POLITECNICO DI TORINO

Collegio di Ingegneria Chimica e dei Materiali

Corso di Laurea Magistrale
in Ingegneria Chimica e dei Processi Sostenibili

Tesi di Laurea Magistrale

Application of population balances to liquid-liquid dispersions: adaptation of breakage and coalescence kernels for dispersions of water in organic viscous solvents

Relatori

dott. Buffo Antonio
dott. Castellano Simone
dott.ssa Charton Sophie

Candidato

Carrillo Lorenzo

Ottobre 2018

A Nonno Lorenzo, per avermi fatto dono dei valori del sacrificio e del lavoro.
A Roberto, per avermi insegnato il vero significato della vita.

CONTENTS

RIASSUNTO

INTRODUZIONE

In ambito ingegneristico numerosi sistemi e apparecchiature impiegano diverse fasi immiscibili tra di loro. Tali sistemi, detti anche multifase, trovano numerose applicazioni in diversi settori come ad esempio nel petrolchimico, nel farmaceutico, nell'alimentare o nel nucleare. Le operazioni di estrazione, separazione, distillazione sono sicuramente gli esempi più conosciuti [1] [2]. Il caso più semplice di sistema multifase è quello costituito da due sole fasi. Tra i diversi sistemi bifasici esistenti, nel corso di questo studio si farà riferimento ai sistemi liquido-liquido, conosciuti anche come *emulsioni*. In un sistema di questo tipo si identifica una *fase dispersa*, rappresentante il componente disperso sotto forma di gocce, e una *fase continua* [3].

L'agitazione permette alla fase dispersa di distribuirsi all'interno della matrice costituita dalla fase continua. Ogni goccia è sottoposta a due meccanismi che ne modificano le dimensioni: la **rottura** e la **coalescenza**. Tali fenomeni dipendono da vari fattori tra cui la tensione interfacciale tra le due fasi e l'intensità dell'agitazione e della turbolenza, i quali determinano il prevalere delle forze inerziali o viscose all'interno della dispersione [3] [4]. Ad esempio, la formazione di gocce molto piccole in emulsione richiede un elevato grado di turbolenza che si traduce in un elevato consumo energetico [3].

Una dispersione può essere classificata a seconda della frazione volumica globale della fase dispersa ϕ [3]:

- $\phi < 0{,}01$, **sistemi diluiti:** le gocce disperse non hanno una loro inerzia e sono quindi trasportate dalla fase continua. Per tal motivo può essere trascurata durante la fase di modellizzazione, se questa ha densità simile a quella della fase continua.
- $\phi < 0{,}2$, **sistemi moderatamente diluiti:** l'interazione tra le gocce diventa importante al punto da modificare la distribuzione dimensionale. Tuttavia, se la fase dispersa ha densità simile a quella della fase continua e se le dimensioni delle gocce sono ridotte il sistema può essere considerato monofasico per descriverne la fluidodinamica.

La produzione di emulsioni avviene in diverse apparecchiature, a seconda del grado di dispersione desiderato e in base alla dimensione richiesta per le gocce. Tra le apparecchiature più importanti si possono citare i **reattori agitati** [3] [6], gli **omogeneizzatori ad alta pressione** [1] [7] e i **miscelatori statici** [3] [8], presentati in figura 1, ma anche le **colonne pulsate** [12].

Alcuni comportamenti a livello macroscopico in un sistema bifasico dipendono in primis dalla natura delle fasi coinvolte, ma anche dal comportamento delle particelle disperse a livello macroscopico. Al fine di monitorare l'evoluzione nel tempo di tali comportamenti da parte della fase dispersa, si può impiegare un **bilancio di popolazione (Population balance equations, PBE)** [9]. A livello matematico, un bilancio di popolazione è costituito da un'equazione integro-differenziale la cui incognita, conosciuta con il nome di *Number density function (NDF)*, permette di monitorare l'evolversi nel tempo e nello spazio del numero di particelle per unità di volume aventi certe proprietà. Ad esempio, il trasferimento di materia, meccanismo fondamentale alla base delle estrazioni, dipende dalla area interfacciale tra le due fasi. In questo caso, l'utilizzo di

un bilancio di popolazione permette di seguire l'evoluzione temporale di tale proprietà, permettendo un'eventuale ottimizzazione delle apparecchiature di processo [10].

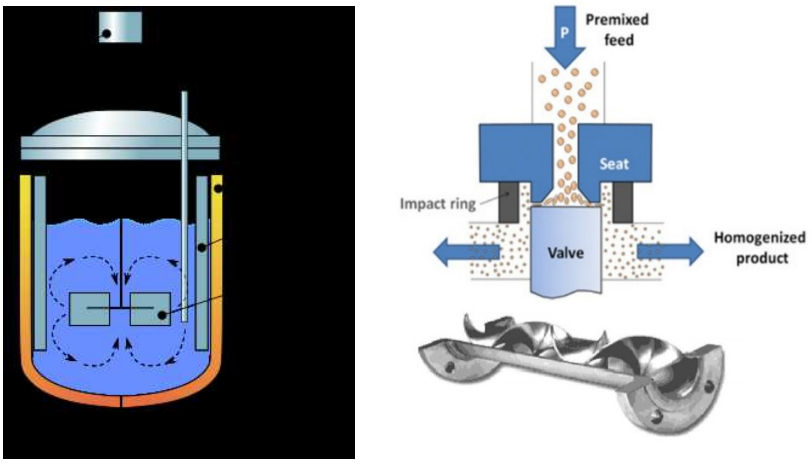

Figura 1 - Principali apparecchiature impiegate per la produzione di emulsioni

In questo lavoro di tesi, i bilanci di popolazione sono stati impiegati nello studio di dispersioni in cui la fase dispersa è rappresentata dalla fase acquosa, mentre la fase continua è costituita dalla fase organica. Contestualmente, tale lavoro si inserisce nel percorso di dottorato intrapreso dal dottor Castellano Simone, presso l'Università di Lione "Claude Bernard" in collaborazione con il CEA (Commissariat à l'Énergie atomique et aux Énergies Alternatives) di Marcoule (Francia).

Esempi di applicazione di un bilancio di popolazione

I bilanci di popolazione possono essere applicati in diverse aree. Numerosi esempi possono essere trovati in letteratura riguardo al loro impiego non solo in svariati ambiti ingegneristici, ma anche per il controllo demografico di una popolazione [27] [28].

Tuttavia, durante questo lavoro, i bilanci di popolazione sono stati applicati per lo studio della fase di estrazione dell'Uranio e del Plutonio nell'ambito del processo PUREX, processo chimico-fisico che permette il recupero di tali elementi a partire da barre di combustibile nucleare post-combustione. Tale processo prevede una prima fase di trinciatura delle barre di combustibile seguita dalla dissoluzione dei residui solidi in acido nitrico ad alta concentrazione e ad alta temperatura. Infine, l'U e il Pu vengono recuperati attraverso una serie di estrazioni liquido-liquido, ponendo in contatto la soluzione acida con una soluzione organica, costituita da Isane o Kerosene (entrambe miscele di idrocarburi a catena C-12 – C-14) e TBP (tributilfosfato) [11]. Tale fase di estrazione prevede l'impiego di diverse apparecchiature, quali i contattori centrifughi, i miscelatori separatori e le colonne pulsate [12]. In figura 2 si può trovare uno schema riassuntivo del processo PUREX.

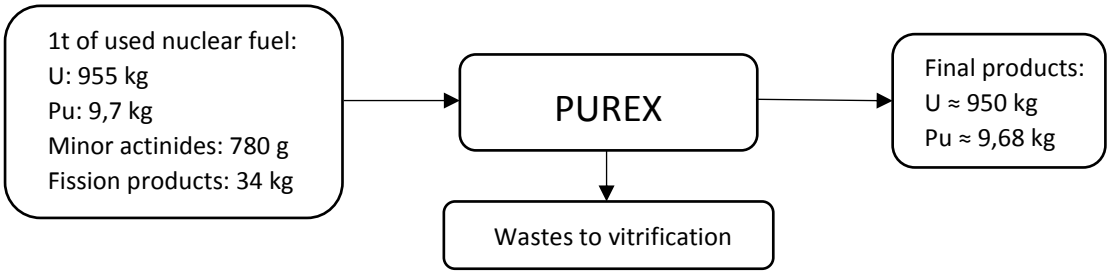

Figura 2 - Schema riassuntivo del processo PUREX: dalle barre di combustibile usate vengono estratti U e Pu che saranno poi reimpiegati per la fabbricazione di nuovo combustibile. Gli scarti sono vetrificati e interrati.

Organizzazione del lavoro

Il seguente lavoro è stato possibile grazie alla collaborazione con il CEA di Marcoule. In tale sede è stato possibile effettuare lo studio sperimentale e teorico del processo d'estrazione liquido-liquido in analisi e la conseguente modellizzazione.

Dopo una prima fase di raccolta delle informazioni presenti in letteratura riguardanti i bilanci di popolazione, i fenomeni di rottura e coalescenza delle gocce e gli studi esistenti in tale ambito, è stata programmata una fase sperimentale per la raccolta dei dati necessari alla modellizzazione finale. In tale fase, l'obiettivo è stato quello di testare diverse condizioni operative, variando la viscosità dei solventi impiegati. In particolare, il cambiamento di viscosità è legato ad una problematica riguardante dei processi alternativi al PUREX, sviluppati dal CEA. Tali alternative propongono l'utilizzo di molecole estrattive diverse (ad esempio le monoammidi) le quali, tuttavia, presentano un aumento di viscosità (fino a 10 cP) proporzionale alla quantità di U e Pu disciolti, causando delle alterazioni a livello fluidodinamico nelle apparecchiature. In seguito, al fine di avvicinarsi il più possibile alle reali condizioni di processo, sono state effettuate delle esperienze impiegando il TBP.

Per quanto riguarda la procedura adottata per l'interpolazione dei dati sperimentali basata sui modelli teorici, nella prima parte di tale lavoro è stata impiegata una prima versione sviluppata in precedenza dal dr. Castellano. Tuttavia, all'aumentare della viscosità, questo primo modello si è dimostrato incapace di fornire un'adeguata interpretazione della realtà. Per tal motivo, sono state necessarie alcune modifiche che hanno portato alla definizione di una seconda versione (*Improved model*) capace di fornire risultati piuttosto soddisfacenti.

In sintesi, gli obiettivi di tale lavoro di ricerca sono stati:

- Riproduzione delle reali condizioni e problematiche del processo PUREX e dei problemi connessi alle varianti in fase di sviluppo, in particolare legati all'aumento di viscosità.
- Utilizzo del modello iniziale per l'interpolazione dei dati.
- Sviluppo di un nuovo modello.
- Codifica e traduzione delle leggi fisiche alla base del modello in linguaggio MATLAB.
- Esecuzione di simulazioni CFD per l'ottenimento di dati fondamentali necessari all'utilizzo del nuovo modello.
- Ricerca di eventuali limiti del nuovo approccio proposto.

L'intero lavoro di tesi, inoltre, si inserisce in un percorso di Doppia Laurea - Erasmus, che ha coinvolto il Politecnico di Torino (Italia) e l'Ecole des Mines di Saint-Etienne (Francia).

FONDAMENTI TEORICI

Per comprendere le ipotesi e l'evoluzione del modello proposto in questo lavoro, è necessario fornire alcune nozioni fondamentali riguardanti i bilanci di popolazione e il concetto di turbolenza.

La turbolenza: la teoria della cascata di energia e la teoria di Kolmogorov

Un fluido in regime di turbolenza è caratterizzato da cambiamenti aleatori delle grandezze che ne descrivono il comportamento a livello microscopico [13]. Questo regime è dovuto al prevalere delle forze inerziali rispetto alle forze viscose. Il rapporto tra tali forze è noto come numero di Reynolds, il quale permette facilmente di comprendere la natura del flusso in analisi. La turbolenza è molto importante a livello ingegneristico in quanto permette di accelerare alcuni

fenomeni fisici come lo scambio di materia o lo scambio di quantità di moto. Questo permette una drastica riduzione delle dimensioni necessarie alle apparecchiature.

La turbolenza è definita come *fenomeno multi-scala*. Tale definizione le è stata attribuita da Richardson, il quale per la prima volta provò ad interpretare la natura microscopica di tale regime fluidodinamico. Egli ipotizzò che un fluido turbolento sia caratterizzato a livello microscopico dalla presenza di piccoli vortici, chiamati *eddies*, aventi dimensioni diverse. Tuttavia, essi presentano tutti il medesimo comportamento: gli eddies hanno infatti la tendenza a rompersi in vortici sempre più piccoli trasferendo energia da una scala all'altra. La rottura prosegue fino al raggiungimento di un limite fisico oltre il quale le forze viscose tornano a prevalere rispetto a quelle inerziali, permettendo infine la dissipazione di energia sotto forma di calore [13]. Nella figura 3 è schematizzato il processo di rottura dei vortici e di trasferimento e di dissipazione di energia a piccole scale.

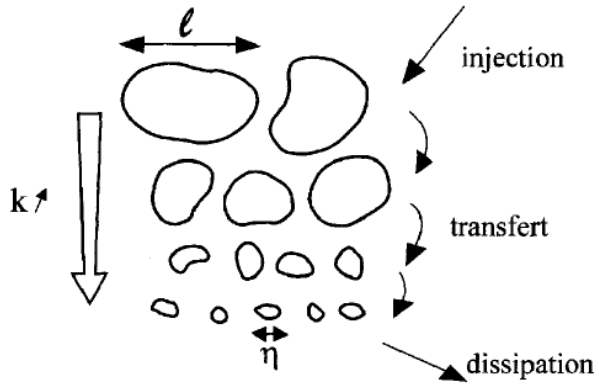

Figura 3 - La cascata d'energia in un flusso turbolento: i vortici si trasformano in vortici più piccoli trasferendo energia alle scale inferiori.

A questo punto è necessario definire quali siano le diverse scale di grandezza possibili per gli eddies. A tal proposito, è possibile impiegare la **teoria di Kolmogorov** la quale è basata fondamentalmente su tre ipotesi [13]:

I. **ISOTROPIA LOCALE**: per Re sufficientemente elevati, in un flusso turbolento si osserva che i vortici aventi una dimensione sufficientemente piccola siano localmente isotropi. La dimensione richiesta dev'essere tale che $l < l_{EI}$, dove $l_{EI} = l_0/6$ e l_0 è la dimensione caratteristica del mezzo in cui avviene il flusso in condizioni di turbolenza. Tali vortici appartengono quindi ad una gamma denominata *Universal Equilibrium Range*.

II. **PRIMA IPOTESI DI SIMILARITA'**: gli eddies di piccola taglia sono caratterizzati da una distribuzione di probabilità per le velocità relative $\overline{\boldsymbol{u^2(r)}}$. Per Re sufficientemente elevati, tale distribuzione dipende unicamente da due grandezze: $\boldsymbol{\varepsilon}$, il **tasso di dissipazione di energia cinetica turbolenta**, e $\boldsymbol{\upsilon}$, la **viscosità cinematica**. Tale formulazione è universale. Inoltre, tale ipotesi permette di definire matematicamente quel limite fisico ipotizzato da Richardson oltre il quale il prevalere delle forze viscose permette la scomparsa dei vortici e la conseguente dissipazione di energia. Tale limite è conosciuto come ***Microscala di Kolmogorov***:

$$\eta = \left(\frac{\upsilon^3}{\varepsilon}\right)^{1/4} \qquad (1)$$

Quando gli eddies raggiungono tale dimensione il valore del Re diventa pari ad 1.

III. **SECONDA IPOTESI DI SIMILARITA'**: se gli eddies hanno una dimensione tale che $l_0 \gg l \gg \eta$, la distribuzione di probabilità per le velocità relative $\overline{\boldsymbol{u^2(r)}}$ dipende **unicamente da $\boldsymbol{\varepsilon}$**.

Le ipotesi di Kolmogorov permettono quindi di dividere l'*Universal Equilibrium Range* in due sottodomini: l'***Inertial subrange*** ($l_{EI} > l > l_{DI}$) e il ***Dissipation range*** ($l < l_{DI}$). Tale suddivisione è rappresentata schematicamente in figura 4. Nel primo range è applicabile unicamente la seconda ipotesi di similarità, mentre nel *Dissipation range* sono valide entrambe. In tal modo, è possibile definire la velocità relativa $\overline{u^2(r)}$ in funzione delle dimensioni dei vortici e del range al quale questi appartengono [14]:

- INERTIAL SUBRANGE:

$$\overline{\boldsymbol{u^2(r)}} = \boldsymbol{C_1(\varepsilon r)^{\frac{2}{3}}} \tag{2}$$

- DISSIPATION RANGE:

$$\overline{\boldsymbol{u^2(r)}} = \boldsymbol{C_2\left(\frac{\varepsilon}{\upsilon}\right)r^2} \text{ (if } \boldsymbol{r \to \eta}) \tag{3}$$

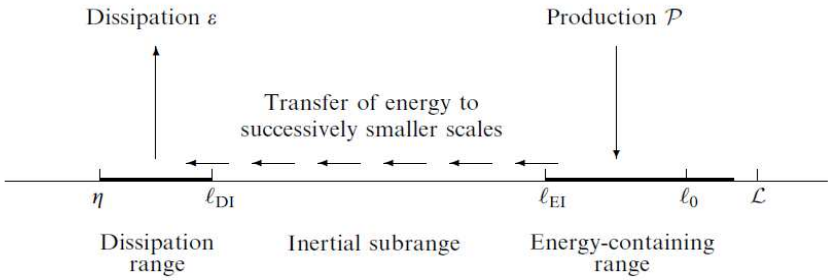

Figura 4 - La divisione in range proposta da Kolmogorov

Lo spettro d'energia secondo Kolmogorov

Secondo la teoria di Richardson, i vortici possiedono una certa quantità di energia che trasmettono alle scale inferiori per poi finalmente essere dissipata. A tal proposito è interessante studiare il contenuto energetico degli eddies, definito come spettro d'energia, al variare della loro dimensione, espressa come lunghezza d'onda κ ($\kappa = 2\pi/l$) [13] mostrato in figura 5.

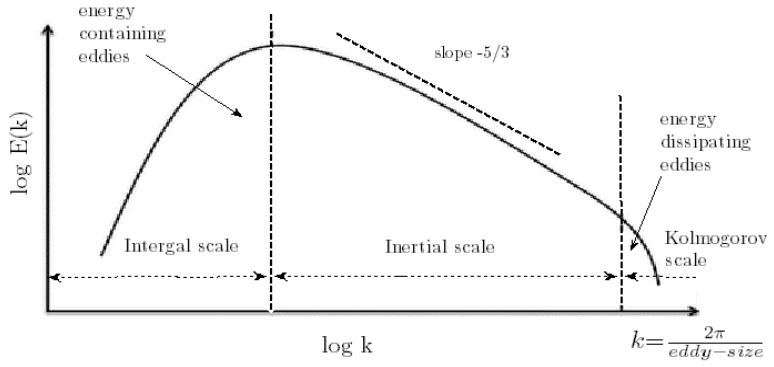

Figura 5 - Lo spettro d'energia degli eddies. Si osservi come l'andamento nell'Inertial subrange resti costante. Sia l'energia che la lunghezza d'onda sono espresse in scala logaritmica.

Cosí come stabilito dalle ipotesi di similarità di Kolmogorov, tale spettro di energia deve necessariamente assumere una forma universale per i vortici a media-alta lunghezza d'onda. Dunque, è possibile definire matematicamente l'andamento dell'energia posseduta dai vortici nell'*Inertial subrange*, dove la seconda ipotesi di similarità è applicabile [13]:

$$E(\kappa) = C\varepsilon^{\frac{2}{3}}\kappa^{-\frac{5}{3}} \tag{4}$$

Tale formulazione matematica è anche conosciuta come *legge dei -5/3 di Kolmogorov* (la costante C è detta *costante universale di Kolmogorov* ed assume un valore $\approx 1{,}5$).

Tuttavia, dal grafico in figura 4 si può notare che per valori piuttosto elevati di κ, lo spettro di energia assume un andamento diverso, in cui l'energia diminuisce drasticamente quando κ tende a η.

Le equazioni di bilancio di massa e di quantità di moto

Considerando un fluido a densità ρ costante e incomprimibile in regime turbolento, è possibile descriverne le variazioni delle principali proprietà, in funzione del tempo e dello spazio, attraverso le celebri **equazioni di Navier-Stokes** [31]:

- **EQUAZIONE DI CONTINUITA' (conservazione della massa):**

$$\nabla \cdot U = 0 \tag{5}$$

- **EQUAZIONE DI BILANCIO DELLA QUANTITÀ DI MOTO:**

$$\frac{DU}{Dt} = -\frac{1}{\rho}\nabla p + \upsilon\nabla^2 U \tag{6}$$

In entrambe le equazioni U rappresenta la velocità istantanea. Nell'equazione (6) p è la *pressione modificata* ($p = P + \rho\Psi$, P è la pressione del fluido e Ψ è il contributo dovuto al potenziale gravitazionale), mentre il termine $\upsilon\nabla^2 U$ rappresenta il termine diffusivo della quantità di moto.

Per tali equazioni esistono delle soluzioni analitiche solo per casi particolari molto semplici. Tuttavia, è possibile adottare un approccio statistico che ne semplifichi parzialmente la risoluzione. Tale approccio, proposto da Reynolds, prevede la sostituzione della velocità istantanea U con la somma del suo valore medio $\langle U \rangle$ e le sui fluttuazioni u:

$$U(x,t) = \langle U(x,t) \rangle + u(x,t) \tag{7}$$

Sostituendo tale definizione nelle equazioni (5) e (6), si ottiene [31]:

$$\nabla \cdot U = \nabla \cdot (\langle U \rangle + u) = 0 \tag{8}$$

$$\frac{\overline{D}\langle U_j \rangle}{\overline{D}t} = -\frac{1}{\rho}\frac{\partial \langle p \rangle}{\partial x_j} + \upsilon\nabla^2\langle U_j \rangle - \frac{\partial \langle u_i u_j \rangle}{\partial x_i} \tag{9}$$

Le equazioni (8) e (9) sono conosciute come **Reynolds-averaged Navier-Stokes equations (RANS)**. Il termine $\langle u_i u_j \rangle$ è il **tensore degli stress di Reynolds**.

Per un generico flusso turbolento tridimensionale, l'equazione di continuità e le tre equazioni della quantità di moto devono essere risolte. Tuttavia, in questo sistema di equazioni compaiono più di quattro incognite (le tre componenti della velocità, la pressione e sei termini del tensore di Reynolds). Tale situazione costituisce il cosiddetto **problema di chiusura**, che può essere risolto esplicitando il termine $\langle u_i u_j \rangle$ in funzione delle altre incognite. L'**ipotesi di Boussinesq** prevede l'introduzione di una nuova proprietà, la **viscosità turbolenta υ_T** [31]:

$$-\frac{\partial \langle u_i u_j \rangle}{\partial x_i} = \upsilon_T\left(\frac{\partial \langle U_i \rangle}{\partial x_j} + \frac{\partial \langle U_j \rangle}{\partial x_i}\right) - \frac{2}{3}k\delta_{ij} \tag{10}$$

Dove k è l'energia cinetica turbolenta e δ_{ij} è il delta di Kronecker.

A questo punto è necessario definire la viscosità turbolenta. A tal proposito, diversi modelli possono essere impiegati, aggiungendo una o più equazioni al sistema precedente. In questo lavoro di tesi la turbolenza è stata quindi modellizzata attraverso uno di questi modelli, il ***k-ε* standard**, il quale aggiunge due equazioni, una per k e una per ε.

La risoluzione di tali equazioni ha sempre rappresentato un problema. Se in passato si ricorreva all'uso di metodi numerici che portassero ad una soluzione analitiche approssimate, al giorno d'oggi il processo di calcolo è stato notevolmente accelerato grazie all'uso di calcolatori elettronici. La branca della fluidodinamica che si occupa di tali problemi è denominata *Computational fluid dynamic* (CFD).

In particolare, il processo di risoluzione delle equazioni di Navier-Stokes è composto da due fasi: una prima fase di **discretizzazione spaziale** del mezzo in cui ha luogo il flusso turbolento, e una seconda di **discretizzazione delle equazioni**, durante la quale le equazioni differenziali vengono trasformate in espressioni algebriche. Nella prima fase, lo spazio è discretizzato in una griglia (*mesh*) che può essere **strutturata** oppure **non-strutturata** [15]. Inoltre, a seconda del tipo di flusso, i modelli possono essere **stazionari** o **transitori** [16]. Principalmente, tre metodi sono usati per la discretizzazione:

- **Metodo alle differenze finite**: è uno schema differenziale basato essenzialmente sugli sviluppi in serie di Taylor.
- **Metodo dei volumi finiti**: è uno schema integrale basato sulla suddivisione dello spazio in piccoli volumetti di dimensione finita. Questo metodo impiega l'equazione di conservazione per ogni volumetto, alla quale è applicato il teorema della divergenza e in seguito discretizzata.
- **Metodo degli elementi finiti**: la griglia è discretizzata in elementi di forma poliedrica. Per ogni elemento vengono definite delle incognite espresse attraverso delle **funzioni interpolanti**.

Bilanci di popolazione

Nel corso di questo lavoro, i bilanci di popolazioni sono stati impiegati per seguire l'evoluzione temporale della dimensione delle particelle della fase dispersa all'interno dei sistemi studiati [9]. In particolare, determinando la distribuzione dei diametri delle gocce disperse è possibile analizzare l'andamento temporale dell'area di scambio tra le due fasi [10].

L'equazione di bilancio di popolazione prevede la determinazione della variazione temporale della NDF attraverso la formulazione di un termine sorgente. In questo studio tale termine risulta essere funzione dei soli fenomeni di rottura e di coalescenza delle gocce. Quindi, in generale [17], considerando rispettivamente delle particelle di volume v e $v-\epsilon$, si può definite la seguente equazione:

$$\begin{aligned}\frac{\partial n'(v;t)}{\partial t} = \frac{1}{2}\int_0^v Q(v-\epsilon,\epsilon)n'(v-\epsilon;t)n'(\epsilon;t)d\epsilon \\ - n'(v;t)\int_0^\infty Q(v,\epsilon)n'^{(\epsilon;t)}d\epsilon \\ + \int_v^\infty \Gamma(\epsilon)p(\epsilon)\beta(v|\epsilon)n'^{(\epsilon;t)}d\epsilon \\ - \Gamma(v)n'(v;t)\end{aligned} \tag{11}$$

Dove,

- $n'(v;t)$ è la densità numerica (NDF).
- $Q(v)$ è definito come **kernel di coalescenza**.
- $\Gamma(v)$ è definito come **kernel di rottura**.
- $\beta(v)$ rappresenta la **daugher size distribution function.** Essa contiene informazioni circa il numero di particelle generate dopo la rottura di una goccia ($p(v)$) e la loro distribuzione in termini di taglia. Essa contiene, dunque, informazioni riguardanti la probabilità per una goccia di formare dei frammenti di una determinata dimensione. In questo lavoro si è assunta una rottura binaria abbinata ad una semplice distribuzione gaussiana.

Nell'equazione (11), si può notare come il termine sorgente sia composto da quattro termini. I primi due rappresentano rispettivamente la formazione e la scomparsa di particelle dovute alla coalescenza, mentre gli ultimi due hanno un significato analogo ma rappresentano il contributo della rottura.

I termini $Q(v)$ e $\Gamma(v)$ rapresentano quindi i cosiddetti *kernel*s, i quali permettono la modellizzazione matematica dei fenomeni di coalescenza e di rottura delle gocce. A seconda del sistema studiato, in letteratura sono disponibili diverse definizioni [18] [19]. Tuttavia, nel caso di un sistema liquido-liquido in regime turbolento le espressioni più utilizzate sono quelle di **Coulaloglou and Tavlarides** [5]:

$$Q(v,v') = K_3\left(v^{\frac{2}{3}} + v'^{\frac{2}{3}}\right)\left(v^{\frac{2}{9}} + v'^{\frac{2}{9}}\right)\varepsilon^{1/3}\exp\left[-\frac{K_4\mu_c\rho_c\varepsilon}{\sigma^2}\left(\frac{v^{1/3}v'^{1/3}}{v^{1/3}+v'^{1/3}}\right)\right] \qquad (12)$$

$$\Gamma(v) = K_1 v^{-2/9}\varepsilon^{1/3}\exp\left(-\frac{K_2\sigma}{\rho_d v^{5/9}\varepsilon^{2/3}}\right) \qquad (13)$$

Notiamo che in tali espressioni compaiono le dimensioni delle particelle (i volumi v e v'), alcune proprietà fisiche delle due fasi presenti (μ_c e ρ_c per la fase continua e ρ_d per la fase dispersa), le condizioni di turbolenza rappresentate da ε, e quattro parametri K_1, K_2, K_3 e K_4.

Il Fixed Pivot Method per la risoluzione dell'equazione di bilancio di popolazione

La risoluzione dell'equazione di bilancio (11) è possibile solo attraverso l'impiego di un metodo numerico semplificativo. Il metodo selezionato in questo studio è il Fixed Pivot Method (FPM), sviluppato da Kumar e Ramkrishna [20]. Tale metodo garantisce l'esattezza di due momenti generici della distribuzione delle particelle. Per convenienza si sceglie il momento legato al numero di particelle e quello legato al volume totale.

Il primo step è la discretizzazione dello spazio della coordinata v in *M* intervalli $[v_i; v_{i+1}]$. Il FPM assume che tutte le gocce, la cui dimensione è compresa all'interno dell'intervallo $[v_i; v_{i+1}]$, siano centrate nel pivot, definito come $v_i < x_i < v_{i+1}$. In tal modo è possibile risolvere l'equazione di bilancio per ogni singolo intervallo individuato.

Quindi, secondo tale metodo, la NDF può essere espressa come:

$$n(v,t) = \sum_{i=1}^{M} N_i(t)\delta(v - x_i) \qquad (14)$$

Dove N_i è il numero di particelle per unità di volume che appartengono all'intervallo i-esimo, assumendo che tutte abbiano volume x_i.

Infine, l'applicazione del FPM porta alla riformulazione dell'equazione (11), che viene riscritta in funzione di N_i, diventando quindi un sistema di equazioni differenziali ordinarie:

$$\frac{dN_i(t)}{dt} = \sum_{\substack{j,k \\ x_{i-1} \le (x_j + x_k) \le x_{i+1}}}^{j \ge k} \left(1 - \frac{1}{2}\delta_{j,k}\right) \eta \, Q_{j,k} N_j(t) N_k(t) - \Gamma_i N_i(t) - N_i(t) \sum_{k=1}^{M} Q_{i,k} N_k(t) + \sum_{x_i}^{x_{i+1}} n_{i,k} \, \Gamma_k N_k(t) \tag{15}$$

Nel corso di questo studio, si è preferito tener conto dell'evoluzione della taglia delle particelle calcolando il **diametro medio di Sauter**, definito come il rapporto tra il momento di ordine tre e quello di ordine due della distribuzione:

$$d_{32} = \frac{m_3}{m_2} \tag{16}$$

Modello iniziale – le inomogeneità della turbolenza

Le espressioni (12) e (13) tengono conto degli effetti della turbolenza tramite ε. Tuttavia, in letteratura si possono reperire quasi esclusivamente studi che considerano $\bar{\varepsilon}$ uniforme nello spazio. In realtà, quest'ipotesi ideale non trova riscontro nella realtà, dove le simulazioni CFD, evidenziano le disomogeneità della turbolenza nello spazio, come nelle seguenti immagini:

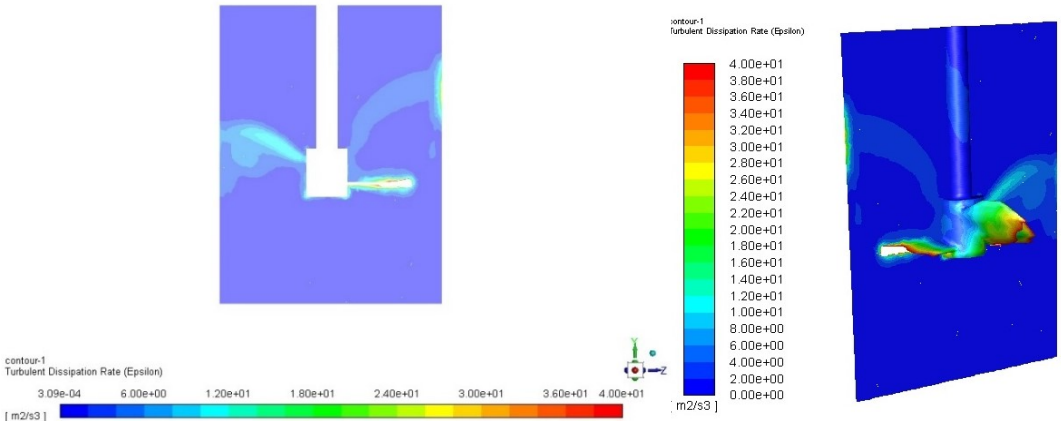

Figura 6 – Attraverso una simulazione CFD si può notare come la distribuzione di ε non sia omogenea nel reattore.

Ad esempio, all'interno di un reattore agitato, come rappresentato in Figura 6, la turbolenza sarà più elevata nell'intorno dell'agitatore che nel resto del reattore. Ed è per questo motivo che le gocce hanno una maggiore probabilità di frammentarsi in tale zona, mentre nel resto del reattore il meccanismo prevalente è la coalescenza.

Al fine di poter considerare le disomogeneità spaziali delle grandezze turbolente è necessario rendere indipendenti dalla coordinata spaziale $\boldsymbol{x}$ i termini dell'equazione (11). Per fare ciò, è necessario mediare rispetto al volume totale i termini dell'equazione di bilancio.

$$\bar{n}(v,t) = \frac{1}{V}\int_V n(\boldsymbol{x}, v, t) d\boldsymbol{x} \tag{17}$$

$$\frac{1}{V}\int_V Q(\boldsymbol{x}, v) d\boldsymbol{x} \approx \bar{Q}(v, \varepsilon(\boldsymbol{x})) \tag{18}$$

$$\frac{1}{V}\int_V \Gamma(\boldsymbol{x}, v)d\boldsymbol{x} \approx \bar{\Gamma}(v, \varepsilon(\boldsymbol{x})) \tag{19}$$

Nelle espressioni (18) e (19), tuttavia, compare ancora la dipendenza dalla coordinata $\boldsymbol{x}$, a causa della presenza del termine $\varepsilon(\boldsymbol{x})$. È quindi necessario mediare nuovamente rispetto al volume totale:

$$\frac{1}{V}\int_V Q(\boldsymbol{x}, v, v')dx \approx \int_0^\infty Q(\varepsilon, v, v')f(\varepsilon)d\varepsilon = \bar{Q}(v, v') \tag{20}$$

$$\frac{1}{V}\int_V \Gamma(\boldsymbol{x}, v)dx \approx \int_0^\infty \Gamma(\varepsilon, v)f(\varepsilon)d\varepsilon = \bar{\Gamma}(v) \tag{21}$$

Dove $f(\varepsilon)$ è la densità di probabilità volumica, conosciuta anche come ***Probability density function*** **(PDF)** della dissipazione dell'energia cinetica turbolenta. Tale funzione rappresenta la probabilità che ε assuma un valore compreso tra ε e $\varepsilon + d\varepsilon$ in tutto il volume considerato. Per tal motivo essa non dipende dalle coordinate spaziali [21] [22].

In questo lavoro di tesi, la funzione la PDF di ε ($f(\varepsilon)$) è stata ottenuta attraverso una serie di simulazioni CFD operate attraverso il software **ANSYS Fluent**. L'equazione finale del bilancio di popolazione diventa quindi la seguente:

$$\begin{aligned}\frac{\partial \bar{n}(v,t)}{\partial t} = \frac{1}{2}\int_0^v \bar{Q}\big((v-v'), v'\big)\bar{n}(v',t)\bar{n}\big((v-v'), t\big)dv' \\ - \bar{n}(v,t)\int_0^\infty \bar{Q}(v, v')\bar{n}(v,t)dv' \\ + \int_L^\infty \bar{\Gamma}(v')p(v, v')\beta(v, v')\bar{n}(v,t)dv' - \bar{\Gamma}(v)\bar{n}(v,t)\end{aligned} \tag{22}$$

Un modello di questo tipo viene definito come *modello omogeneo* (o 0D) e permette di ottenere rapidamente una soluzione al problema presentato, fornendo risultati precisi quanto più la distribuzione spaziale è omogenea. Questa si riscontra a basse frazioni volumiche di fase dispersa [21] [22].

Modello avanzato – Sovrastima della dissipazione energetica

Come visto in precedenza, l'espressione della *legge dei -5/3 di Kolmogorov* risulta essere non più applicabile nel *Dissipation range*, dove il grafico in figura 5 mostra un andamento completamente diverso rispetto a quello assunto nell'*Inertial subrange*. L'errore concettuale alla base del modello iniziale è infatti contenuto nell'utilizzo delle definizioni di Coulaloglou e Tavlarides, anche quando le gocce hanno dimensione inferiore agli eddies del subrange inerziale. Questo porta infatti a una sovrastima dell'energia dissipata a livello del *Dissipation range*.

Nel corso di questo lavoro, si è reso necessario reperire in letteratura una nuova formulazione per lo spettro d'energia dei vortici, tale da poter considerare correttamente l'interazione fra gocce ed eddies tutto lo spettro d'energia. La nuova formulazione è fornita da **Pope** ed è la seguente [13]:

$$E(\kappa) = C\varepsilon^{\frac{2}{3}}\kappa^{-\frac{5}{3}}\left(\frac{\kappa L}{[(\kappa L)^2 + c_L]^{\frac{1}{2}}}\right)^{\frac{11}{3}} exp(-\beta\{\big[(\kappa\eta)^4 + c_\eta^4\big]^{\frac{1}{4}} - c_\eta\}) \tag{23}$$

Dove,

- L rappresenta la scala integrale della turbolenza, ovvero la dimensione caratteristica del sistema, considerata pari al diametro dell'agitatore.

- Il termine contenuto nell'esponenziale è la funzione adimensionata $f_\eta(\kappa\eta)$, la quale modellizza lo spettro d'energia nel *Dissipation range*. β è una costante sperimentale (=5,2) [23].
- I coefficienti c_L e c_η sono ottenuti risolvendo il seguente sistema di equazioni:

$$\begin{cases} \varepsilon - \int_0^\infty 2\upsilon k^2 E\left(k, c_L, c_\eta\right) dk = 0 \\ k - \int_0^\infty E\left(k, c_L, c_\eta\right) dk = 0 \end{cases} \tag{24}$$

Al fine di ottenere una nuova definizione di velocità relativa tra due punti, da inserire nei nuclei di rottura e coalescenza, si è reso necessario fornire una nuova formulazione matematica di $\bar{u}(v)^2$ che potesse permetterne il calcolo considerando il nuovo $E(\kappa)$ [24]:

$$\langle [\Delta u(r)]^2 \rangle \approx \frac{4}{3} \int_0^\infty E(\kappa) \left\{ 1 - 3 \left[\frac{sin(\kappa r)}{(\kappa r)^3} - \frac{cos(\kappa r)}{(\kappa r)^2} \right] \right\} d\kappa \tag{25}$$

L'ultimissimo step nella formulazione del modello avanzato è la riscrittura delle espressioni dei nuclei di Coulaloglou e Tavlarides in funzione di $\bar{u}(v)^2$:

$$Q(v, v') = K_3 \left(v^{\frac{2}{3}} + v'^{\frac{2}{3}} \right) \left(\bar{u}(v)^2 + \bar{u}(v')^2 \right)^{1/2} \exp\left[-\frac{K_4 \mu_c \rho_c}{\sigma^2} \frac{\left(v^{1/3} v'^{1/3} \right)^4}{\left(v^{1/3} + v'^{1/3} \right)^5} [\bar{u}(v + v')^2]^{3/2} \right] \tag{26}$$

$$\Gamma(v) = K_1 \sqrt{\bar{u}(v)^2} v^{-1/3} \exp\left(-\frac{K_2 \sigma}{\rho_d v^{1/3} \bar{u}(v)^2} \right) \tag{27}$$

MATERIALI E METODI

L'obiettivo di tale lavoro di tesi è l'analisi dell'evoluzione temporale delle dimensioni delle gocce d'acqua disperse all'interno di un solvente organico. I due modelli presentati sono stati impiegati per l'interpolazione dei dati reali, raccolti durante una fase sperimentale preliminare. L'obiettivo ultimo è l'incremento della viscosità del solvente organico nonché un riavvicinamento alle condizioni operative del processo PUREX.

Nella fase sperimentale, dunque, sono stati miscelati diversi composti organici al fine di poter ottenere i livelli di viscosità desiderati. I tre composti principali sono:

- **Isane IP175**: composto in prevalenza da catene di carbonio C-12 – C-14, si presenta inodore e incolore. Tale sostanza viene principalmente impiegata come lubrificante e per la preparazione di vernici.
- **Marcol**: si tratta di una sostanza di origine petrolifera composta in prevalenza da idrocarburi insaturi, ottenuta tramite diverse fasi di raffinazione. Tale composto ha una viscosità dieci volte superiore a quella dell'Isane ed è essenzialmente utilizzato in ambito farmaceutico e cosmetico.
- **TBP**: il tributilfosfato presenta una tensione superficiale molto bassa rispetto ai precedenti composti. Esso viene utilizzato come fluido caloportore, come lubrificante o come plasticizzante.

Il reattore nel quale è stata condotta la fase sperimentale è un reattore agitato in vetro, dal volume di un litro, mostrato in Figura 7. Il sistema di agitazione è composto da un agitatore di tipo **Mixel-TT a tre pale** e da **4 baffles** che impediscono la formazione di vortici dovuti al

ricircolo del flusso. Le pareti del reattore sono state silanizzate, mentre il sistema di miscelazione è stato teflonizzato al fine di evitare interferenze nei meccanismi di rottura e di coalescenza delle gocce d'acqua.

Il dispositivo sperimentale include una sonda endoscopica SOPAT. Tale sonda ha permesso il monitoraggio dell'evoluzione temporale delle dimensioni delle gocce attraverso l'acquisizione di circa 190-240 immagini al minuto. La sonda è inoltre dotata di un flash stroboscopico (frequenza compresa tra 5 e 7 Hz) necessario per evidenziare le due differenti fasi.

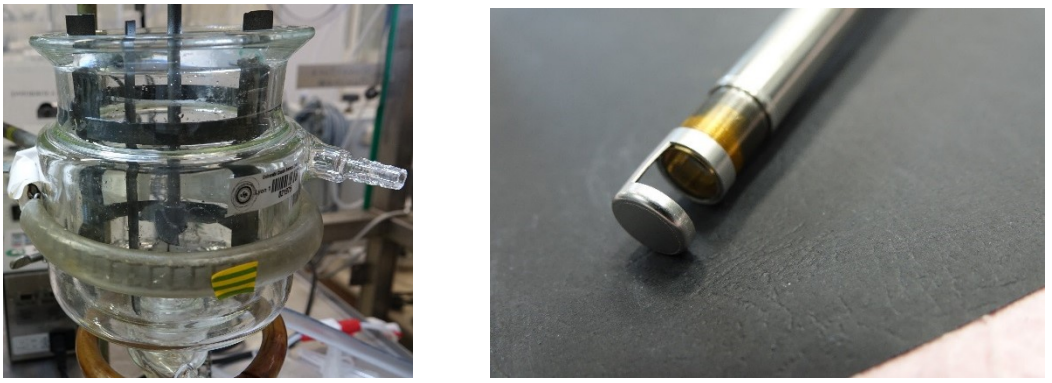

Figura 7 – A sinistra il reattore e il sistema d'agitazione impiegati durante la fase sperimentale, a destra la sonda endoscopica impiegata per rilevare la variazione temporale della taglia delle particelle.

Il primo step per ogni prova sperimentale è il riempimento del reattore con il solvente organico, costituente la fase continua. In seguito viene iniettata la corretta quantità d'acqua corrispondente all'1% o al 2% del volume totale. Il sistema di agitazione viene quindi attivato, imponendo il valore desiderato di velocità rotazionale attraverso la regolazione della potenza erogata dal rotore. La sonda endoscopica viene inserita nella dispersione per la raccolta delle immagini necessarie circa ogni 10-15 minuti. Ogni esperimento ha una durata di circa 5-6 ore, tranne che per quelli in cui si è impiegato il TBP. In tal caso la presenza di gocce al di sotto del limite di detezione della sonda endoscopica (15 µm) ha ridotto il tempo delle esperienze a circa 1,5 ore.

In seguito, le immagini vengono analizzate attraverso il software per il trattamento d'immagini fornito con il sistema endoscopico. Infine, nella fase di post-trattamento dati, si estraggono i diagrammi corrispondenti alle distribuzioni nei vari istanti di misurazione.

Le equazioni matematiche dei bilanci di popolazione sono state implementate in MATLAB e risolte attraverso la funzione ***ode15s***, la quale permette l'integrazione di equazioni differenziali. Tale codice ha permesso inoltre di valutare le principali differenze tra le due versioni del modello impiegate.

Tuttavia, nel caso del *modello avanzato*, è stato necessario lo sviluppo di un secondo codice parallelo che permettesse il calcolo della velocità $\bar{u}(v)^2$, secondo la nuova definizione. Le funzioni impiegate per la risoluzione delle equazioni (22) – (24) sono ***integral***, per il calcolo degli integrali, e ***fsolve***, per la soluzione dell'equazione non lineare. Tale codice costituisce la problematica più critica dell'intero lavoro, in quanto a livello computazionale esso richiede un tempo compreso tra 20 e 25 minuti per esperienza.

I parametri presenti nelle espressioni dei kernels di rottura e coalescenza sono stati ottenuti tramite un processo di ottimizzazione delle varie versioni dei modelli con i dati sperimentali delle esperienze **1-2 % di acqua in Isane a 600 rpm**. L'identificazione dei parametri è stata dunque

condotta attraverso la funzione ***patternsearch*** della toolbox MATLAB Global Optimization. Tale funzione ha permesso la minimizzazione degli scarti calcolati tra il diametro di Sauter teorico, valutato attraverso i modelli, e i dati reali, presi ad un dato istante. Nella seguente tabella si indicano i valori dei 4 parametri:

Tabella 1 - La tabella contiene i quattro parametri presenti nei nuclei di rottura e coalescenza

	Uniform ε	Initial model	Advanced model
k1	0,0784	0,0012	2,23E-04
k2	0,306	0,711	0,708
k3	0,000375	0,0195	1,0073
k4	8,23E+18	2,05E+14	1,68E+18

Simulazioni CFD: ipotesi semplificative

Come già anticipato in precedenza, le PDF di ε sono state ottenute attraverso una serie di simulazioni CFD impiegando ANSYS Fluent. Tuttavia, alcune ipotesi semplificative sono state formulate al fine di rendere più rapida la convergenza:

- Studio di un sistema **monofase**, giustificato dalle basse percentuali di fase dispersa.
- Modellizzazione della turbolenza attraverso il modello ***k-ε* standard.**
- Modellizzazione della sezione in movimento della mesh attraverso il metodo **Multiple Reference Frame (MRF)** [25]**.**
- **Schema upwind del secondo ordine**.
- **Simulazioni in transitorio** (formulazione implicita del secondo ordine).

Il seguente grafico mostra un esempio di PDF ottenuta per il caso dell'Isane in fase continua. La densità di probabilità è indicata sull'asse delle y, mentre in ascisse sono indicati i valori di ε.

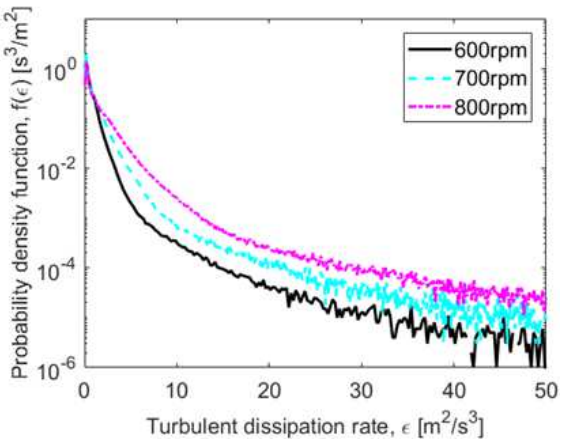

Figura 8 – La PDF di ε è mostrata in funzione di ε. Essa dipende dalla velocità di rotazione, che aumenta la quantità di energia dissipata dal fluido, e quindi ε.

RISULTATI

In questa sezione sono presentati i principali risultati. La restante parte è disponibile nel capitolo 4 della tesi.

È importante notare che sia per il modello iniziale che per quello avanzato i parametri presentati nella definizione dei kernels (k_1, k_2, k_3 e k_4) sono stati ottenuti tramite l'ottimizzazione dei modelli con una singola condizione operativa, rispettivamente con le esperienze a 1-2% d'Isane in acqua e con le esperienze a 1-2% d'acqua in Isane. In seguito, gli stessi parametri sono stati impiegati per l'interpolazione dei dati ottenuti imponendo condizioni operative differenti. I risultati presentati dimostrano quindi che i parametri trovati possono essere impiegati a

prescindere dalle condizioni di viscosità, di turbolenza, ecc., fornendo sempre risultati soddisfacenti.

Durante la fase sperimentale, si è potuto notare come la dimensione delle gocce fosse dipendente in primis dalla tensione interfacciale, ma soprattutto dalla frazione d'acqua considerata e dalla velocità di rotazione dell'agitatore. In particolare, il diametro di Sauter delle particelle della fase dispersa varia proporzionalmente alla quantità d'acqua presente nella dispersione e tende a diminuire quando la velocità dell'agitatore aumenta. In ultima analisi, è stato possibile analizzare l'effetto della viscosità. In particolare si è rilevato che un aumento di viscosità permette di ridurre la dimensione iniziale delle gocce verso diametri inferiori. Tuttavia, la crescita di viscosità riduce contemporaneamente il grado di turbolenza del sistema, portando ad un rallentamento dei fenomeni di rottura delle gocce. Per tale ragione, si ha una dinamica più lenta per quanto riguarda le dimensioni delle particelle della fase dispersa. I dati relativi alla variazione dei diametri delle gocce sono disponibili all'interno del paragrafo 4.1 della tesi.

Nella seguente tabella sono riassunte le principali proprietà e le condizioni operative adottate nel corso della fase sperimentale:

Tabella 2 - Sono presentate le condizioni operative e le principali proprietà dei solventi impiegati.

Test number	Solvents				Conditions and properties			
	Marcol [%]	Isane [%]	TBP [%]	Water [%]	Duration [h]	μ [cP]	ρ [Kg/m^3]	Δσ [mPa.s]
1 – 3	0	100	0	2%	6	1,219	757,4	38,30
4 – 6	30	70	0	1% - 2%	6	2,429	783,4	38,21
7 - 12	45	55	0	1%	6	4,102	799,9	39,81
13 - 18	0	70	30	1% - 2%	1,5	1,608	821,4	10,50
19 - 24	30	40	30	1% - 2%	1,5	3,384	848,2	15,90

Modello iniziale

Nella prima parte di questo studio il campo di applicazione del modello sviluppato da Castellano è stato esteso alle soluzioni aventi un tenore in acqua superiore, ovvero pari al 2% del volume totale. I risultati, riportati qui di seguito, mostrano come l'utilizzo della PDF di ε permetta di ottenere una migliore interpretazione dei dati sperimentali rispetto all'impiego di $\bar{\varepsilon}$, come mostrato in Figura 9. Questo permette di considerare in maniera più efficace gli effetti dovuti alle zone a più forte turbolenza, in cui i meccanismi di rottura e di coalescenza hanno una frequenza diversa rispetto alla sezione restante del reattore.

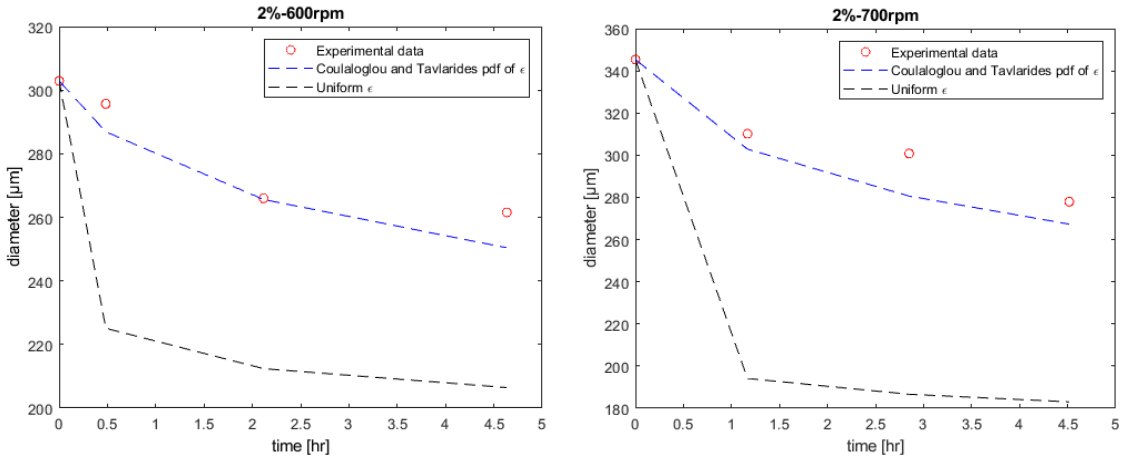

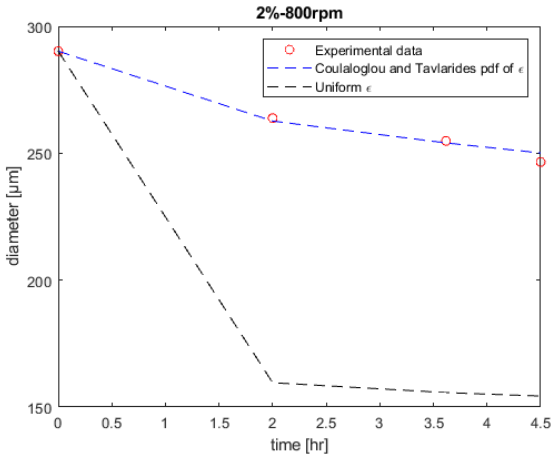

Figura 9 - La versione iniziale del modello permette un'ottima interpolazione dei dati sperimentali. In particolare, si può notare l'effetto positivo sulla presa in conto delle inomogeneità della turbolenza nello spazio.

Tuttavia, impiegando tale modello per l'interpolazione dei dati raccolti a viscosità più elevata, i risultati non sono soddisfacenti allo stesso modo, come si può vedere in figura 10:

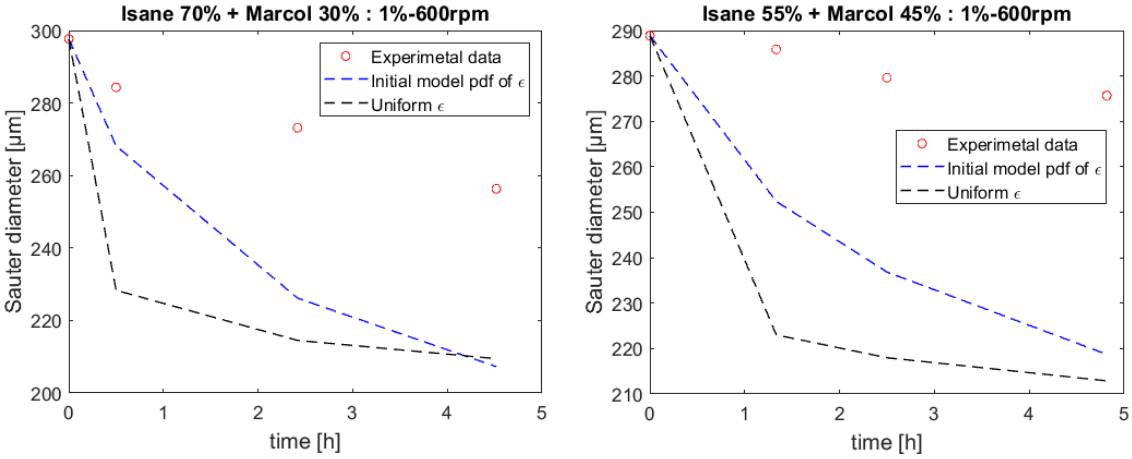

Figura 10 - Il modello iniziale non è in grado di interpolare i dati raccolti a viscosità più elevate (μ = 2,4 cP a sinistra, μ = 4,1 cP a destra). La causa è da ricercare nella sovrastima dell'energia dissipata dagli eddies.

Come già analizzato precedentemente, la prima versione del modello si basa sulla *legge dei -5/3 di Kolmogorov*, valida nell'*Inertial subrange*, ovvero per le gocce di "taglia medio-bassa". Tuttavia, quando si impiegano solventi più viscosi, tale range si sposta verso diametri maggiori, mentre il *Dissipation range* si amplia inglobando parte delle gocce precedentemente contenute nell'*Inertial subrange*. Calcolando infatti i nuovi limiti del *Dissipation range,* ovvero η e l_{DI} ($\approx 60\eta$) [13], si ottengono i seguenti risultati:

Tabella 3 - L'ampiezza del Dissipation range varia in funzione della viscosità.

	μ = 2,4 cP		**μ = 4,1 cP**	
ε	**η [μm]**	**l_{DI} [mm]**	**η [μm]**	**l_{DI} [mm]**
0,63	82,94	4,98	120,96	7,26
1	73,89	4,43	107,76	6,47
1,47	67,1	4,03	97,87	5,87

La viscosità è infatti direttamente contenuta nell'espressione di η, influendo positivamente su di essa. Ad esempio, osservando la distribuzione in figura 11 per il caso μ=2,4 cP a 600 rpm ottenuta a t=241 minuti, si può notare come la maggior parte delle gocce siano contenute nell'intervallo espresso nella tabella 3 (82,94 μm - 4,98 mm).

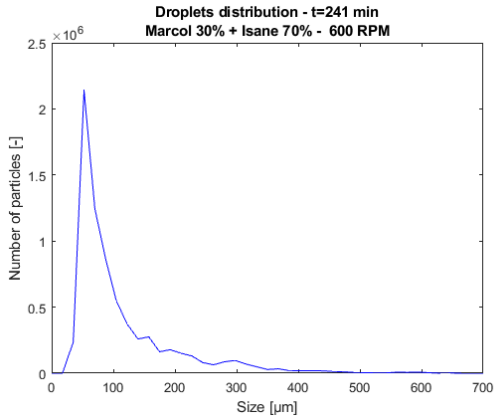

Figura 11 - Distribuzione della taglia delle gocce perla dispersione a viscosità 2,4 cP a 600 rpm. Tutte le particelle sono contenute nel Dissipation range.

Una situazione di questo tipo porta ad una sovrastima dell'energia dissipata realmente nel *Dissipation range* e, conseguentemente, ad una frequenza di rottura stimata superiore a quella reale. Per tal motivo, si è resa necessaria una riformulazione più completa dell'espressione matematica dello spettro d'energia dei vortici.

Modello avanzato

Nella seconda parte di questo lavoro è stato dunque necessario procedere alla validazione del modello nella sua versione riformulata. Per tal motivo, come primo step si è deciso di testare il nuovo approccio sulle precedenti esperienze, condotte prendendo l'Isane come solvente.

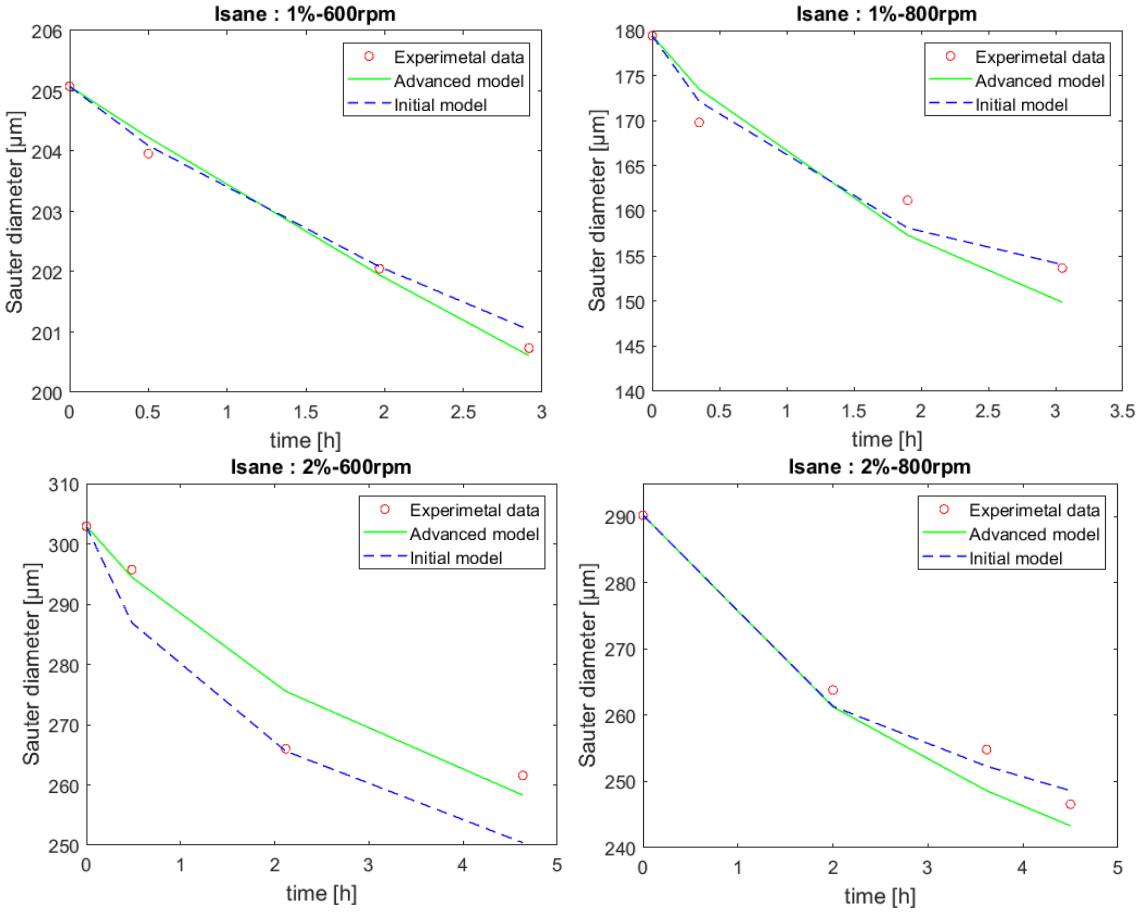

Figura 12 – I grafici riportano i risultati ottenuti interpolando i dati sperimentali ottenuti per solventi a bassa viscosità.

I risultati riportati in Figura 12 mostrano che entrambi i modelli forniscono un'ottima interpolazione dei dati reali. Questo perché in tali esperienze le particelle sono principalmente incluse nell'*Inertial subrange* e quindi entrambe le versioni forniscono una buona stima dell'energia dissipata.

A questo punto, il modello è stato impiegato per l'interpolazione dei dati raccolti a viscosità μ=2,4 cP, pari al doppio rispetto al caso dell'Isane. I grafici riportati in Figura 13 mostrano come la versione avanzata risulti essere più efficace della precedente. Come già anticipato, tale versione tiene conto della corretta quantità di energia dissipata dalle particelle presenti nel *Dissipation range*, a prescindere dalle percentuali di fase acquosa impiegate.

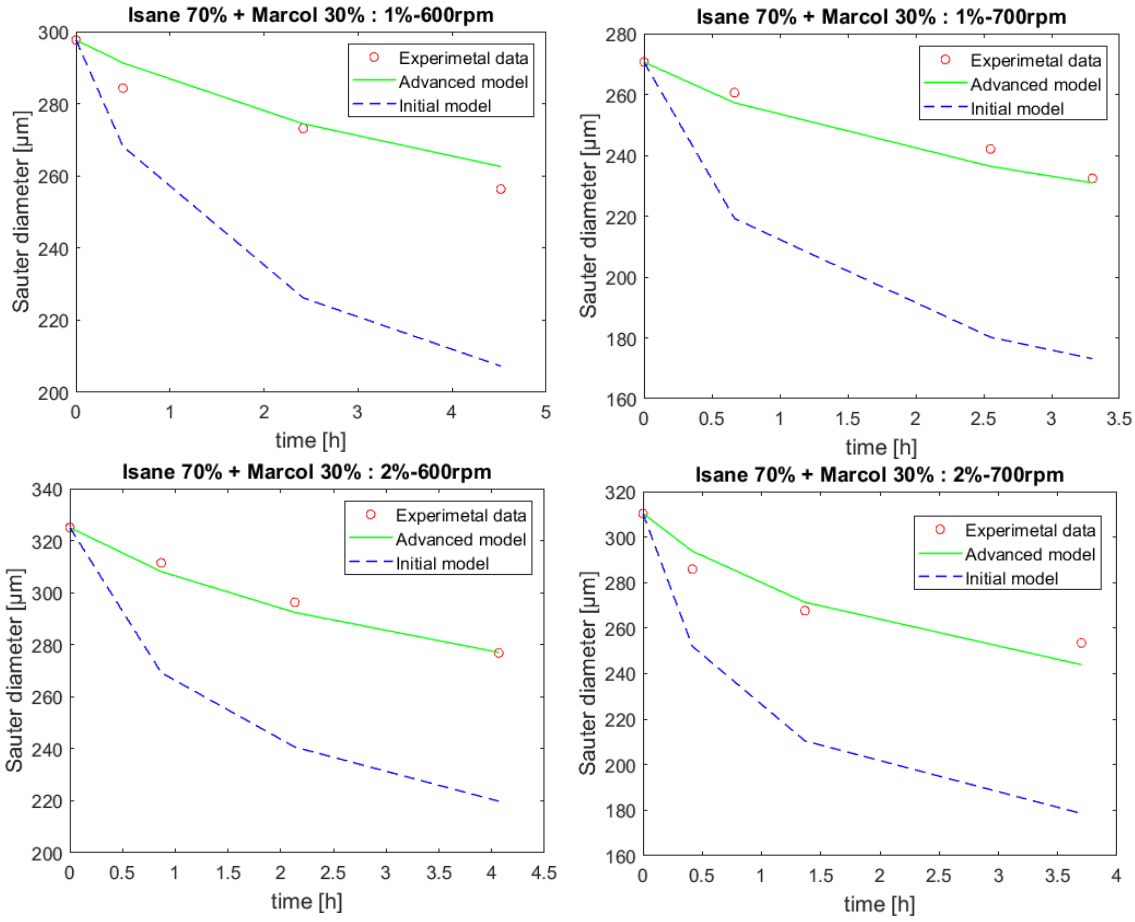

Figura 13 – I grafici riportano i risultati ottenuti tramite l'interpolazione dei dati sperimentali a media viscosità.

Lo stesso discorso vale per le esperienze condotte a μ=4,1 cP. In questo caso, come mostrato nella tabella 3, il *Dissipation range* risulta essere più ampio, quindi il modello iniziale conduce ad un errore superiore nella stima dell'energia dissipata.

In tal caso si nota, in figura 14, come la variazione temporale del diametro proceda più lentamente rispetto alle esperienze precedenti e come lo scarto tra i due modelli risulti essere più elevato. Nella prima versione del modello, infatti, l'energia dissipata risulta essere più elevata, causando una frequenza di rottura più alta. Per tal motivo, il modello iniziale fornisce un andamento che decresce più rapidamente rispetto al modello avanzato.

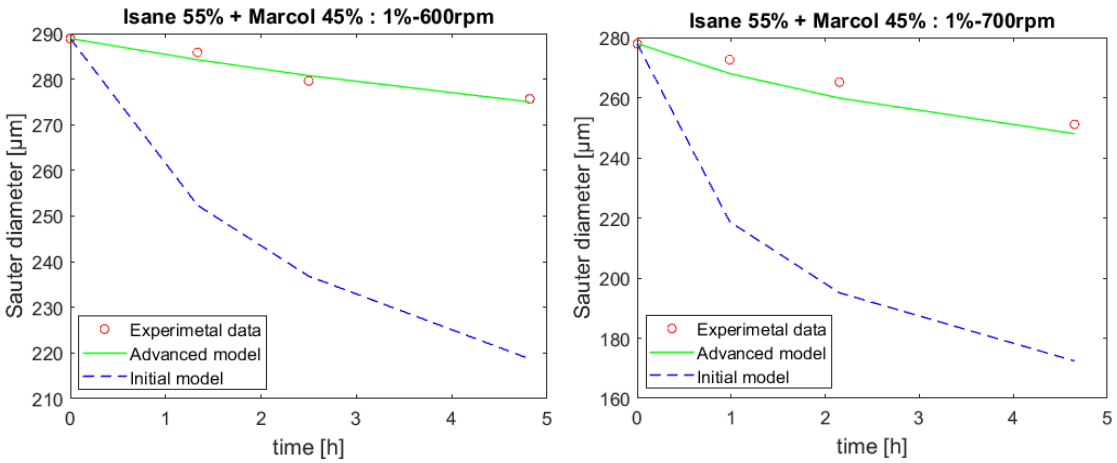

Figura 14 - Aumentando ulteriormente la viscosità il modello avanzato permette ancora di avere dei risultati soddisfacenti.

L'ipotesi iniziale valida per i nuclei di Coulalglou e Tavlarides, e quindi alla base di entrambe le versioni del modello, è che il sistema si trovi in condizioni di turbolenza. Nel caso di un reattore agitato, con sistema di agitazione costituito da una turbina Mixel TT, l'*Handbook of Industrial Mixing* fissa il Re limite a 10000 [3]. Tuttavia, secondo Hockey e Saouri [26] per un sistema analogo fissano un valore limite a circa 1500. Nella tabella seguente sono riportati i valori di Reynolds calcolati nei tre sistemi studiati in questo lavoro:

Tabella 4 - I numeri di Re confermano la condizione di piena turbolenza, a sostegno dell'ipotesi effettuata a priori.

Rotational speed	**Re number**		
[rpm]	**µ=1,2 cP**	**µ=2,4 cP**	**µ=4,1 cP**
600	22368	11611	7020
700	26096	13546	8190
800	29824	15481	9360

Se per i primi due sistemi studiati i valori di Re garantiscono un regime di piena turbolenza secondo entrambe le definizioni, nell'ultimo sistema studiato l'aumento di viscosità porta ad una riduzione dei valori di Re. Tuttavia, adottando l'ipotesi di Hockey e Saouri, il sistema puó essere ancora considerato in condizioni di turbolenza.

Limiti del modello

Aggiungendo il TBP al sistema, come visto in precedenza, la tensione interfacciale viene ridotta drasticamente.

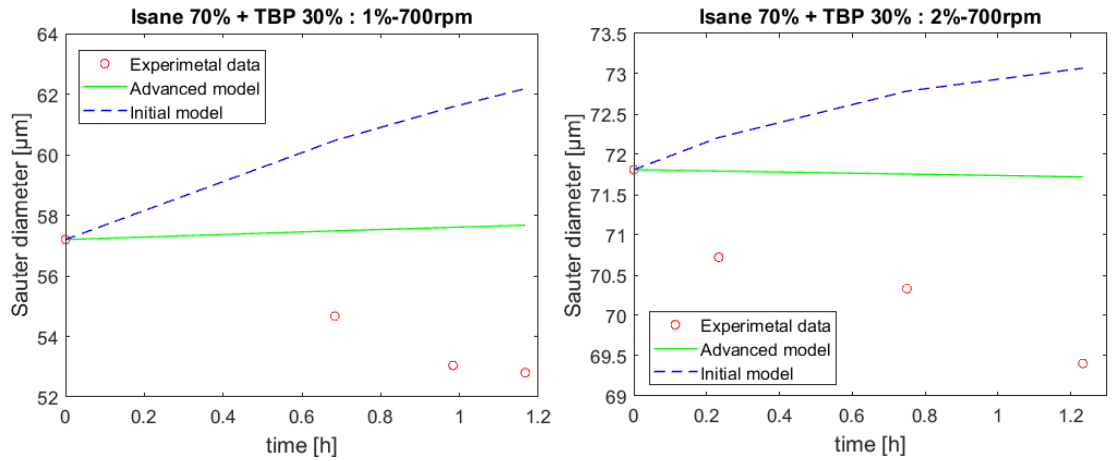

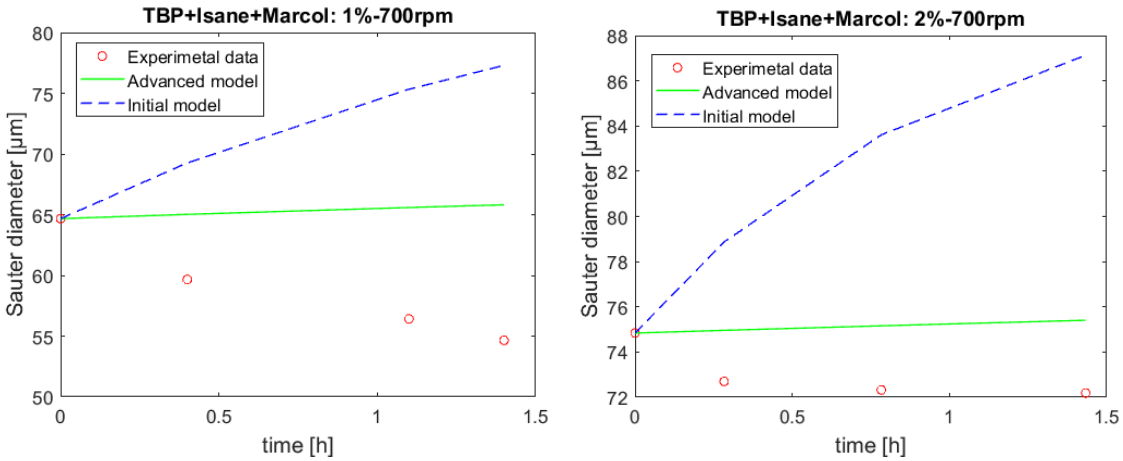

Figura 15 - Testando diverse viscosità, i due modelli non sembrano essere in grado di interpretare i dati sperimentali.

Questo porta ad una diminuzione delle dimensioni delle particelle nella distribuzione iniziale. Tuttavia, impiegando le due versioni del modello, si osserva che entrambe forniscono un'interpretazione incorretta dei dati sperimentali. In particolare si può notare come il modello iniziale sembri predire una predominanza del fenomeno di coalescenza, mentre per il modello avanzato l'evoluzione temporale della taglia risulta essere costante.

In questo lavoro si è tentato di fornire una spiegazione a tale problema. Diminuendo la tensione interfacciale tra le due fasi, la dimensione delle gocce della fase dispersa diminuisce al punto da essere addirittura inferiore alla *microscala di Kolmogorov*, uscendo così dal *Dissipation range*, come mostrato in figura 16. L'ipotesi di turbolenza in questo nuovo range non è più applicabile in quanto a prevalere sono le forze laminari. Per tale ragione, entrambe le versioni del modello risultano essere non idonee all'interpretazione dei dati sperimentali.

Tabella 5 – Per ogni esperienza sono riportati i valori della microscala di Kolmogorov.

	TBP + Isane	TBP + Isane + Marcol
Epsilon	**η [µm]**	**η [µm]**
0,63	58,74	100,20
1	52,34	89,27
1,47	47,53	81,07

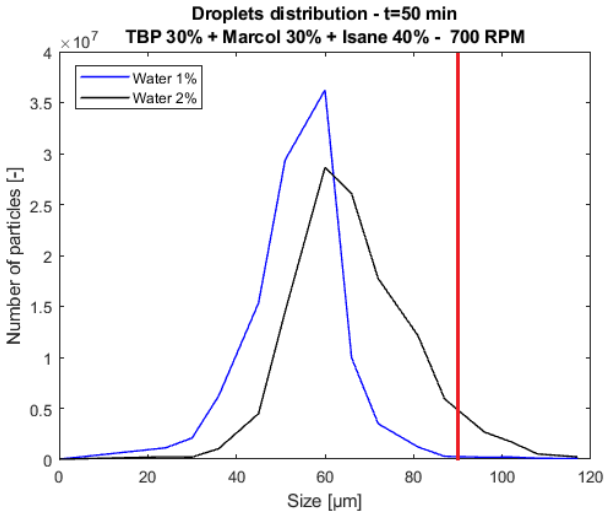

Figura 16 - In entrambe le distribuzioni presentate nel grafico, praticamente tutte le gocce hanno dimensione inferiore alla microscala di Kolmogorov.

CONCLUSIONI

Questo lavoro contiene informazioni riguardanti l'evoluzione delle particelle appartenenti alla fase dispersa in un sistema liquido-liquido bifasico reale. Tale operazione è stata possibile grazie all'impiego di un bilancio di popolazione, la cui soluzione, la *number density function* (NDF) permette di monitorare la variazione nel tempo e nello spazio del numero di particelle presentanti una specifica proprietà. In particolare, nelle equazioni integro-differenziali del bilancio di popolazione è necessario esprimere un *termine sorgente*, il quale nel caso di un'emulsione, è funzione dei fenomeni di rottura e di coalescenza. In letteratura sono disponibili diverse formulazioni matematiche (dette *kernels*) per la modellizzazione di tali fenomeni. Nel corso di questo lavoro si è scelto di impiegare i kernels di Coulaloglu e Tavlarides, ideali nel caso di dispersioni liquido-liquido in condizioni turbolente.

A differenza della formulazione classica nella quale la turbolenza è considerata uniforme nello spazio, in questo lavoro di tesi si è preferito adottare un modello che potesse prendere in conto la disomogeneità spaziale dei fenomeni turbolenti. Tale modello, proposto da Buffo et al. e Castellano et al. [22] è stato impiegato per l'interpretazione dei dati raccolti sperimentalmente adottando solventi più viscosi.

La risoluzione delle equazioni del bilancio di popolazione è stata possibile tramite l'utilizzo di un metodo numerico noto come Fixed Pivot Method. Tale metodo è stato implementato su MATLAB e ha permesso di poter comparare i diversi risultati.

In un primo momento, il modello proposto da Castellano et al. [22] è stato impiegato per la risoluzione delle equazioni, non producendo, tuttavia, i risultati sperati. La ragione dell'errata interpretazione dei dati sperimentali è da ricercare nella definizione di spettro d'energia dei vortici, adottata da Coulaloglou e Tavlarides. Adottando la *legge dei -5/3 di Kolmogorov*, i due kernels impiegati conducono ad una valutazione errata dell'energia dissipata dagli eddies più piccoli, contenuti nel *Dissipation range*. Per tal motivo, si è proceduto all'elaborazione di un nuovo modello, basato su una nuova formulazione matematica di spettro d'energia, fornita da Pope. Contemporaneamente, si è deciso di adottare una nuova definizione di velocità relativa tra i vortici, fornita da Davidson, la quale permette di tener conto in maniera più completa dei fenomeni che portano alla dissipazione di energia. Tale modello, detto *Advanced model*, è stato impiegato per l'interpretazione dei dati raccolti a viscosià superiore. Questa volta, i risultati prodotti si mostrano molto soddisfacenti, fornendo una corretta interpretazione dei dati sperimentali.

Tuttavia, impiegando un solvente a bassa tensione interfacciale, il modello non è più in grado di predire il comportamento reale delle gocce della fase dispersa, in quanto queste presentano dimensioni tali da essere inferiori alla *Microscala di Kolmogorov*. Infatti, per tali diametri le particelle disperse oltrepassano i limiti della turbolenza, uscendo dal *Dissipation range*, dove a prevalere sono le forze laminari. Non essendo più in condizioni di turbolenza, il modello cessa di essere valido.

In conclusione, il modello sviluppato permette di predire l'evoluzione delle particelle della fase dispersa per dei sistemi liquido-liquido. Tale scoperta potrà essere impiegata in ambito petrolifero, nucleare, alimentare, ecc., al fine di comprendere in maniera più efficiente alcune delle proprietà macroscopiche, come ad esempio lo scambio di materia.

In prospettiva per il futuro, tale lavoro andrà ad integrare il lavoro di dottorato svolto dal dr. Castellano, il quale si concentrerà maggiormente sull'interpretazione dei fenomeni di rottura e di coalescenza nelle colonne pulsate.

Possibili futuri sviluppi, potranno riguardare la comprensione e la modellizzazione dei fenomeni di rottura causati dalle forze laminari. L'interesse sarebbe quello di poter fornire una nuova versione dei kernels adoperabile *a priori*, cioé a prescindere dalla dimensione dalle gocce.

Inoltre, il modello potrebbe essere testato in condizioni operative differenti, adottando, ad esempio, un tenore superiore di acqua in fase dispersa. A tale incremento percentuale di fase dispersa, dovrà probabilmente corrispondere l'uso di simulazioni CFD multifasiche. Infine, sarebbe interessante poter studiare contemporaneamente lo scambio di materia tra le due fasi, adottando una nuova opportuna fase dispersa contente un componente chimico che si trasferisce.

Per concludere, tale lavoro sarà pubblicato prossimamente grazie alla collaborazione esistente tra il Politecnico di Torino e il CEA di Marcoule.

1. INTRODUCTION

A large variety of systems consists of different phases simultaneously. The simplest case is a two-phase system, such as gas-liquid, liquid-liquid, solid-liquid. These systems are often used in engineering for different purposes. Numerous examples could be found in several domains, from pharmaceutical to nuclear, from food industry to oil. Extraction, purification, leaching, fluidized bed reactors, etc. are the most known dispersion applications. Usually, we are interested in studying certain properties at the macroscopic scale. In a dispersed system the macroscopic behavior depends on the behavior of the particles. Both of them can be related by employing a population balance, which provides a mathematical-statistical approach to the problem.

Population balance equations are useful to define how properties related to the particle population (number, dimension, temperature, solute concentration, etc.) develop over time and space. The evolution of these properties affects the macroscopic properties of the entire system, such as the interfacial area, which has an important role in mass transfer process. PBEs are a set of integro-partial differential equations which describe the evolution of the particle distribution through the number density function (NDF). The NDF evolves over time, spatial location and internal coordinates. In this work, we will assume the NDF to be homogeneous in space and the size to be the only internal variable.

Historically, they were used in the early 60's to model the evolution of biological populations. However, its first simplified mathematical formulation was made by Landauand Rumer (1938) who identified PBEs for the distribution of energy among elementary particles. In the last 50 years, PBEs were used for various purposes in a very large field of applications [9]. In really recent years, a more completed formulation has been carried out to be extended to complex and multiphase processes [10].

In this study, thanks to the previous work done by Simone Castellano during his PhD at the CEA (Commissariat à l'Énergie atomique et aux Énergies alternatives, Marcoule center) and the Claude Bernard University of Lyon, the elaboration and validation of an improved model for liquid-liquid emulsions have been possible. In particular, a new method, using CFD and a 0D PBE model, has been compared with old methods and experimental data.

1.1 LIQUID – LIQUID SYSTEMS

Liquid-liquid systems play a key role in many industrial processes for instance polymerization, crystallization, or liquid-liquid extraction processes. Similar systems are usually employed in pharmaceutical, oil and gas, food-products, cosmetics, etc. In many cases systems consist of several components and macroscopic physical and rheological properties of the system (viscosity, density, etc.) are further complicated to be determined.

A system is defined as *immiscible* when two or more phases are insoluble and they appear as separate phases. Such systems are also known as *emulsions*. In this study we only refer to diphasic emulsions. Diphasic systems consist of a *dispersed phase*, representing the less concentrated phase, and a *continuous* or *matrix phase*. The dispersed phase is usually present in the form of spherical droplets distributed in the continuous phase; for this reason these systems can also be defined as *dispersions* [3].

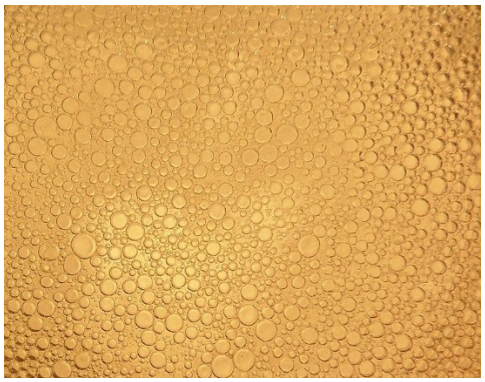

Figure 1.1 - Example of emulsion in polymerization process.

Agitation plays a key role in the evolution of droplets population in liquid-liquid dispersions, by promoting the *coalescence*, the combination of drops, or the *breakage*, which leads to smaller particles. It is interesting to evaluate the droplets size evolution over time, in order to evaluate certain macroscopic properties like the interfacial area between the two phases [5].

The intensity and the direction of convective flows produced by the agitation system, directly affect the droplets time path. Turbulent conditions allow to mutually promote coalescence and breakage. The predominant phenomenon depends on turbulence intensity. For instance, production of very fine emulsions requires a high degree of turbulence, which involves a significant amount of mechanical energy input.

1.1.1 Breakage and coalescence

Mechanical forces induced by the mixing system lead to drop deformations. The level of deformation depends on force intensity and direction but also on the surrounding fluid. In particular surface tension and viscous forces play a key role in breakage and coalescence mechanisms. Depending on the fluid motion conditions, droplets can deform differently. When the motion is laminar, shear and viscous stresses become important. On the contrary, when the system in turbulent conditions, pressure fluctuations become predominant. However, in drops coalescence and breakage, surface forces also depend on interfacial tension between the two phases [3].

Breakage is achieved when shear stresses become higher than surface tensions [5]. On the contrary, coalescence happens when two or more drops collide. The collision is followed by film drainage. Indeed, continuous phase is trapped between the droplets interface, a liquid film is formed and its thickness essentially depends on interfacial tension, relative velocity of the particles involved, and viscosity ratio between the phases. When the contact time is sufficiently high in order to make the film drainage possible, droplets can coalesce [4]. In the end, we can affirm that the coalescence rate depends on the collision rate and a coalescence efficiency. This latter is influenced by particles velocities, interfacial tension and viscosities [3].

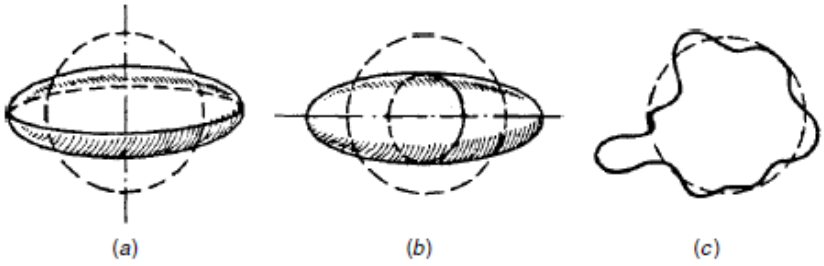

Figure 1.2 - Particle deformations: (a) lenticular, laminar forces; (b) cigar-shaped, colliding drops; (c) bulgy, pressure fluctuantions in turbulent conditions [3].

Mathematical definitions and other details concerning breakage and coalescence mechanisms are provided in chapter 2.

1.1.2 Dispersed phase characterization

The dispersed phase ratio is usually expressed as the volume fraction ϕ. Coalescence and breakage are affected by ϕ. For instance, coalescence rate is proportional to ϕ because higher dispersed fractions lead to higher collision frequency. By employing ϕ liquid-liquid dispersions can be characterized as follows [3]:

- $\phi < 0{,}01$, **dilute systems**: dispersed phase can be neglected since it does not influence flow conditions and droplets experience phase fluid forces. In particular, coalescence can be ignored until $\phi < 0{,}05$, because collisions rarely occur.
- $\phi < 0{,}2$, **moderately concentrated systems**: coalescence becomes more important; however, dilute system assumptions may still apply. For this kind of systems, drops do not affect the continuous phase field at the drop scale. Hence, the dispersion can be still considered composed by a single phase.

Other phenomena can affect drops size evolution, like the mass transfer. In particular, in the region of thinning film, mass transfer induces concentration gradients, which can either increase or decrease the probability of coalescence. Indeed, internal circulation within the drop and surface flows can affect the film drainage [4].

1.1.3 Industrial applications

Immiscible liquid-liquid systems find several applications throughout numerous domains. Extraction operations involve two immiscible phases, one in which multiple components are dissolved, and another one able to extract only the component of interest. The extraction is followed by a separation step, which allows to separate the two phases and, in the end, the component is recovered through a purification process.

Chemical reactions are basically controlled and influenced by interfacial area. For instance, the nitration of aromatic compounds needs the presence of a continuous acid phase (HNO_3 + H_2SO_4) and a dispersed phase in which organic components are dissolved. The reaction involves the ammonium ion, which is transported on the drop surface where reaction occur. The process is exothermic and it can be controlled through an efficient system of agitation and heat transfer between the phases [3].

Liquid-liquid dispersions heavily underlie food industry. Several products such as soft drink, mayonnaise, butter, cream rely on the use of emulsions. Behind their production, emulsifiers play a key role, by reducing interfacial tensions between the phases. For instance, the most common emulsifiers employed are amphiphilic proteins, phospholipids, polysaccharides, etc.[1] [2].

1.1.4 Common equipment

Hereunder, we give a brief overview of the most common equipment used to promote liquid-liquid dispersions.

1.1.4.1 Stirred tanks

Stirred tanks are heavily employed in emulsification processes. They also can be used for gas-liquid and solid-liquid systems. Crystallization, emulsion polymerization and pharmaceutical applications are generally carried out in batch conditions. Nevertheless, they can also be employed in continuous conditions (CSTR) for example in water waste treatment [3].

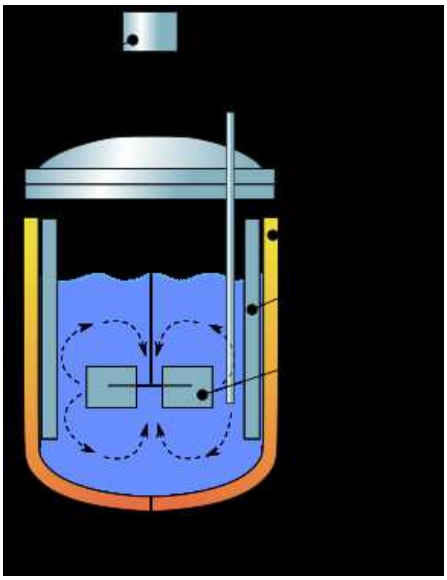

Figure 1.3 - Cross-sectional diagram of a stirred tanks reactor [*Wikipedia,* en.wikipedia.org/wiki/Continuous_stirred-tank_reactor]

A stirred tank consists of a vessel and a mixing system, usually composed by an impeller and lateral baffles which prevent recirculating flows. The most common employed impellers are Rushton turbines because their simple design, radial flow and high-power number. However, advanced agitators are recently designed for specific applications [6]. In this work a Mixel-TT propeller has been used since its design provides satisfactory mixing conditions and low shear.

1.1.4.2 High-pressure homogenizers (HPHs)

This kind of equipment consist of one or more valves which provide the spontaneous decompression of liquids from high pressures to atmospheric pressure. Upstream is placed a volumetric pump which allows to achieve a pressure max of 2000 bars. HPHs provide a very fine dispersion of the phases, approaching micron droplets sizes. For this purpose, HPHs are employed in emulsions presenting high dispersed-phase concentrations and high viscosities. They are indifferently used in batch or in continuous conditions [7].

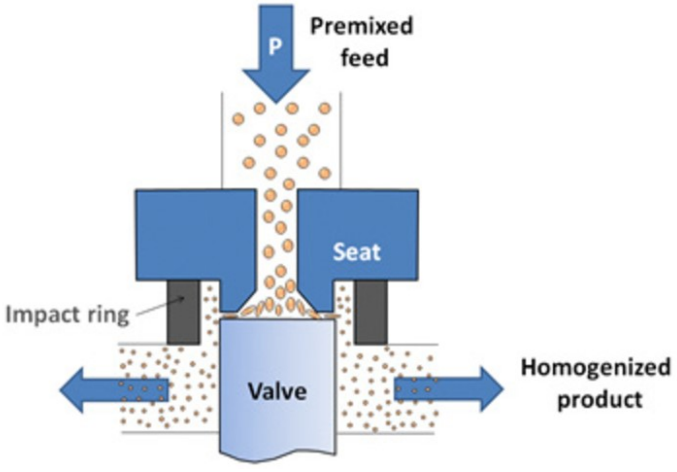

Figure 1.4 - High-pressure homogenizers diagram of operation [7].

High-pressure homogenizers are widely used in food manufactory, in the cosmetic industry and in the pharmaceutical area [1] [7].

1.1.4.3 Static mixers

Static mixers allow the continuous mixing of two or more liquid phases through a fixed motionless element. They are placed in a rigid pipe in which liquids are forced to pass, causing a pressure drop [3]. Their use in continuous processes represents a satisfactory alternative to conventional stirred tank reactors. Besides, this kind of equipment usually allows to achieve good performances at lower cost and at lower energy consumptions. Furthermore, the motionless component requires reduced maintenance operations. The mixing system is available in different materials of construction and in several designs, on the basis of specific applications [8].

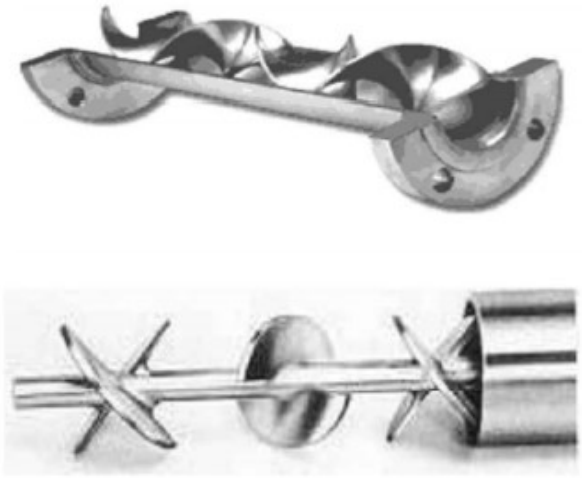

Figure 1.5 - Examples of motionless elements [8].

Static mixers are widely employed in adhesives and sealants production, wastewater treatment and chemical processing. Other applications can be found in oil and gas industry, for desalting crude oil, or in petroleum derivatives production (e.g. bitumen processing). Besides, static mixers also allow polymerization reactions.

1.2 POPULATION BALANCE MODEL FOR DEMOGRAPHY

Population balance equations find application in several domains. For instance, they could be used in order to build demographic predictive models, bearing in mind the phenomena characterizing a population evolution. In this case, the NDF variation over time represents the instantaneous growth rate, whose source terms are respectively the death rate and the birth rate. Furthermore, the model can also take in account probabilities for other events which could affect the demographic decline, such as population migrations, wars, etc. [27].

A funny example found in literature describes the evolution for a fish population in a controlled environment. The authors build a model on the base of the crystal growth model, highlighting numerous similarities. Crystals are born, grow up and may disappear. In the same way, fishes born, change size during their life and eventually die. A model of this type can provide important predictions about fish population size or age distribution. This information can aid in formulating harvesting plans, in choosing operating conditions with the purpose of increasing economic aspects for the fish farming domain [28].

1.3 AN INTERESTING INDUSTRIAL APPLICATION IN NUCLEAR

1.3.1 The nuclear context

Since 1950s, nuclear power has been representing a low-carbon alternative to produce electric energy. With about 450 power reactors all over the world, nuclear plants supply 2477 TWh of electricity, representing about 11% of the global electricity demand, according to the *World Nuclear Association*. However, nuclear power production is one of the most debated question because of its numerous risks parallels to benefits. In the last years, the growing public awareness about climate change has made nuclear the only high-density energy alternative to fossil fuels. On the other hand, the Chernobyl and Fukushima accidents have shown how dangerous nuclear could be for human health. Furthermore, radioactive waste management is one of the greatest nuclear power's critical issues. Different strategies have been put in place, according to technological evolution [29].

France represents the most nuclear dependent country in the world, with its 72% of electricity provided by nuclear, in 2017. In order to reduce risks and environmental impact, the French government has decided to adopt a strategy of nuclear fuel reprocessing. In this way, the nuclear fuel long-term storage can be reduced as well as the uranium mining exploitation. The process which allows to achieve these goals is the PUREX process. It is aimed, in a one hand at isolating and properly manage the more hazardous elements (fission products, minor actinides), while enabling the recovery and possible recycling of uranium and plutonium from the irradiated nuclear fuel. This is achieved by implementing several liquid-liquid extraction steps. In recent years, R&D studies are dedicated to the development of new solvents that would provide a better flexibility to the process (transposition to new nuclear fuel, simplification of the flow-sheet, etc.). Hence, they have built models to describe the phenomena taking places in the liquid-liquid contactors.

1.3.1 The PUREX process

The PUREX (Plutonium Uranium Refining by EXtraction) is a continuous hydrometallurgical extraction process. It is used to recover and separate uranium and plutonium from irradiated spent fuel. The difference from the other numerous existing extraction processes is the use of a mixture of tri-butyl phosphate (TBP) (30%) and an organic solvent (TPH, kerosene or dodecane). This phase is contacted with an aqueous phase (containing an important concentration of nitric acid), previously employed to dissolve the nuclear irradiated fuel. Thus, minor actinides and other fission products are separated from Pu and U, which will be recycled in the MOX fuel fabrication [11].

Once the irradiated nuclear fuel is dissolved in hot concentrated nitric acid, the process provides a series of liquid-liquid extraction steps to separate U and Pu from the fission products. The solution is contacted, counter-currently, with the organic phase (TBP + kerosene). In an extraction process it is indeed important to increase the interface area between the phases, in order to promote mass-transfer. Thus, the two phases are intimately mixed by mechanical agitation (in pulsed columns, mixer-settlers or centrifugal contactors) which creates a dispersion of nitric acid in the organic phase (and vice-versa) in the form of droplets [12].

After this step, the extracting solution is treated by partitioning the plutonium and the uranium, which after a decontamination process can be reemployed in the fuel fabrication process. Finally, the organic phase and the nitric acid solution are recovered by distillation, permitting a drastic reduction of waste and a lower required budget. The residual liquid still contains about 3% of radioactive products, such as minor actinides (Np, Am, Cm) and other fission products [12]. Thus, it is conditioned with a post-process of calcination and vitrification in a borosilicate matrix, which guarantees the physical-chemical stability necessary for the final storage. The diagram below resumes the process:

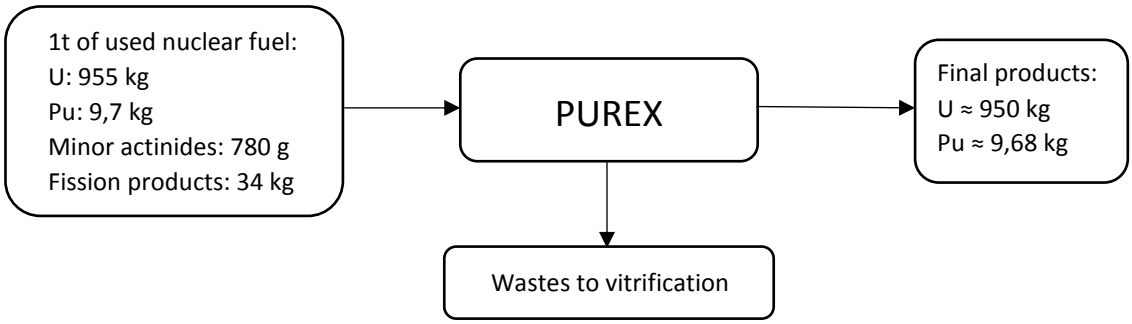

Figure 1.6 - PUREX process diagram

PUREX was developed by Herbert H. Anderson and Larned B. Asprey at the Metallurgical Laboratory at the University of Chicago. Today, the American company Energy Solutions held its rights. In France, the nuclear fuel reprocessing is carried out in the La Hague site, in northern France. The site has a capacity of 17000 tonnes per year, which makes it the most productive in the world. The extracted Plutonium is then recycled in Marcoule site (southern France), where the MOX fabrication takes place.

Alternative processes have been developed in the recent years. The French Areva (Orano) and CEA have proposed three PUREX based processes:

- COEX: it is based on the extraction and the precipitation of a U + Pu mix (U/Pu>20%) which can be directly used to MOX fabrication, without other conditioning.
- DIAMEX-SANEX: which separates long-lived radionuclides from the other fission products.
- GANEX: the goal is the production of a nuclear fuel for the Generation IV fast neutron reactors. For this purpose, it involves the co-precipitation of U, Pu and minor actinides by separating them from the other short-lived fission products.

Besides the development of these new processes, the use of alternative organic solvents or extracting molecules has been considered. While some of them appear promising from a thermodynamic point of view (distribution coefficient, selectivity) some hydrodynamics issues are likely to occur in their large-scale implementation. Indeed, in some cases, the loading of large amount of U in the organic phase has been observed to increase the viscosity of the oil, reaching sometimes up to 10 cP. This high viscosity level is quite unexplored in solvent extraction and emulsification processes, especially regarding the continuous phase.

1.3.2 Extraction equipment

As we saw, irradiated nuclear fuel is dissolved in high-concentrated nitric acid at high temperatures. The main reactions are the following:

$$PuO_2 + 4HNO_3 \rightarrow Pu(NO_3)_4 + 2H_2O$$

$$UO_2 + \frac{4}{3}(2+x)HNO_3 \rightarrow UO_2(NO_3)_2 + \frac{4}{3}(1-x)NO + 2xNO_2 + \frac{2}{3}(2+x)H_2O$$

where $0 < x < 1$, depending on the acid solution molarity.

After a clarification, the acid solution undergoes the extraction process. Pu^{4+} and UO_2^{2+} are dissolved in ionic form, thus the extraction is essentially a solvation by the extractive molecule (TBP), as shown below:

$$M^{n+} + nA^{-} + xTBP \rightarrow MA_n xTBP$$

In order to accelerate this reaction, it is important to increase interfacial surface between the phases. Hence, the design of liquid-liquid contactors requires the knowledge of the droplet size distribution. The process is essentially carried out with three equipment: pulsed columns, mixer settlers and centrifugal extractors [12].

1.3.2.1 The pulsed column

A pulsed column consists of a cylindrical shell in which the two liquids are mixed in continuum. Besides, a pulsation leg is connected to the base of the column, establishing a periodic movement of the air inside the leg. This periodic movement pushes the two phases back and forth against the packing elements of the column, enhancing the formation of a dispersion. Thus, the interfacial area between the two immiscible phases is dramatically increased, favoring the mass transfer. There are two possible configurations:

- Continuous organic phase: the column is already filled with the organic solvent and the water phase is injected from the top, forming the dispersed phase.
- Continuous water phase: in this case the column contains the water phase and the organic one circulates from the bottom to the top.

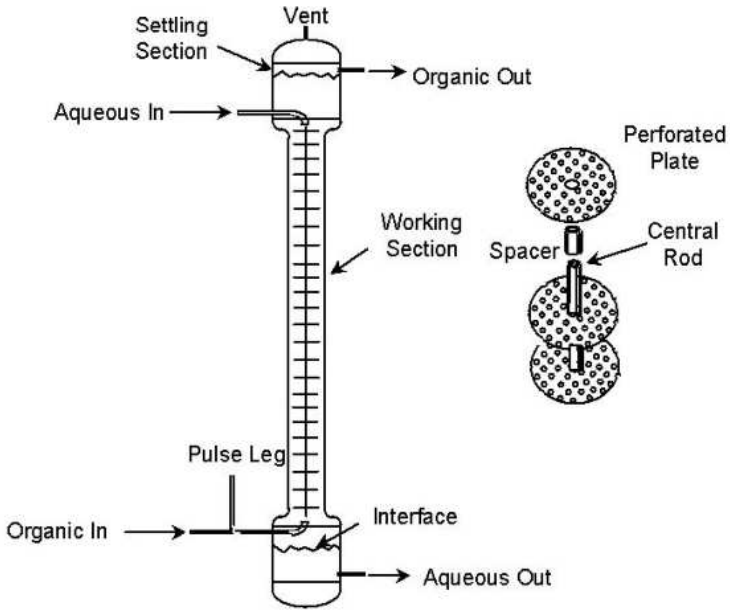

Figure 1.7 - A pulsed column

Its main advantage consists of the lack of rotating parts which reduces the need of maintenance in a highly radiotoxic environment. However, to achieve optimal separations, the column must have a significant height, generating issues in terms of costs and structure stability.

1.3.2.2 The mixer-settlers

The industrial equipment consists of several mounted-battery unities, called stages. Each stage is composed of a mixing chamber for mixing and a parallelepiped shaped one for decanting. The two phases are counter-currently injected in the mixing chamber, where the rotating movement of an impeller promotes the turbulence. The engine also allows to connect stages each other. The separation between the two phases occurs in the decanting chamber.

Figure 1.8 - A laboratory-scaled mixer settler [12]

The main advantages are the high efficiency, close to the theoretical one, and the possibility to work in a wide flow range. On the other hand, due to their size, the residence time can be too long, causing a solvent degradation.

1.3.2.3 The centrifugal extractors

The most complex device employed during the process is the centrifugal extractor. It consists of a cylindrical shell partitioned in two concentric chambers, with the same function of the mixer-settler's ones. However, this time in the middle of the vessel a rotor is placed to mix the phases and to push them outside, thanks to centrifugal force. Blades are arranged alternatively on the rotor, hence creating the mixing chambers. Each chamber is considered as a stage. Hence, the mixed liquid is rapidly accelerated to rotor speed and phase separation starts to occur in the second chamber. Finally, the light phase could be extracted thanks to pressure generated by the centrifugal force, while the heavy phase is recovered in the bottom section.

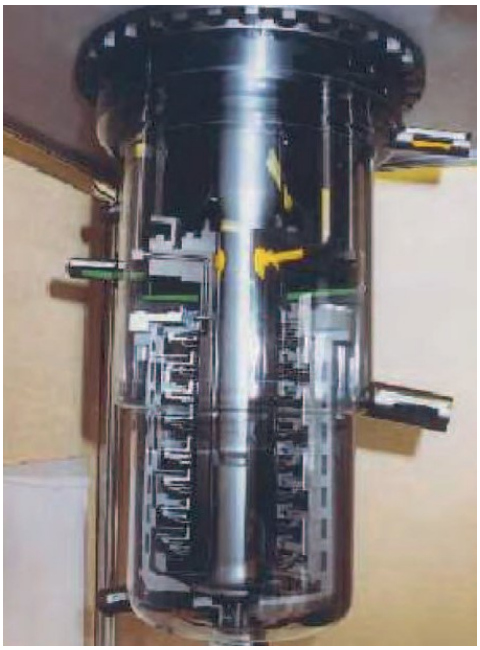

Figure 1.9 - A centrifugal extractor [12]

Centrifugal extractors provided the fastest separation, thanks to their very short residence time. This also allows to reach rapidly the equilibrium. However, the presence of the rotor does not

allow any solid particle, since they could obstruct the chambers. Furthermore, the use of a huge quantity of energy for the rotor motion causes an excessive heating that could affect the entire separation.

1.4 ORGANIZATION AND OBJECTIVES OF THE THESIS

The work started with a preliminary literature and theoretical review, concerning turbulence theories, PBEs models and kernels formulations. The PBE present source terms, the kernels, whose modeling is of crucial importance in order to accurately predict the time evolution of the NDF. The kernels are strongly influenced by the turbulent inhomogeneities in the liquid-liquid contactors. Therefore, a good description of turbulence leads to better results. Normally, the kernels available in the literature consider the droplets to have dimensions in the inertial subrange of turbulence, thus considering the Kolmogorov -5/3 law to apply. Increasing the viscosity of the continuous phase, the droplet dimension lies in the dissipation subrange, where the -5/3 law is not anymore valid. Therefore, the objective of this work is to improve the turbulence description of the kernels in order to make them valid for any droplet having dimension in the turbulent ranges. The thesis is the prosecution of Castellano previous work [22], who employed an alternative model to consider turbulent inhomogeneity in liquid-liquid contactors. After showing that this model is valid at low continuous phase viscosity, while it is not at high ones, an improved version will be proposed.

To test the model, different series of experiments were set in a stirred tank reactor. The first set was carried out increasing the viscosity of the continuous phase. In this phase, Castellano's model did not fit the experimental data. Hence, the improved model has been developed considering a formulation of the energy spectrum which included all the eddy sizes. On the basis of this approach, a new second order structure function has been defined and the Coulaloglou and Tavlarides' kernels reformulated. The improved model was fitted with the first set of experimental data collected at high viscosity, producing satisfactory results.

In the second part of the internship other experiments were performed in order to reproduce the PUREX process conditions, employing a TBP – Isane mixture. As previously mentioned, the viscosity has been varied, changing the composition of the mixture. However, both models were not able to fit experimental data. We have analyzed the possible reasons why the two approaches have produced similar results.

1.5 THE INTERNSHIP CONTEXT

This study has been developed at the CEA Marcoule. I have collaborated for six months with Simone Castellano, with whom I had the pleasure to work. This internship represents the final step of a double degree project which involves the Polytechnic of Turin (Italy) and the Ecole des Mines of Saint-Etienne (France). The enterprise is briefly described below.

1.5.1 Commissariat à l'Energie Atomique et aux Energies Alternatives (CEA)

The CEA is a public government-funded research center for the nuclear and alternative energies in France. The development and the innovation of the French energy sector is achieved thanks to synergies between engineers and researchers. CEA research activities are focused on four main domains to which correspond four main divisions:

- The division of nuclear energy (DEN), which works on low carbon energies (nuclear and renewable energies).
- The division of military applications (DAM), responsible for defense and security applications.

- The division of technological research (DRT), providing technological industrial research and innovation.
- The division of fundamental research (DRF), which is active in several scientific areas.

The ten CEA sites are distributed throughout the French territory. Furthermore, the CEA collaborates with several partners, such as universities, industrial and other research institutes all over the world. At present, more than 19800 people are engaged in the CEA activities producing almost 5000 scientific publications per year. The yearly budget amounts to 5 billion euros.

1.5.1.1 CEA Marcoule

The Marcoule site is directly involved in the reprocessing process of irradiated nuclear fuel. In particular, the site focuses on the development of separation processes and also on radioactive waste treatment and conditioning.

Furthermore, engineers and researchers work together in defining new safe methods for the decommissioning of old nuclear plants.

Marcoule was founded in 1955 and at present more than 1500 CEA's employees are working there, out of a total of 5000 people.

2 THEORETICAL BACKGROUND

2.1 TURBULENT FLOWS

A fluid turbulent motion is characterized by chaotic changes of the variables that characterize it. In particular, fluid velocity field and pressure field vary considerably and irregularly in position and time. Thus, the behavior of a turbulent flows seems to be completely random and unpredictable.

Turbulence is observable every day in our life: sea waves, river currents, wind motion. The air around an airplane or a vehicle and many other phenomena are turbulent. When turbulence is generated in a fluid motion, it is possible to see the formation of several unsteady vortices of different size. Turbulence is essentially caused by growing inertial forces which overcome viscous damping effect. The ratio between these two forces is the Reynolds number, which is a non-dimensional parameter describing fluid conditions. Generally, turbulence allows to increase the capacity of transporting and mixing fluids. This property is very important in many applications such as mixers, reactors and burners.

2.1.1 The energy cascade

Turbulence is a multiscale phenomenon. This interpretation was formulated for the first time by Richardson, who assumed that a turbulent motion is composed of eddies (swirling of fluid) of different sizes. Each size range is be characterized by a length-scale l_0; the largest eddies have a length-scale comparable to the flow scale $\mathcal{L}$. The main characteristic of an eddy is to be unstable. Hence, Richardson assumed that larger eddies break up in smaller ones. In this process, which Richardson assimilated to a cascade, the energy is transferred from one scale to the next one. The eddies breakage and the energy transfer continue until the Re becomes sufficiently low and the eddies are dissipated by viscous stresses. The dissipation turbulent kinetic energy rate is indicated with ε.

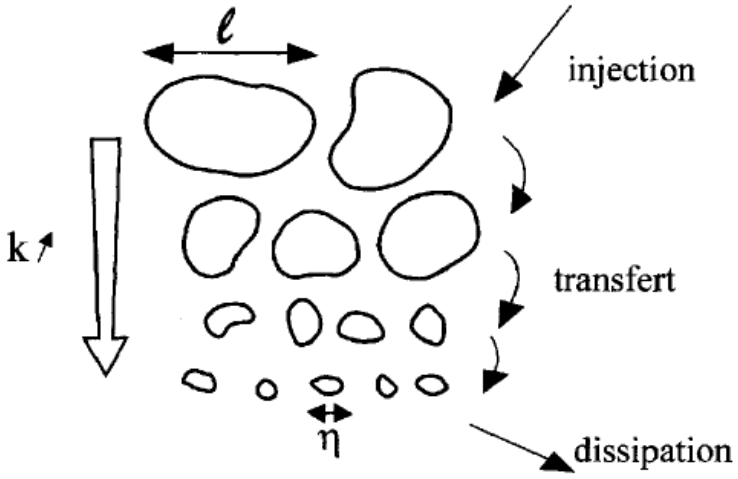

Figure 2.1 - The energy cascade proceeds towards smaller eddies

2.1.2 Kolmogorov's theory

According to the energy cascade theory, energy is completely dissipated when eddies reach a minimum size. Hence, it is necessary to define the minimal dimension an eddy can achieve. The answer to this question was provided by Kolmogorov, who postulated the following hypotheses:

I. LOCAL ISOTROPY: In a turbulent flow, the small-scale motions are statistically isotropic when the Reynolds number is sufficiently high. However, it is necessary to define this small-scale: Kolmogorov stated that local isotropy exists for eddies having a size $l < l_{EI}$ in the *Universal Equilibrium Range*, where $l_{EI} = l_0/6$. Directional and geometrical information of large eddies is lost during the transition to the small-scale.

II. FIRST SIMILARITY HYPOTHESIS: If Re is adequately high, the small-scale motion information depends uniquely on $\boldsymbol{\varepsilon}$ and $\boldsymbol{\upsilon}$, the kinematic viscosity, assuming a universal form. Starting from this hypothesis, it is possible to define a new length-scale for the smallest eddies, the Kolmogorov length scale:

$$\eta = \left(\frac{\upsilon^3}{\varepsilon}\right)^{1/4} \tag{2.1}$$

If we calculate the Reynolds number for the eddies having this size, we can easily find $Re_\eta = 1$. This result is consistent with the idea that the energy cascade proceeds through lower and lower Re.

Thus, by combining the hypotheses I and II, Pope states that *"On the small scales, all high-Reynolds-number turbulent velocity fields are statistically similar; that is, they are statistically identical when they are scaled by the Kolmogorov scales"*[13].

III. SECOND SIMILARITY HYPOTHESIS: If Re is sufficiently high, for the eddies having a length-scale in the range $l_0 \gg l \gg \eta$, the statistics assume a universal form which depends uniquely on ε. At this stage, it is convenient to split the *Universal Equilibrium Range* into two subranges, by introducing a length-scale $l_{DI} \approx 60\eta$: the *Inertial subrange* ($l_{EI} > l > l_{DI}$) and the *Dissipation range* ($l < l_{DI}$). For the former, both the similarity hypothesis can be employed, where viscous effects are negligible compared to inertial effects. On the contrary, in the *dissipation range*, only the first similarity hypothesis is valid, since viscous effects are important.

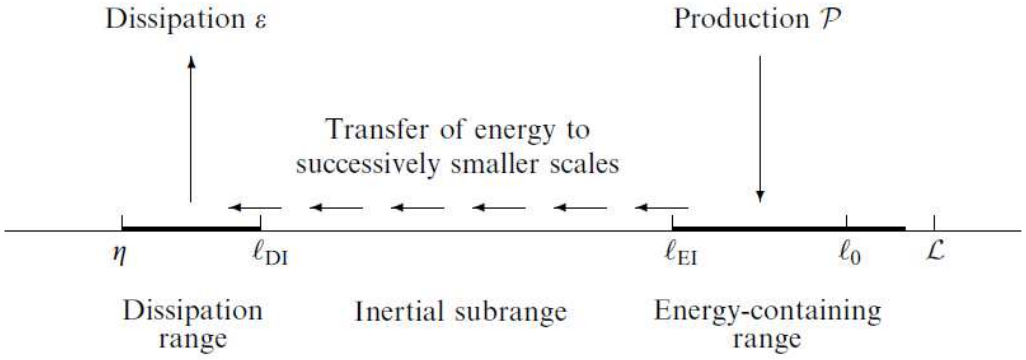

Figure 2.2 - The ranges characterizing small wavelength eddies [13]

2.1.3 The energy spectrum

As told above, the turbulence is characterized by an energy transfer from bigger to smaller eddies. Each eddy is characterized by a turbulent kinetic energy that depends on his size. The energy spectrum represents the distribution of turbulent kinetic energy as function of the wavelength of the eddy. Starting from his hypothesis, Kolmogorov showed that the energy spectrum has a well-defined form in the Inertial Subrange, confirmed by experimental results. Indeed, the spectrum shows a linear tendency (in a logarithm graph) with a slope of *-5/3*.

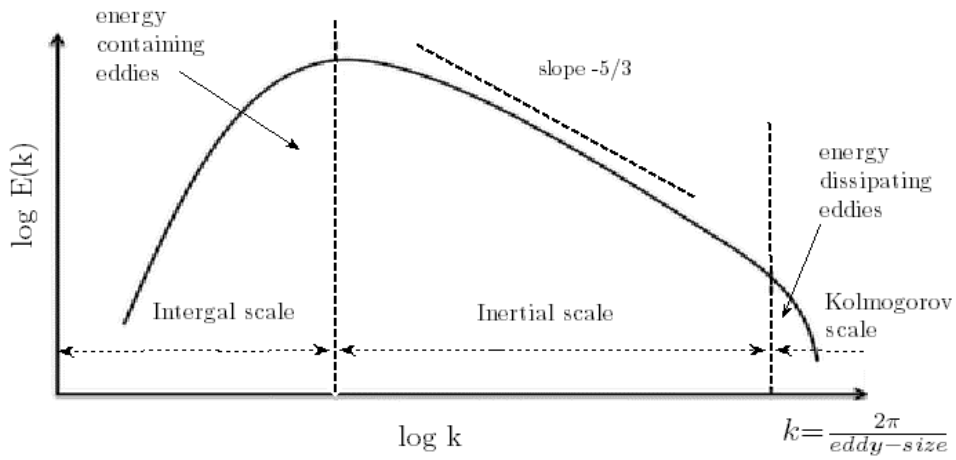

Figure 2.3 - Energy spectrum behavior across the entire wavelength scale [30]

Instead, applying only the first similarity hypothesis, in the *Universal Equilibrium Range* the velocity fluctuations depend on κ ($\kappa = 2\pi/l$), ε and ν. Therefore, the energy spectrum $E(\kappa)$ can be expressed as [13]:

$$E(\kappa) = \varepsilon^{\frac{2}{3}}\kappa^{-\frac{5}{3}}\Psi(\kappa\eta) \tag{2.2}$$

Where, $\Psi(\kappa\eta) = (\eta\kappa)^{\frac{5}{3}}\varphi(\kappa\eta)$, with $\varphi(\kappa\eta)$ is a universal non-dimensional function (the *Kolmogorov spectrum function*). However, according with the second similarity hypothesis, in the inertial subrange the spectrum depends uniquely on ε. This implies that the function $\Psi(\kappa\eta)$ becomes constant, since it is independent of the variables κ and η. The *Kolmogorov spectrum* assumes the following final form, also known as *the Kolmogorov -5/3 spectrum*:

$$E(\kappa) = C\varepsilon^{\frac{2}{3}}\kappa^{-\frac{5}{3}} \tag{2.3}$$

C is the *universal Kolmogorov constant* and it is widely experimentally demonstrated that it assumes a value of $C \approx 1{,}5$.

As we will see in the paragraph 2.4, Coulaloglou and Tavlarides used equation (2.3) and the second order structure function to describe eddy behavior. Indeed they assumed the droplets to have always dimension in the *Inertial subrange*. However, in liquid-liquid contactors, droplets may have dimensions in the *Dissipation range*, where the second order structure function also depends on υ. Hence, employing Coulaloglou and Tavlarides kernel in the latter case leads to erroneous results, since we are considering that the linear -5/3 tendency is still valid in the last part of the curve in figure 7. For this purpose, we replaced the Kolmogorov's definition with a more complex formulation, which accounts for the viscous effects in the *Dissipation range*.

2.1.4 Relative velocity between two points

From this section on, we replace the length-scale l with the corresponding wave number $\kappa = 2\pi/l$. The energy spectrum is strictly connected with the velocity correlation function. Namely, this function does not depend on time and position. For this reason, we could say that turbulence is homogenous and isotropic. Thus:

$$Q_{ij} = \langle {v'}_i(x){v'}_j(x,r)\rangle \tag{2.4}$$
$$v^2 = {v^2}_x = {v^2}_y = {v^2}_z \tag{2.5}$$

The term ${v'}_i$ represents eddies velocity fluctuation. For instance, if we are considering its x-component, this function tells us if ${v'}_x$ at one point is correlated to ${v'}_x$ at an adjacent point.

Furthermore, the autocorrelation function can be related with the *second-order structure function* and with the energy spectrum. In particular, these function gives precious information about the eddy size distribution and the kinetic energy distribution. By defining the x-component of the second-order longitudinal structure function in terms of longitudinal velocity increment:

$$\langle [\Delta u(r)]^2 \rangle = \langle [u_x(x+r) - u_x(x)]^2 \rangle \tag{2.6}$$

With reference to the Kolmogorov' theory, two possible mean square velocities can be expressed, depending on the range considered [14].

- INERTIAL SUBRANGE:

$$\overline{u^2(r)} = C_1(\varepsilon r)^{\frac{2}{3}} \tag{2.7}$$

- DISSIPATION RANGE:

$$\overline{u^2(r)} = C_2\left(\frac{\varepsilon}{\upsilon}\right) r^2 \text{ (if } r \to \eta) \tag{2.8}$$

According to the Kolmogorov' hypotheses, in the inertial subrange the mean square velocity depends uniquely on the ε while in the dissipation range also depends on the υ. By using these definitions, it is possible to evaluate the energy spectrum.

2.2 COMPUTATIONAL FLUID DYNAMICS

Since the beginning of the XX century, several numerical methods have been implemented and adopted for solving differential equations. In the past, engineers, mathematicians and physicians used to carry out a solution by hand and using desk calculators. Later, thanks to the advent of digital computers, it has been possible to accelerate significantly the computation time. *Computational fluid dynamics* (CFD) is the study of fluid dynamics through the solution of equation with the computers.

2.2.1 Equations

In order to have a set of equations which describes fluid motion, it is assumed the fluid to be continuous. This hypothesis concerns fluid properties but also fluid velocity field. Among the most important variables there are the density $\rho(x,t)$ the velocity $U(x,t)$, and the pressure, which depend on position and time. In mathematical terms, a turbulent flow can be described through the following equations

2.2.1.1 The continuity equation

The continuity equation is also known as the mass-conservation equation [31]:

$$\frac{\partial \rho}{\partial t} + \nabla \cdot (\rho U) = 0 \tag{2.9}$$

Since we are considering constant-density flow, which means that ρ does not depend on x and t, the equation can be simplified as follows:

$$\nabla \cdot U = 0 \tag{2.10}$$

2.2.1.2 The momentum equation

The momentum equation results directly from Newton's second law. Hence, for a fluid element, its velocity changes are related with surface (stress tensor τ_{ij}) and body (gravity) forces experienced by the fluid.

$$\rho \frac{DU_j}{Dt} = \frac{\partial \tau_{ij}}{\partial x_i} - \rho \frac{\partial \Psi}{\partial x_j} \tag{2.11}$$

Where

- $\tau_{ij} = -P\delta_{ij} + \mu\left(\frac{\partial U_i}{\partial x_j} + \frac{\partial U_j}{\partial x_i}\right)$ is the stress tensor for a constant-properties fluid is (P is the pressure and μ is the dynamic viscosity).
- $\Psi = gz$ is the gravitational field potential assuming a constant acceleration.

Now, by considering that we are working on a constant-properties fluid and by including the continuity equation, we can simplify the momentum equation as follows [31]:

$$\frac{DU}{Dt} = -\frac{1}{\rho}\nabla p + \upsilon\nabla^2 U \tag{2.12}$$

Where $p = P + \rho\Psi$ is the modified pressure and $\upsilon = \mu/\rho$ is the kinematic viscosity. The second term on the right side of the equation can be explained as the difference between the velocity at a point and the mean velocity in a small surrounding volume. For a Newtonian fluid, this term works as a diffusion of momentum, depending on viscosity.

The equations (2.10) and (2.12) represent the well-known ***Navier-Stokes equations*** [31]. They can be analytically solved in very few cases. Otherwise, a solution could be found by using the DNS (direct numerical simulation) methods, available only for moderate Reynolds numbers, since the computational time varies with Re^3. It consists of solving the entire range of spatial and temporal scales of the turbulence. For this reason, the DNS method is computationally really expensive.

2.2.1.3 Mean flow equations

For flows having high-Re, which are more frequent in engineering applications, a statistical approach could be a good alternative. Thus, instead of describing the flow in terms of velocity $U(x,t)$ it is possible to use the mean velocity field $\langle U(x,t)\rangle$. In fact, the velocity can be rewritten as the sum of two components, its mean and its fluctuation $u(x,t)$:

$$U(x,t) = \langle U(x,t)\rangle + u(x,t) \tag{2.13}$$

By replacing this definition in the Navier-Stokes equations we obtain the **Reynolds-averaged Navier-Stokes equations (RANS)** [31]:

$$\nabla \cdot U = \nabla \cdot (\langle U\rangle + u) = \nabla \cdot \langle U\rangle = 0 \tag{2.14}$$

$$\frac{\bar{D}\langle U_j\rangle}{\bar{D}t} = -\frac{1}{\rho}\frac{\partial\langle p\rangle}{\partial x_j} + \upsilon\nabla^2\langle U_j\rangle - \frac{\partial\langle u_i u_j\rangle}{\partial x_i} \tag{2.15}$$

The three terms on the right side represent respectively the isotropic stress, the viscous stress and the apparent stress caused by the velocity fluctuation. This latter is also known as the **Reynolds stress tensor**. It constitutes a symmetric second-order tensor in which the diagonal components are normal stresses and the off-diagonal components are the shear stresses. In particular, the half trace of the Reynolds stress tensor represents the turbulent kinetic k:

$$k = \frac{1}{2}\langle u_i u_i\rangle \tag{2.16}$$

2.2.1.4 The vorticity equation

In turbulent flows, an important variable that we must consider is the vorticity. In a continuous medium, vorticity describes the local spinning motion of a point.

$$\omega = \nabla \times U \tag{2.17}$$

Starting from Navier-Stokes equations (2.12), it is possible to determine a mathematical formulation for ω. Since the left side term $\frac{DU}{Dt}$ represents the convective derivative, it can be split as follows:

$$\frac{DU}{Dt} = \frac{\partial U}{\partial t} + U \cdot \nabla U \tag{2.18}$$

In particular, the inertia term $U \cdot \nabla U$ can be rewritten as:

$$U \cdot \nabla U = \frac{1}{2}\nabla(U \cdot U) - U \times (\nabla \times \mathrm{U}) = \nabla\left(\frac{U^2}{2}\right) - U \times \omega \tag{2.19}$$

Now, it is necessary to apply the differential operator **curl** ($\boldsymbol{\nabla}\times$) to both side of the Navier-Stokes equations. Thus, for an incompressible fluid in fixed reference frames, left side terms become:

$$\nabla \times \frac{\partial U}{\partial t} = \frac{\partial(\nabla \times U)}{\partial t} = \frac{\partial \omega}{\partial t} \tag{2.20}$$

$$\nabla \times (U \cdot \nabla U) = (U \cdot \nabla)\omega - (\omega \cdot \nabla)U \tag{2.21}$$

For the right side, the first term becomes 0 because of the following identity:

$$\nabla \times \nabla(scalar) = \nabla \times \nabla p = 0 \tag{2.22}$$

On the contrary, for the second term we have:

$$\nabla \times (\upsilon \nabla^2 U) = \upsilon \nabla^2 \omega \tag{2.23}$$

Finally, putting together equations (2.20) – (2.23), we obtain [31]:

$$\frac{\partial \omega}{\partial t} + U \cdot \nabla \omega = \frac{D\omega}{Dt} = \omega \cdot \nabla U + \upsilon \nabla^2 \omega \tag{2.24}$$

In the equation 24, the first term on the right side describes the phenomenon of vortex-stretching.

2.2.1.5 The closure problem

For a three-dimensional system, it is necessary to solve four independent equations which determine the mean velocity field: the three components RANS equations and the mean continuity equation. In this equations system there are more than four unknowns, the three mean velocities $\langle U_j \rangle$, the mean pressure $\langle p \rangle$ and also the Reynolds stresses. As it is, the system cannot be solved and it is said to be unclosed. Hence, in order to *close* the set of equations, we need to model the Reynolds stress term. Thus, the goal is to remove the fluctuating part of the velocity, by expressing them as a function of the mean flow.

Boussinesq's hypothesis is employed to overcome the closure problem. Indeed, it is possible to model the Reynolds stresses by introducing a new proportionality constant, the turbulent viscosity υ_T [31].

$$-\frac{\partial \langle u_i u_j \rangle}{\partial x_i} = \upsilon_T \left(\frac{\partial \langle U_i \rangle}{\partial x_j} + \frac{\partial \langle U_j \rangle}{\partial x_i}\right) - \frac{2}{3} k \delta_{ij} \tag{2.25}$$

Where is δ_{ij} the Kronecker delta.

In order to define v_T, several approaches have been developed which provide one or more additional equations. The most known turbulence models are:

- **Mixing-length model**: the mixing-length concept, introduced by Prandtl [32], considers that turbulent viscosity must vary by approaching the wall of the turbulent motion. This variation is proportional to the square mixing-length and to the velocity gradient near the wall.
- **Spalart-Almaras**: this model provides just one additional equation and it is largely used in aerospace applications.
- **k-epsilon**: this model is the most used. It provides a general description of turbulence by introducing two transport equations which describe k, the turbulent kinetic energy, and ε, the ***turbulent dissipation rate***. The purpose for using the k-epsilon model is to improve the mixing-length concept by describing accurately turbulent length-scales. It can be employed for planar shear layers and recirculating flows, where the pressure gradient is relatively small. For this reason, in this work this method was used. The model includes the following equations [31]:

$$\frac{\partial(\rho k)}{\partial t}+\frac{\partial(\rho k u_i)}{\partial x_i}=\frac{\partial}{\partial x_j}\left[\left(\mu+\frac{\mu_t}{\sigma_k}\right)\frac{\partial k}{\partial x_j}\right]+G_k-\rho\varepsilon \tag{2.26}$$

$$\frac{\partial(\rho \varepsilon)}{\partial t}+\frac{\partial(\rho \varepsilon u_i)}{\partial x_i}=\frac{\partial}{\partial x_j}\left[\left(\mu+\frac{\mu_t}{\sigma_\varepsilon}\right)\frac{\partial \varepsilon}{\partial x_j}\right]+C_{1\varepsilon}\frac{\varepsilon}{k}G_k-C_{2\varepsilon}\rho\frac{\varepsilon^2}{k} \tag{2.27}$$

- **k-omega**: as the k-epsilon model, two partial differential equations have been added in order to describe k and ω, the specific rate of dissipation.

2.2.2 Numerical methods for computational fluid dynamic

Navier-Stokes equations constitutes a nonlinear partial differential equations system, which rarely present an analytical solution, due to their complexity. However, they can be solved through numerical methods. Numerical methods allow to evaluate certain variables at only discrete points. Therefore, they do not provide a "continuous" solution, valid throughout the entire domain.

Hence, the computational approach provides a simplification of Navier-Stokes equations through two processes: the **space discretization** and the **equation discretization**. The first one consists in replacing continuum space with a finite number of points, called **mesh** or **grid**. Intuitively, the finer is the discretization, the higher is the accuracy of the numerical approximation. We can state that the numerical error tends to zero when grid dimension tends equally to zero. However, meshes too fine can lead to a considerable increased of the computational time. Two kind of grids can be usually implemented [15]:

- **Structured**, which are composed by families of lines (within a Cartesian or curvilinear system) whose intersections constitute the points in which variables will be determined. They form several cells which can be identified by an index *(i, j)* in 2D and *(i, j, k)* in 3D.
- **Unstructured**, nodes distribution in the plane or in the space follows an irregular pattern. In contrast with structured grids, these ones need to be connected through polynomials (in the plane) or polyhedrals (in the space).

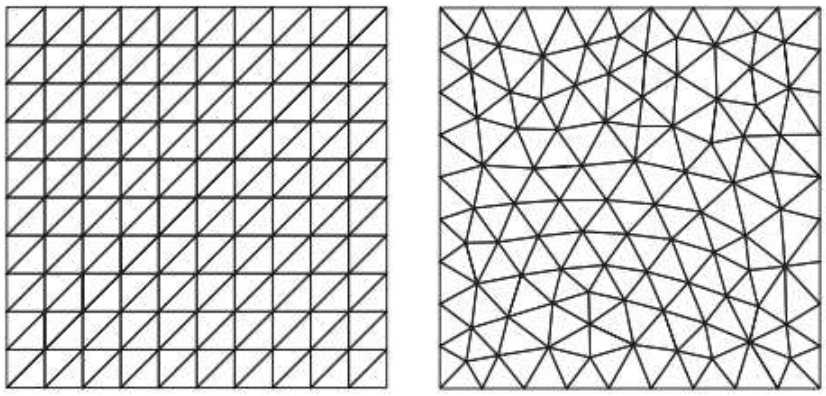

Figure 2.4 - On the left an example of structured mesh, on the right an unstructured one [15].

The second step consists in discretizing the equations. This process allows the transformation by partial differential equations in discrete **algebraic expressions**, linear or non-linear. In this way, it is possible to evaluate the unknown variables in each point of the mesh.

The mathematical model selected in order to model our system can be considered **steady state** or it can be **time-dependent**. The choice of the one or the other depends on the nature of the flow. A flow in which boundary conditions vary over time will be modeled with a time-dependent model. For steady state or stationary problems, however, it is possible to follow solutions evolution over time by employing an unsteady formulation. This technique is also known a *pseudo unsteady* and it does not require a strong time accuracy since we are not interested in the transient behavior of the flow. Besides, Hirsch stated that [16]:

"…at small enough length scales all turbulent flow configurations are unsteady […]. Therefore, we recommend working with the time dependent-equations."

That is why, even with steady state problem, it is usual to employ time-dependent algorithms. Furthermore, time-dependent formulations can be split in two families, **explicit** or **implicit**. The first one can calculate variables of a system at a time $t + \Delta t$ by knowing their values at a time t. On the contrary, implicit methods has to solve equations by using both the current state t and the later one $t + \Delta t$.

Moreover, three equation discretization methods can be employed:

- Finite difference method (FDM).
- Finite volume method (FVM).
- Finite element method (FEM).

The FDM is a differential scheme based on Taylor expansions. By neglecting higher-order terms, it may bring us in some approximation error. The FVM and the FEM are integral schemes based on the integration across surfaces, which allows to reduce the chance of error.

On the other hand, differential schemes are generally easier to implement and allow short calculation time. Besides, the error can be minimized when a regular structured mesh is employed.

Integral schemes are slower in terms of computational time but they can be applied when the grid is unstructured.

2.2.2.1 Finite difference method

The FDM is based on derivative formulation of conservative laws and on Taylor expansions and it is the simplest one to apply. Nevertheless, it requires to be applied uniquely on structured meshes [16].

By considering a function $u(x)$, its derivative for a point x is:

$$u_x = \frac{\partial u}{\partial x} = \lim_{\Delta x \to 0} \frac{u(x + \Delta x) - u(x)}{\Delta x} \tag{2.28}$$

When the limit is removed, we obtain a *finite difference*.

From equation (2.28), we can obtain:

$$u(x + \Delta x) = u(x) + \Delta x \frac{\partial u}{\partial x} \tag{2.29}$$

Which represents the Taylor expansion of the function $u(x)$ truncated at the first order. It can be expanded as follows:

$$u(x + \Delta x) = u(x) + \Delta x \frac{\partial u}{\partial x} + \frac{\Delta x^2}{2} \frac{\partial^2 u}{\partial x^2} + \frac{\Delta x^3}{3!} \frac{\partial^3 u}{\partial x^3} + \cdots \tag{2.30}$$

The power of Δx represents the **order of accuracy** of the derivative approximation.

Now, once the derivative definition is given, we can resume the most important finite difference approximation. At a point *i*, finite difference approach depends on the order that we select want which direction we are moving in the space. Thus, we have:

- **First order forward difference:**

$$u_i = \frac{u_{i+1} - u_i}{\Delta x} + O(\Delta x) \tag{2.31}$$

- **First order backward difference:**

$$u_i = \frac{u_i - u_{i-1}}{\Delta x} + O(\Delta x) \tag{2.32}$$

- **Second order approximation (central difference formula):**

$$u_i = \frac{u_{i+1} - u_{i-1}}{2\Delta x} + O(\Delta x^2) \tag{2.33}$$

When also time-dependence is included, for a time n, moving towards an instant $n + 1$ and by adopting the central difference scheme, we obtain:

- **Explicit Euler method:**

$$\frac{{u_i}^{n+1} - {u_i}^n}{\Delta t} = \frac{{u_{i+1}}^n - {u_{i-1}}^n}{2\Delta x} \tag{2.34}$$

- **Explicit Euler method:**

$$\frac{{u_i}^{n+1} - {u_i}^n}{\Delta t} = \frac{{u_{i+1}}^{n+1} - {u_{i-1}}^{n+1}}{2\Delta x} \tag{2.35}$$

2.2.2.2 Finite volume method

The FVM is characterized by the discretization of the conservation law (using the integral form) in a given space. This method is widely employed since its simplicity and its easy adaptation for structured and unstructured grids. It is based on the concept of **cell-averaged values**: once the mesh is defined, the method assumes that each nodes of the grid is locally surrounded by a local **control volume** (like a small cell) in which conservation law is discretized and solved. This allows the conservation of the main flow quantities such as mass, energy and momentum, which allows a *conservative discretization* [16].

The method is based on the **divergence theorem**, which states that for source terms the volume integral of the divergence is equal to the net flow across the surface which delimits the

volume. Let consider the following equation in order to illustrate the general conservation law [33]:

$$\frac{\partial u}{\partial t} + \nabla \cdot f(u) = 0 \tag{2.36}$$

Where u represent a vector of states and $f(u)$ is the flux of the vector. Let us consider a finite volume cell i. By taking the volume integral over the volume cell v_i, we obtain:

$$\int_{v_i} \frac{\partial u}{\partial t} dv + \int_{v_i} \nabla \cdot f(u)\, dv = 0 \tag{2.37}$$

The first term represents the definition of volume average, while on the second one we can apply the divergence theorem:

$$v_i \frac{d\overline{u_i}}{dt} + \oint_{S_i} f(u) \cdot n dS = 0 \tag{2.38}$$

Where S_i is cell surface and n is a unit. Now fluxes can be estimated over the edge by extrapolation or interpolation of the cells average. Hence, the time variation of $\overline{u_i}$ only depends on the surfaces fluxes.

If we consider the following figure, by applying the conservation law over the three cells Ω_1, Ω_2, Ω_3 and summing the three surfaces integral, it seems that edge fluxes appear two times. However, for the two adjacent cells BDE and ADE, the fluxes are the same but with opposite signs:

$$(-\int_{ED} \vec{F} \cdot d\vec{S} = \int_{DE} \vec{F} \cdot d\vec{S}) \tag{2.39}$$

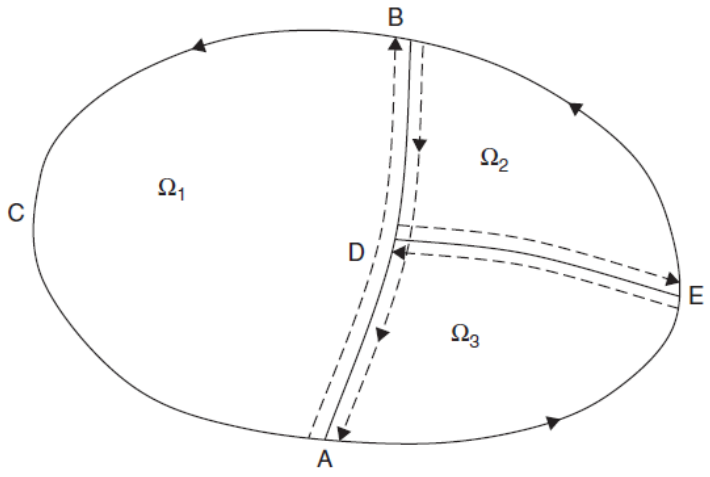

Figure 2.5 - The conservation law can be applied over this volume [16].

When this important property is satisfied, the scheme is said **conservative** [16].

In general, for the FVM two steps are necessary:

I. The mesh volume has to be subdivided into finite volumes and each control volume has to be associated to each grid points.
II. For each control volume the integral conservation law must be applied.

Let us consider a simple case where $f(u) \cdot n = \Gamma \nabla \phi \cdot n$ represents the diffusive component of the flux. Γ represents fluid properties that we assume are known. In order to evaluate the flux,

it is necessary to know the value of the gradient of ϕ for each face of the volume. Flux values have to be evaluated through an interpolation of the nodal values.

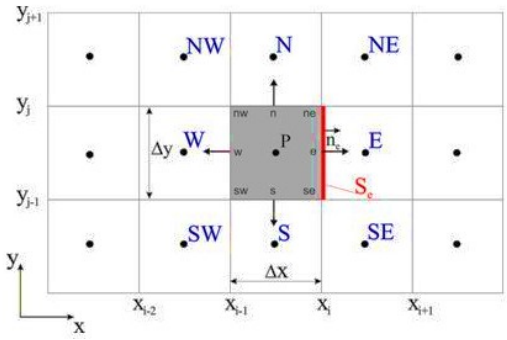

Figure 2.6 – Discretization of a Cartesian 2D grid. The control volume surface consists in 4 faces, identified according to spatial direction (e, w, n, s).

If we only consider the value of ϕ on the east face, ϕ_e, we can approximate it by using a backward- or a forward-difference scheme for the first derivative, as follows:

$$\phi_e = \begin{cases} \phi_P \text{ if } (v \cdot n)_e > 0 \\ \phi_e \text{ if } (v \cdot n)_e < 0 \end{cases} \tag{2.40}$$

This way of interpolating flux values is called **upwind differencing scheme**. We can define ϕ_e through a Taylor expansion. We can note that the UDS retains only the first term, leading to a truncation error proportional to the first derivate. For this reason, the UDS is a first-order scheme which presents a *numerical diffusion*.

At the same way, we can define another interpolation method, the **central differencing scheme**. In this case, ϕ_e is approximated by employing both values ϕ_E and ϕ_P as follows:

$$\phi_e = \phi_E \lambda_e + \phi_P (1 - \lambda_e) \tag{2.41}$$

Where $\lambda_e = (x_e - x_P)/(x_E - x_P)$. This time the method considers the first two terms of the Taylor expansion, leading to a truncation term proportional to the square of the grid interval in the hypothesis that:

$$\left(\frac{\partial \phi}{\partial x}\right)_e = \frac{\phi_E - \phi_P}{x_E - x_P} \tag{2.42}$$

2.2.2.3 Finite element method

The FEM draws a discretization of the space that is conceptually similar to the FVM. The grid is discretized in contiguous cells of arbitrary shapes, called **elements**. However, the FEM is mostly employed in discretization of unstructured grids.

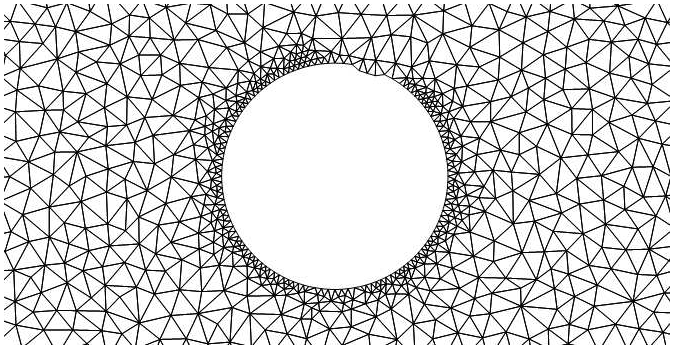

Figure 2.7 - Example of discretization through the FEM.

Once the elements have been defined, the method provides a representation of the unknown variables for each element through some **interpolating functions** (or **trial functions**, or **shape functions**). Let us consider an unknown function $u(\vec{x})$, we can represent it through a linear combination of an interpolating function N_I [16] for each node *I*:

$$\tilde{u}(\vec{x}) = \sum_I u_I N_I(\vec{x}) \tag{2.43}$$

Where, u_I represents the numerical value of the unknowns at node *I*, such that:

$$\tilde{u}(\vec{x}_I) = u_I \tag{2.44}$$

Consequently, $N_I(\vec{x}_I) = \delta_{II}$ is a function that is 1 at the node *I* and 0 in the rest of the grid. The global function N_I can be obtained by adding all the contributions for every element which is connected to the node that we are studying.

The PDE usually employs:

- Algebraic equations for steady state problems.
- Ordinary differential equations for transient cases.

For each nodes of the grid, the total number of unknowns, functions and derivatives represents the **degree of freedom** of the problem.

Finally, an integral formulation is given for the equations previously defined, that have to be solved for each element of the grid.

2.3 POPULATION BALANCE EQUATIONS

Population balance consists of an integro-differential equation which allows to follow particles distribution over time. In a liquid-liquid system, the dispersed phase consists of droplets, which undergo coalescence and breakage. For such systems, we are interested in droplet size distribution (DSD) of the dispersed phase. The DSD allows to determine several dispersion properties. For instance, in a stirred tank reactors DSD depends on the geometry of the tank and from the operating conditions. Indeed, droplets breakage is stronger in the zone near to the impeller, shifting particles towards smaller one. On the other hand, in the stagnant zone far from the impeller, coalescence occurs with a greater probability, leading the DSD to higher diameters [21].

In this study, we are just interested in aggregation and breakage phenomena, thus we used a simplified version of PBE, the general aggregation-breakage equation. The general expression for the PBE, in the case of a 3D system, depends on external coordinates (spatial) *x*, on internal coordinates φ (the properties of the dispersed phase that will be monitored) and on time *t* [34]:

$$\begin{aligned} \frac{\partial n(x,\varphi,t)}{\partial t} + \langle u_i \rangle \frac{\partial n(x,\varphi,t)}{\partial x_i} - \frac{\partial}{\partial x_i}\left[D_t \frac{\partial n(x,\varphi,t)}{\partial x_i}\right] \\ = \frac{\partial}{\partial \varphi_j}\left[n(x,\varphi,t)\dot{\varphi}_j\right] + s(x,\varphi,t) \end{aligned} \tag{2.45}$$

The term $s(x,\varphi,t)$ is defined as **source term** and it depends on the phenomena that we are investigating.

In the equation (2.45), Reynolds-averaged velocities appear. In order to estimate Reynolds-averaged velocities, it is necessary to couple CFD with PBE. However, such operation would require long computation time and for this purpose, a 0D model has been employed. Furthermore,

in this work only particles size has been investigated. Hence, in continuous form and for a homogeneous system and by considering, the equation becomes [17]:

$$\begin{aligned}\frac{\partial n'(v;t)}{\partial t} = &\frac{1}{2}\int_0^v Q(v-\epsilon,\epsilon)n'(v-\epsilon;t)n'(\epsilon;t)d\epsilon \\ &- n'(v;t)\int_0^\infty Q(v,\epsilon)n'(\epsilon;t)d\epsilon \\ &+ \int_v^\infty \Gamma(\epsilon)\beta(v|\epsilon)n'(\epsilon;t)d\epsilon \\ &-\Gamma(v)n'(v;t)\end{aligned} \tag{2.46}$$

where:

- $n'(v;t)$ is the **number density function** (NDF).
- $Q(v)$ is the **aggregation kernel**.
- $\Gamma(v)$ is the **breakage kernel**.
- $\beta(v)$ is the **daughter size distribution function**. It contains information about the number of fragments generated after a drop breakage ($p(v)$) and about their size. In particular, $\beta(v)$ is a distribution function that contains information about the probability for a drop to produce a breakage event. Binary breakage is generally assumed.

All the terms are volume-averaged. The right-hand side terms represent the source term $s(v,t)$. It is composed by four terms:

- The first one considers the formation of a mother-droplet with a volume $v+\epsilon$ generated by the collision of two particles of volume v and ϵ respectively.
- The second term represents the loss of droplets of volume v caused by coalescence.
- The third one describes the number of particles of volume v born out of the breakage of a particle of volume ϵ.
- The last term represents the loss of droplets caused by the breakage.

2.3.1 Volume-averaging procedure

Now, we want to integrate out the special coordinates dependence in the equation (2.46). For this purpose, the volume-averaging procedure can be applied to NDF and to kernels in the source terms (where V is the volume of the stirred reactor), leading to:

$$\bar{n}(v,t) = \frac{1}{V}\int_V n(\boldsymbol{x},v,t)d\boldsymbol{x} \tag{2.47}$$

$$\frac{1}{V}\int_V Q(\boldsymbol{x},v)d\boldsymbol{x} \approx \bar{Q}(v,\varepsilon(\boldsymbol{x})) \tag{2.48}$$

$$\frac{1}{V}\int_V \Gamma(\boldsymbol{x},v)d\boldsymbol{x} \approx \bar{\Gamma}(v,\varepsilon(\boldsymbol{x})) \tag{2.49}$$

Here we note that even if the volume-averaged NDF does not depend on the spatial coordinates, PBEs source terms still depend on them, because of the presence of ε, which in terms strongly depends on the position $\boldsymbol{x}$, inside the geometry under investigation. According to Buffo et al. [21] and Castellano et al. [22] kernels can be approximated with the following expressions:

$$\frac{1}{V}\int_V Q(\boldsymbol{x},v,v')d\boldsymbol{x} \approx \int_0^\infty Q(\varepsilon,v,v')f(\varepsilon)d\varepsilon = \bar{Q}(v,v') \tag{2.50}$$

$$\frac{1}{V}\int_V \Gamma(\boldsymbol{x}, v)d\boldsymbol{x} \approx \int_0^\infty \Gamma(\varepsilon, v)f(\varepsilon)d\varepsilon = \bar{\Gamma}(v) \tag{2.51}$$

Where $f(\varepsilon)$ is the volumetric **probability density function (PDF)** of ε which expresses the volume fraction of the domain having a turbulent kinetic energy dissipation rate value between ε and $\varepsilon + d\varepsilon$. This function can be obtained through **single phase CFD simulation**, if the system is **adequately diluted** [22], as previously mentioned.

In order to make the entire equation completely independent of spatial coordinates, it is necessary to apply the volume-averaging procedure again. Equation (2.46) becomes:

$$\begin{aligned}\frac{\partial \bar{n}(v,t)}{\partial t} = \frac{1}{2}\int_0^v \bar{Q}\big((v-v'),v'\big)\bar{n}(v',t)\bar{n}\big((v-v'),t\big)dv' \\ - \bar{n}(v,t)\int_0^\infty \bar{Q}(v,v')\bar{n}(v,t)dv' \\ + \int_L^\infty \bar{\Gamma}(v')\beta(v,v')\bar{n}(v,t)dv' \\ -\bar{\Gamma}(v)\bar{n}(v,t)\end{aligned} \tag{2.52}$$

This 0D model is also known as *homogeneous model* and it can be employed to have quicker results with a good degree of precision. Compared to a fully coupled CFD – PBM simulation, even if this model is based on the volume-averaging procedure, it is completely different from 0D *uniform* models [21], where a unique voume averaged value of ε in the equation of the volume averaged kernels is used.

2.4 INITIAL MODEL – COULALOGLOU AND TAVLARIDES KERNELS

Aggregation and breakage kernels could be expressed in different ways [18], [19]. In this study, we used the most known formulation for a liquid-liquid dispersion in turbulent conditions, provided by **Coulaloglou and Tavlarides** [5].

2.4.1 Breakage kernel

Surface tension, density and disperse phase hold-up affect drops distribution and the frequency of the breakage phenomenon. Namely, in a turbulent flow, the local turbulent energy dissipation plays a key role. Energy dissipation is usually provided by Kolmogorov's theory, assuming that droplets are in a turbulent flow that is locally isotropic. Even droplet size influences the breakage mechanism. Indeed, droplet breakage is caused by the arrival on the surface of an eddy of equal or lower size than the one of the droplet and with a turbulent kinetic energy higher than the droplet surface energy. In particular, as we saw in section 2.1, eddy energy distribution depends on the size and follows two different behaviours. Coulaloglou and Tavlarides considered uniquely droplets within the inertial subrange ($l_{DI} > d > \eta$), where both the similarity hypothesis are valid. Thus, viscosity is not accounted in the computation of inertial forces.

Generally, the breakage kernel for a droplet of volume v is expressed by:

$$\Gamma(v) = \left(\frac{1}{t_b}\right)\left(\frac{N_{break}(v)}{N_{tot}(v)}\right) \tag{2.53}$$

The ratio $\frac{N_{break}(v)}{N_{tot}(v)}$ represents the fraction of droplets which incurs in breakage. The breakage time t_b is provided by Batchelor [14], who considers the droplets as two lumps of fluid moving in opposite direction. If we consider the distance between the two lamps equal to drop diameter and

the second order structure function derived by considering the -5/3 law, the breakage time is expressed as:

$$t_b = c_1 v^{2/9} \varepsilon^{-1/3} \tag{2.54}$$

The fraction of drops breaking should be assumed proportional to the fraction of eddies colliding with droplets, which cause their breakage. Hence, eddies must have a turbulent kinetic energy greater than the droplet surface energy E_c:

$$E_c = c_2 \sigma v^{2/3} \tag{2.55}$$

where σ is the surface tension.

If we consider the fraction of drops breaking as the velocity distribution of eddies having the energy required E, we obtain:

$$\frac{N_{break}(v)}{N_{tot}(v)} = \exp\left(-\frac{E_c}{E}\right) \tag{2.56}$$

Thus, the mean turbulent energy is:

$$E = c_3 \rho_d d^3 \bar{u}^2(v) \tag{2.57}$$

where ρ_d is the disperse phase density.

Eq. (22), (23) (24)and (25) lead to the following expression for the breakage kernel:

$$\Gamma(v) = K_1 v^{-2/9} \varepsilon^{1/3} \exp\left(-\frac{K_2 \sigma}{\rho_d v^{5/9} \varepsilon^{2/3}}\right) \tag{2.58}$$

K_1 and K_2 are model parameters which have to be obtained by fitting experimental data.

Coulalouglou and Tavlarides eventually included the damping effect due to the dispersed phase fraction ϕ in the calculation of the turbulent energy dissipation ε_d:

$$\varepsilon_d = \varepsilon_c / (1 + \phi)^3 \tag{2.59}$$

2.4.2 Coalescence kernel

Coalescence is caused by the chaotic motion of droplets in a turbulent flow. Indeed, the droplets are transported by eddies that have bigger dimensions than the droplet ones. This chaotic motion could lead to the collision of two droplets. Coalescence takes place if droplets remain in contact for a sufficient time to occur the film drainage, the film rupture and the final coalescence.

Generally, coalescence kernel is the result of two factors:

$$Q(v, v') = h(v, v') \lambda(v, v') \tag{2.60}$$

where $h(v, v')$ is the collision rate of drops and $\lambda(v, v')$ is the coalescence efficiency of binary collisions.

The mechanism of collision between droplets could be considered analogous to the one of particles collision in kinetic theory of gases. For two droplets having volumes v and v' and mean square velocities $\bar{u}^2(v)$ and $\bar{u}'^2(v)$, respectively, the first factor is expressed as:

$$h(v, v') = c_4 \left(v^{\frac{2}{3}} + v'^{\frac{2}{3}}\right) [\bar{u}^2(v) + \bar{u}'^2(v)] \tag{2.61}$$

For the expression of the second term we should consider that the film drainage, the film rupture and the final coalescence must occur in a *coalescence time* τ. If drops rest in contact for a time t greater than τ, the coalescence will take place. By assuming that contact time is randomly distributed, coalescence efficiency could be expressed as:

$$\lambda(v, v') = \exp(-\tau/t) \tag{2.62}$$

The coalescence time τ could be obtained by considering the film drainage model [4] and the compressing forces, taken proportional to second order structure function provided by Kolmogorov for the inertial subrange. Thus, we obtain a final expression for the coalescence efficiency:

$$\lambda(v, v') = \exp\left[-\frac{c_5 \mu_c \rho_c \varepsilon}{\sigma^2}\left(\frac{v^{1/3} v'^{1/3}}{v^{1/3} + v'^{1/3}}\right)\right] \tag{2.63}$$

where μ_c and ρ_c are respectively the viscosity and the density for the continuous phase. Here, the contact time is assumed proportional to the characteristic period of velocity fluctuation of an eddy of volume $v + v'$, defined as:

$$t = \frac{\left(v^{1/3} + v'^{1/3}\right)^{2/3}}{\varepsilon^{1/3}} \tag{2.64}$$

In the end, by including the inertial subrange second order structure function, for equal volume size droplets, we obtain the final expression for the coalescence kernel:

$$Q(v, v') = K_3 \left(v^{\frac{2}{3}} + v'^{\frac{2}{3}}\right)\left(v^{\frac{2}{9}} + v'^{\frac{2}{9}}\right)\varepsilon^{1/3} \exp\left[-\frac{K_4 \mu_c \rho_c \varepsilon}{\sigma^2}\left(\frac{v^{1/3} v'^{1/3}}{v^{1/3} + v'^{1/3}}\right)\right] \tag{2.65}$$

K_3 and K_4 are parameters which have been obtained by fitting experimental data.

2.4.3 Daughter size distribution

As we saw in the general equation for a population balance, it is necessary to specify a breakage frequency, which is the result of two terms: $p(v')$ and $\beta(v|v')$.

The first term is the number of daughter drops created after a breakage event. A binary breakup was considered during this work. The second term is the daughter size distribution, representing the probability for a mother drop of volume v to break in two daughter droplets of volume vf_w and $v(1 - f_w)$, respectively (f_w is the volume fraction). In order to ensure mass balance, the following relations must be satisfied:

$$\begin{aligned} \int_0^\infty \beta(v|v')\, dv' &= p(v) \\ \int_0^\infty v'\beta(v|v')\, dv' &= v \end{aligned} \tag{2.66}$$

In literature, we can find several breakage frequency models. The simplest one, adopted by Coulaloglou and Tavlarides, considers a Gaussian distribution for the daughter droplets. Thus, the highest probability corresponds to the formation of two equal-sized drops. However, there are no real evidences in the experimental data collected. Indeed, other models have been proposed. Among them, a U-shaped distribution considers the breakage of a "mother" drop in two unequal-sized drops could be observed, a main one and a satellite one.

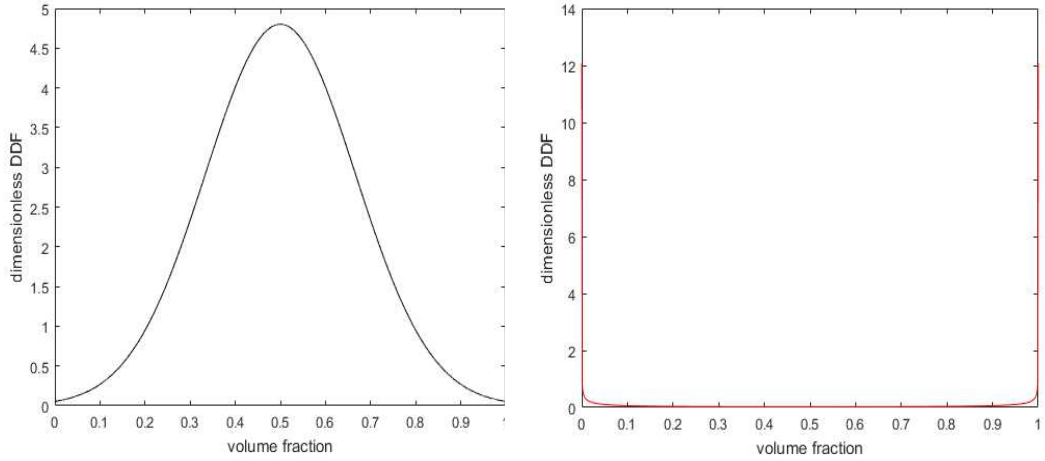

Figure 2.8 - Daughter size distributions. On the left a Gaussian distribution, on the right a U-shaped distribution.

2.5 ADVANCED MODEL – ACCOUNTING FOR DISSIPATION ENERGY OVERESTIMATION

2.5.1 Pope's energy spectrum

Since the Kolmogorov spectrum is valid only for the inertial subrange, as we saw in the paragraph 2.1.4, we are interested in finding an expression which is more generally.
For this purpose, according to Pope's definition [13] the energy spectrum can be expressed as follows:

$$E(\kappa) = C\varepsilon^{\frac{2}{3}}\kappa^{-\frac{5}{3}}\left(\frac{\kappa L}{[(\kappa L)^2 + c_L]^{\frac{1}{2}}}\right)^{\frac{11}{3}} exp(-\beta\{[(\kappa\eta)^4 + c_\eta^4]^{\frac{1}{4}} - c_\eta\}) \tag{2.67}$$

Where

- κ is the wavelength of the eddies spectrum.
- The second term, $f_L(\kappa L)$, is a non-dimensional function which determines the shape of the energy-containing range. L denotes the integral length-scale, representing the characteristic dimension of the system. In this work, L has been replaced by the impeller diameter.
- The exponential term, $f_\eta(\kappa\eta)$, is also a non-dimensional function which represents the shape of the dissipation range. The constant β (=5,2) is provided by experimental data [23]. η is the Kolmogrov scale.
- c_L and c_η are coefficients that can be obtained by solving the following equations:

$$\begin{cases} \varepsilon - \int_0^\infty 2\upsilon k^2 E(k, c_L, c_\eta)dk = 0 \\ k - \int_0^\infty E(k, c_L, c_\eta)dk = 0 \end{cases} \tag{2.68}$$

By using this new formulation, we are considering all the contributions given by the energy-containing, the inertial and the dissipation ranges, in contrast with the Kolmogorov' energy spectrum, which overestimated the global dissipated energy.

2.5.2 Second order structure function

As we saw in the paragraph 2.1.3, the relative velocity between two points in a turbulent isotropic flow can be expressed as follows:

$$\langle[\Delta u(r)]^2\rangle = \langle[u_x(x+r) - u_x(x)]^2\rangle \tag{2.69}$$

By considering the assumption of turbulence isotropy it is possible to show that the function could be simplified as follows [24]:

$$\langle[\Delta u(r)]^2\rangle \sim \frac{4}{3}\,\langle\frac{1}{2}u^2\rangle \tag{2.70}$$

We note that the term $\langle\frac{1}{2}u^2\rangle$ physically corresponds to [24]:

$$\begin{aligned}\langle[\Delta u(r)]^2\rangle \sim & \frac{4}{3}[all\ energy\ in\ eddies\ of\ size \leq r] \\ & + r^2[all\ enstrophy\ n\ eddies\ of\ size \geq r]\end{aligned} \tag{2.71}$$

Now, by replacing the eddy size r with the wavenumber κ and by applying the Fourier transform, we can define the energy spectrum $E(\kappa)$. Namely, it can be used to define $\langle[\Delta u(r)]^2\rangle$ when $r \to 0$.

$$\langle[\Delta u(r)]^2\rangle \sim \int_0^\infty E(\kappa)d\kappa \tag{2.72}$$

This term is useful to evaluate the energy distribution across eddy sizes from 0 to ∞.
At the same way, $E(\kappa)$ could be used to give a definition of enstrophy $\mathcal{E}$, which can be interpreted as the quantity of energy directly related to the vorticity ω of the flow, causing dissipation effects.

$$\mathcal{E}(\omega) = \frac{1}{2}\langle\omega^2\rangle = \int_0^\infty \kappa^2 E(\kappa)d\kappa \tag{2.73}$$

We can eventually define a new function $H(\kappa r)$, which allows to simplify the relation between $\langle[\Delta u(r)]^2\rangle$ and $E(\kappa)$ as follows [24]:

$$\langle[\Delta u(r)]^2\rangle \approx \frac{4}{3}\int_0^\infty E(\kappa)\left\{1 - 3\left[\frac{sin(\kappa r)}{(\kappa r)^3} - \frac{cos(\kappa r)}{(\kappa r)^2}\right]\right\}d\kappa \tag{2.74}$$

Where, $H(\kappa r) = 1 - 3\left[\frac{sin(\kappa r)}{(\kappa r)^3} - \frac{cos(\kappa r)}{(\kappa r)^2}\right]$, and it can be approximated as:

$$H(\kappa r) \approx \begin{cases}(x/\pi)^2, & for\ x < \pi \\ 1, & for\ x > \pi\end{cases}$$

Finally, by using the linearity of integration property, we are able to find a final expression, where on the right side we identify, respectively in the first and in the second term, the eddies energy for small eddies and the enstrophy for eddies which the size is r or greater.

$$\langle[\Delta u(r)]^2\rangle \approx \frac{4}{3}\int_{\pi/r}^\infty E(\kappa)d\kappa + \frac{4r^2}{3\pi^2}\int_0^{\pi/r} \kappa^2 E(\kappa)d\kappa \tag{2.75}$$

2.5.3 Coulaloglou and Tavlarides' kernels reformulation

At this stage it is necessary to rewrite the kernels previously proposed, as functions of mean square velocity $\bar{u}(r)^2$.

2.5.3.1 Breakage kernel

As we saw in the paragraph 2.4.1, we need to define a breakage time t_b. On the basis of Coulaloglou and Tavlarides' definition, the breakage time can be expressed as follows:

$$t_b = \frac{c_1 v^{\frac{1}{3}}}{\sqrt{\bar{u}(v)^2}} \tag{2.76}$$

For the surface energy E_c and the droplets kinetic energy E we can employ the expressions previously introduced. Hence, the breakage kernel assumes the following final formulation:

$$\Gamma(v) = K_1\sqrt{\bar{u}(v)^2}v^{-1/3}\exp\left(-\frac{K_2\sigma}{\rho_d v^{1/3}\bar{u}(v)^2}\right) \tag{2.77}$$

K_1 and K_2 are parameters which have been obtained by fitting experimental data.

2.5.3.2 Coalescence kernel

As in the previous expression, we can adopt the same function $h(v, v')$ and the same coalescence time τ, depending on the drainage film theory. Nevertheless, it is necessary to change the real contact time t according to Levich definition [38].

$$t = \frac{v^{-1/3} + v'^{-1/3}}{\sqrt{\bar{u}(v, v')^2}} \tag{2.78}$$

Finally, the coalescence kernel becomes:

$$Q(v, v') = K_3\left(v^{\frac{2}{3}} + v'^{\frac{2}{3}}\right)(\bar{u}(v)^2 + \bar{u}(v')^2)^{1/2} \exp\left[-\frac{K_4\mu_c\rho_c}{\sigma^2}\frac{\left(v^{1/3}v'^{1/3}\right)^4}{(v^{1/3} + v'^{1/3})^5}[\bar{u}(v + v')^2]^{3/2}\right] \tag{2.79}$$

K_3 and K_4 are parameters which have been obtained by fitting experimental data.

2.6 SOLUTION METHODS FOR THE POPULATION BALANCE EQUATION

Population balance equations rarely have analytical solutions. For this reason, numerical methods are often employed for solving PBEs. In this study, we mention just two of them:

- The **Fixed Pivot Method (FPM)**, which is one of the numerous discretization methods. Such methods are based on the discretization of a continuous function (or variable) in order to obtain a set of equations that can be solved in each discretized size-interval.
- The **Methods of Moments**, which allows to solve a population balance equation in terms of sample moments for a specified parameter. When moment methods are available, they have the advantage of being simple to apply. The disadvantage is that they are often not available.

2.6.1 The Fixed Pivot Method

This method has been developed by Kumar and Ramkrishna [20]. The advantage of this method is its consistence with the two random moments. For convenience, it is usually ensured the conservation of the total number of droplets and their mass (or volume). Furthermore, the method allows to implement any kind of grids, such as geometric or arithmetic. For this reason, the FPM has been used in this work.

The FPM starts by discretizing the droplet volume v into N intervals $[v_i; v_{i+1}]$. The method assumes that all the drops, whose dimension is included in the interval $[v_i; v_{i+1}]$, are centered at the pivot of the interval x_i, defined as $v_i < x_i < v_{i+1}$. Hence, all the droplets in an interval have the volume equal to the one of the interval pivots. Based on this assumption, Kumar and Ramkrishna expressed the number density function as follows:

$$n(v,t) = \sum_{i=1}^{M} N_i(t)\delta(v - x_i) \tag{2.80}$$

Then, the authors integrated the PBE with respect to the variable v in each interval $[v_i; v_{i+1}]$, obtaining the following formulation:

$$\begin{aligned}\int_{v_i}^{v_{i+1}} \frac{\partial n(t)}{\partial t} dv = \\ = \frac{1}{2}\int_{v_i}^{v_{i+1}} \left(\int_0^v Q(v-v',v')n(v',t)n(v-v')dv'\right)dv \\ - \int_{v_i}^{v_{i+1}} n(v,t)\left(\int_0^{\infty} n(v',t)Q(v,v')dv'\right)dv \\ + \int_{v_i}^{v_{i+1}} \left(\int_v^{\infty} \Gamma(v')(\beta(v,v')n(v',t)dv'\right)dv \\ - \int_{v_i}^{v_{i+1}} \Gamma(v)n(v,t)dv\end{aligned} \tag{2.81}$$

This method allows to write the number density function as follows:

$$n(v,t) = \sum_{i=1}^{M} N_i(t)\delta(v - x_i) \tag{2.82}$$

According to Eq. (36), the terms of the PBE become as follows:

1) **Accumulation**:

$$\int_{v_i}^{v_{i+1}} \frac{\partial n(t)}{\partial t} dv = \frac{\partial N(i)(t)}{\partial t} \tag{2.83}$$

2) **Birth due to breakage**:

$$\begin{aligned}R_{Bb} = \int_{v_i}^{v_{i+1}} \left(\int_v^{\infty} \beta(v,v')n(v',t)\Gamma(v')dv'\right) = \\ = \int_{x_i}^{x_{i+1}} a(v,x_i)\left(\int_v^{\infty} \beta(v,v')n(v',t)\Gamma(v')dv'\right)dv \\ + \int_{x_{i-1}}^{x_i} b(v,x_i)\left(\int_v^{\infty} \beta(v,v')n(v',t)\Gamma(v')dv'\right)dv\end{aligned} \tag{2.84}$$

Finally we obtain:

$$R_{Bb} = \sum_{x_i}^{x_{i+1}} n_{i,k}\,\Gamma_k N_k(t) \tag{2.85}$$

Where,

$$n_{i,k} = \int_{x_i}^{x_{i+1}} \frac{x_{i+1} - v}{x_{i+1} - x_i}\beta(v,x_k)dv + \int_{x_{i-1}}^{x_i} \frac{v - x_{i-1}}{x_i - x_{i-1}}\beta(v,x_k)dv \tag{2.86}$$

3) **Death due to breakage**:

$$R_{Db} = \Gamma_i N_i(t) \tag{2.87}$$

4) **Birth due to coalescence**:

$$R_{Ab} = \sum_{\substack{j,k \\ x_{i-1} \le (x_j + x_k) \le x_{i+1}}}^{j \ge k} \left(1 - \frac{1}{2}\delta_{j,k}\right) \eta \, Q_{j,k} N_j(t) N_k(t) \tag{2.88}$$

Where,

$$\eta = \begin{cases} \dfrac{x_{i+1} - v}{x_{i+1} - x_i} & x_i \le v \le x_{i+1} \\ \dfrac{v - x_{i-1}}{x_i - x_{i-1}} & x_{i-1} \le v \le x_i \end{cases}$$

5) **Death due to coalescence**:

$$R_{Da} = N_i(t) \sum_{k=1}^{M} Q_{i,k} N_k(t) \tag{2.89}$$

Finally:

$$\begin{aligned} \frac{dN_i(t)}{dt} = & \sum_{\substack{j,k \\ x_{i-1} \le (x_j + x_k) \le x_{i+1}}}^{j \ge k} \left(1 - \frac{1}{2}\delta_{j,k}\right) \eta \, Q_{j,k} N_j(t) N_k(t) - \Gamma_i N_i(t) \\ & - N_i(t) \sum_{k=1}^{M} Q_{i,k} N_k(t) + \sum_{x_i}^{x_{i+1}} n_{i,k} \, \Gamma_k N_k(t) \end{aligned} \tag{2.90}$$

2.6.2 The Quadrature Method of Moments (QMOM)

For solving an integro-differntial equation, is mandatory to consider the computational time spent by the calculator. For instance, Monte Carlo and Fixed Pivot methods are usually more computationally expensive. For this reason, a good compromise can be the use of the Method of Moments (MOM). However, this method seems to be inaccurate for different cases. A valid alternative is the **Quadrature Method of Moments (QMOM)**, although it is not easy to extend to multivariate system. Furthermore, this method is only based on the particles size distribution moments, which does not allow to directly obtain the NDF. Nevertheless, they can be considered a reliable method to evaluate the moments of the distributions.

Proposed by McGraw, it was extended and tested successfully to PBEs by Marchisio et al. et al. [17]. Hence, it is first necessary to introduce the definition of a k-order moment for the case of the NDF $n(L;t)$ (L is the particle diameter):

$$m_k(t) = \int_0^{+\infty} n(L;t) \, L^k dL \tag{2.91}$$

In particular, here a quadrature approximation could be employed:

$$m_k(t) \approx \sum_{i=1}^{N} w_i L_i^k \tag{2.92}$$

Where w_i are the weights, L_i are the abscissas and both of them are determined by using the product-difference (PD) algorithm, proposed by Gordon in 1968. The PD algorithm is based on the minimization of the error for the estimation of the moment integral [35].

One of the advantages of this method is that the weights w_i and the abscissas L_i can be specified from the lower-order *i* moments. For this reason, to build a k-order quadrature approximation, it is sufficient to know the first *2k* moments. Thus, if the QMOM is applied on three nodes, it can accurately describe the first six moments $(m_0, \dots, m_5)$ [34].

By applying the QMOM on the PBE, we obtain:

$$\frac{\partial m_k(t)}{\partial t} = \frac{1}{2}\sum_i w_i \sum_j w_j (L_i^3 + L_j^3)^{k/3} \beta_{i,j} - \sum_i w_i L_i^k \sum_j w_j \beta_{i,j} + \sum_i w_i a_i b_i^k - \sum_i w_i a_i L_i^k \tag{2.93}$$

Where $\beta_{i,j} = \beta(L_i, L_j)$ is the coalescence kernel, $a_i = a(L_i)$ is the breakage kernel and $b_i = \int_0^\infty b(L_i) L_i^k dL$ represents the daughter size distribution.

2.6.3 Sauter mean diameter

Once the moments have been obtained, the most common way to represents DSD consists of using the Sauter mean diameter d_{32}. It can be defined as the ratio between the third moment and the second moment.

$$d_{32} = \frac{m_3}{m_2} \tag{2.94}$$

2.7 ACCOUNTING FOR INHOMOGENEOUS TURBULENCE DISSIPATION RATE

In order to solve PBEs it is necessary to estimate breakage and coalescence frequencies. As we saw, in literature there are several models depending on fluids properties, such as surface tension, density, viscosity and flow regime parameters, in particular the turbulent kinetic energy dissipation rate ε. Generally, according to the fully turbulence assumption, many authors assume turbulence to be uniform in liquid-liquid contactors and employ a uniform value of ε. However, this assumption can be inadequate to estimate the real breakage and coalescence rates [21], [22]. By using CFD simulations, large variations of ε can be observed in a given liquid-liquid contactor, with zones where the dissipation is elevated and others where it is very low. The figure 2.9 shows the ε distribution provided by a Mixel TT impeller in the case of a stirred tank reactor. It is noticeable that ε is not uniform especially near the impeller and at the walls, where its value is higher compared to every where else.

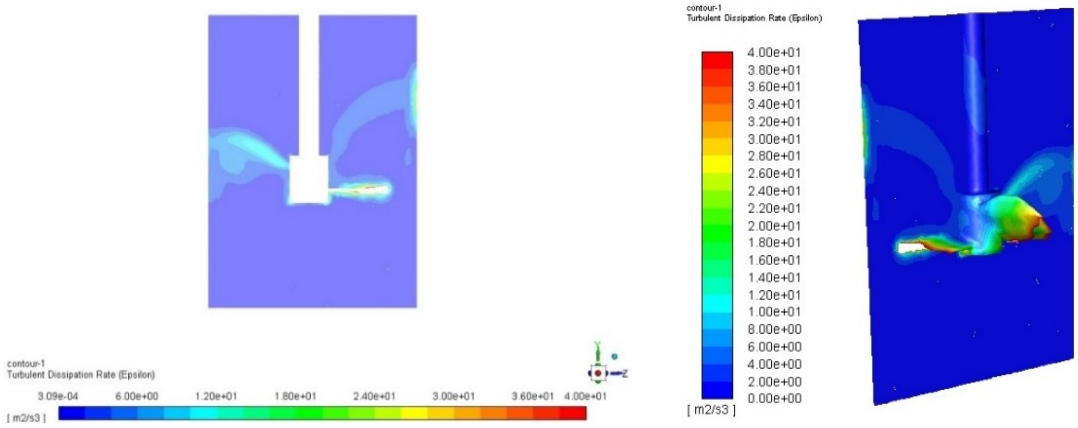

Figure 2.9 - ANSYS Fluent simulations show that the turbulent dissipation rate is not uniform in the space, especially approaching the impeller and the baffles.

In order to account for this inhomogeneity, it is possible to couple CFD simulations with PBEs [21][22]. This strategy can give more reliable results. Neverthless, the main issue remains the computation time. Several methods have been proposed and discussed to solve this problem.

2.7.1 Compartment method

Compartmental methods are a valid alternative to save on computational time in the study of reactor modeling, allowing to retain the effect of fluid dynamics inhomogeneity. In a compartmental model, the computational domain is split into compartments bigger than in simple CFD simulations. The compartments are considered as subdomains having similar flow motion characteristics. In particular, in each compartment ε is considered to be uniform and thus PBEs can be easily solved [36].

The simplest possible configuration of a stirred reactor consists of two compartments: a small region around the impeller with ε values extremely high, and a larger region far from the impeller, where ε is almost 0 [37].

Although this method allows to reduce calculation time, its difficulty is related to the estimation of the fluxes between the compartments. Indeed, for more complex configurations it is necessary a greater number of subdomains, which increase the compartment flux issue.

3 MATERIAL AND METHODS

This study aims to examine the evolution of the droplet size distribution in a liquid-liquid dispersion in a stirred tank reactor. Two different models were developed in order to predict droplets patterns. Several tests were conducted by employing a set of solvents which presents different properties. In particular, in order to approach the PUREX process conditions, viscosities were increased and interfacial tensions were reduced. For this purpose, the Isane, mixture of hydrocarbon chains with 12 to 14 carbon atoms, was firstly mixed with a more viscous compound, the Marcol, and then with the Tributyl phosphate (TBP), which lower the surface tension. Hence, tests were conducted using the organic phase as continuous phase, while water represents the dispersed phase.

3.1 SOLVENTS PREPARATION

In order to approach to PUREX process conditions, the Isane, the Marcol and the TBP were employed in different proportions. The solvents are briefly described hereafter.

- **Isane IP175**: odorless and colorless, Isane is essentially an isoparaffinic solvent, designed for the compositions of resins and paints, for the polyolefin synthesis, for hand soaps and domestic products and other chemical purposes.
- **TBP**: (Tri-n-butyl phosphate) TBP is an industrial chemical compound used for various purposes. It can be employed as plasticizer, as solvent in hydraulic fluid, or a heat exchange agent. It is an odorless colorless to yellow liquid, and it is toxic by ingestion and inhalation.
- **Marcol**: this compound is obtained from petroleum through several refining stages and it consists of a purified mixture of liquid saturated hydrocarbons. Marcol is essentially odorless, tasteless, colorless and transparent. It can be used in food-contact, cosmetic and pharmaceutical applications.

For each solution, the surface tension, the density and the viscosity were measured. The following table resumes the results for each compound:

Table 3.1 - Solvents composition and main properties.

Marcol [%]	Isane [%]	TBP [%]	μ [cP]	ρ [Kg/m^3]	Δσ [mN/m]
0	100	0	1,219	757,4	38,30
100	0	0	12,00	829,7	40,30
0	0	100	3,390	978,0	7,400
45	55	0	4,102	799,9	39,81
30	70	0	2,429	783,4	38,21
0	70	30	1,608	821,4	10,50
30	40	30	3,384	848,2	15,90

The use of a lower tension surface solvent allowed to reduce droplets diameter, providing an easier discrimination of air bubbles, trapped in the solution when viscosity was increased.

3.2 STIRRED TANK REACTOR

Droplets size distribution and its evolution over time was studied performing several laboratory tests. The experimental set up consists of a **1-liter stirred-tank reactor**, figures 3.1 and 3.2, provided with a **3-blades Mixel-TT turbine** and **4 baffles** to avoid vortex formation.

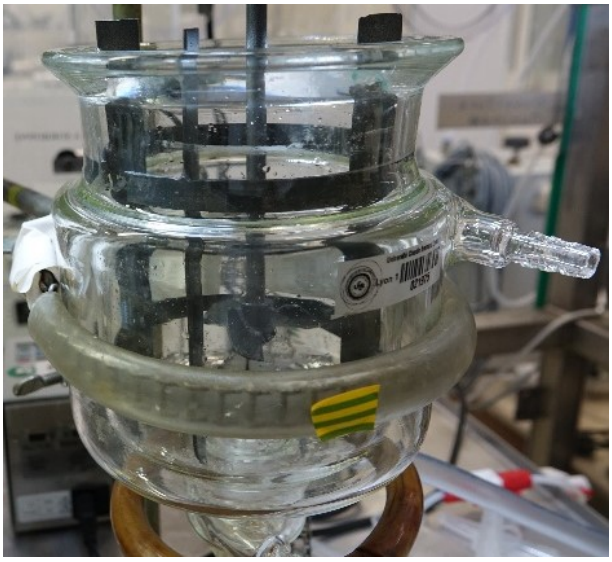

Figure 3.1 - The stirred tank reactor employed for the experiences.

In the following diagram, geometry characteristics of the reactor are illustrated:

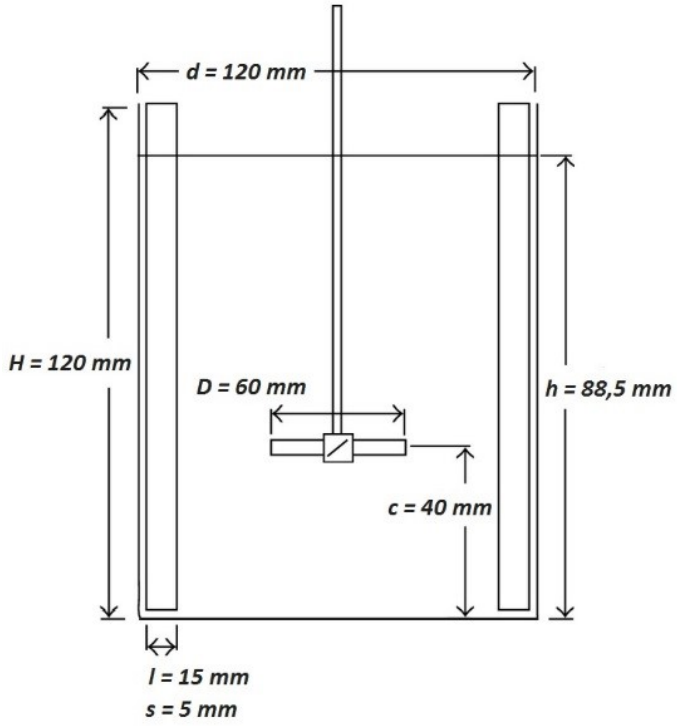

Figure 3.2 - Geometric characteristics of the experimental devices: H is height of tank, d is the diameter of the tank, D is the diameter of the impeller and l and s are respectively the width and the thickness of the baffles.

Since all the experiences were conducted by imposing the organic phase as continuous phase, the walls of the reactor were silanized, while the impeller, the shaft and the baffles were teflon-coated in order to avoid water film formation.

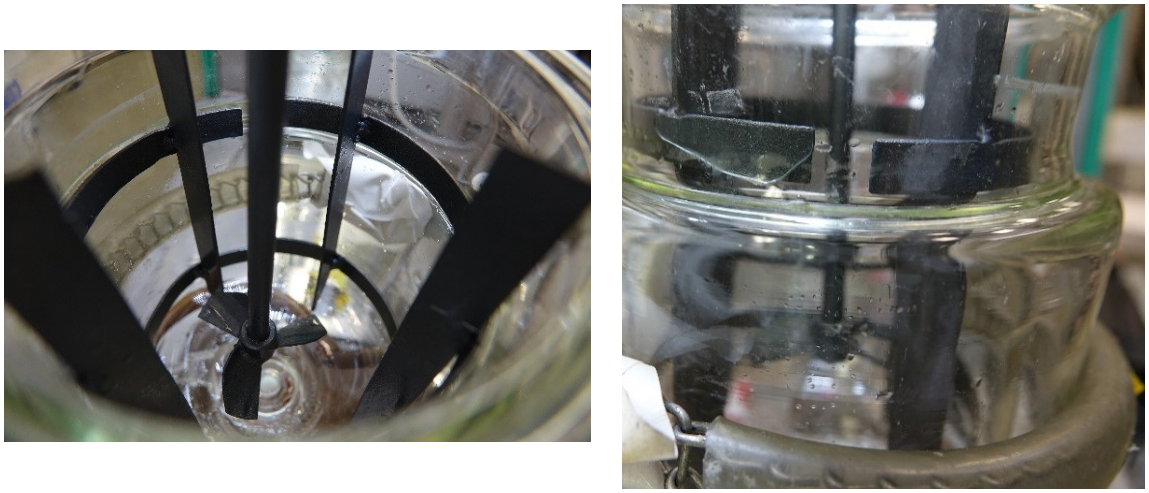

Figure 3.3 - On the left, the teflon-coated impeller and baffles. On the right a global view of the silanized reactor.

In a stirred tank reactor, the Reynolds number can be evaluated as [3]:

$$Re = \frac{\rho N D^2}{\mu} \tag{3.1}$$

Where, N is the rotational speed in rps, D is the impeller characteristc dimension (6 cm), ρ and μ are respectively the density and the viscosity of the continuous phase.

The average turbulent dissipation rate in the reactor was estimated using the following expression [3]:

$$\bar{\varepsilon} = \frac{N_p\, N^3 D^5}{V_r} \tag{3.2}$$

Where, N is the rotational speed in rps, V_r is the liquid volume and N_p is the power number, which is equal to 0,81 for a Mixel TT impeller in a reactor with specified geometry. Three different rotational speeds 600, 700 and 800 rpm were imposed through rotor power regulation. The equation (3.2) shows that ε does not depend on solvent properties. In the following table are indicated the 3 values for ε:

Table 3.2 - ε values depending on rotational speed

Rotation speed (rpm)	ε (m^2/s^3)
600	0,63
700	1,01
800	1,47

3.3 ENDOSCOPIC PROBE

The reactor was equipped with an endoscopic probe SOPAT. The probe has allowed the monitoring of the droplets population through the acquisition of several images. With the probe an image processing software was also provided, which has finally permitted to evaluate the droplets distribution and to obtain the data necessary to validate the model.

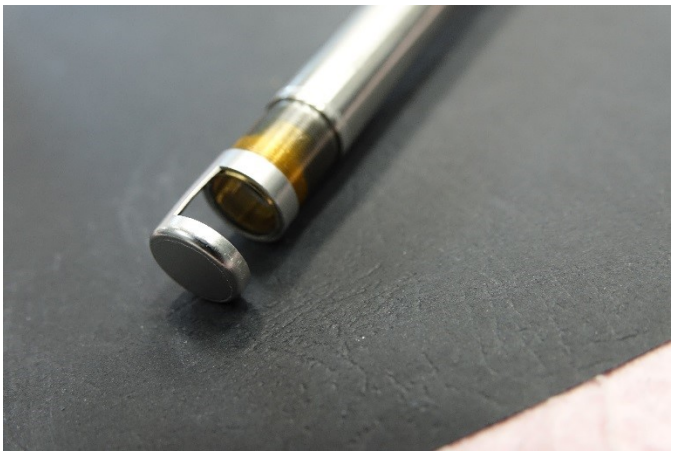

Figure 3.4 - The camera system of the endoscopic probe employed.

During the experiences, the probe was immerged in the agitated dispersion, capturing several frames per minute. The camera strobe flash frame rate was set up at 5 – 7 Hz. Each acquisition is characterized by several triggers. A trigger initiates the capture of frames by analyzing the sensor and eventually send them to a host computer in order to be processed. In the experimental phase, trigger duration was set to 6 seconds and for each acquisition 10 triggers were executed. The number of frames processed for each trigger depends on the dispersion conditions. Indeed, for more viscous solvents a huge part of air was trapped in the stirred reactor, causing a problematic image processing. For this reason, a higher number of frames was necessary. Hence, the total number of frames per camera varies between 190 and 240 frames par minutes.

3.4 MATLAB CODES

PBEs were solved by using the Fixed Pivot Method implemented in a MATLAB routine. This code allowed the evaluation of the Sauter diameter evolution over time, comparing the experimental data with the developed models. In particular, for the *Advanced model* the second order structure function has been evaluated with a second code which constituted an issue for the global computational time. Indeed, the required time was evaluating between 20-25 minutes.

Hereunder, we briefly explain main functions of the developed codes:

I. **Optimization code**: this code allows to estimate kernels parameters K_1, K_2, K_3 and K_4, by fitting experimental data with the two versions of the model. The code employs the function ***patternsearch***, which was used to minimize the residual sum of squares as a function of the parameters. Residual was calculated as difference between experimental Sauter diameters and model Sauter diameters, computed on the basis of initial random parameters.

$$\sum_{i=0}^{4}\left(d_{32,i}^{exp}-d_{32,i}^{comp}\right)^2 \tag{3.3}$$

In particular, by creating an initial random vector x_0, containing the parameters, we are setting the initial points for the pattern search algorithm. Experimental data were taken from two different tests, according to the model computing the diameters:

- **Uniform ε** : 1-2% Isane in Water, computed by Castellano et al. [22].
- **Initial model** : 1-2% Isane in Water, computed by Castellano et al. [22].
- **Advanced model** : 1-2% Water in Isane.

For each experience, four Sauter diameters have been taken at four different times. The definitive parameters which minimize the residual sum of squares are contained in table 3.3.

II. **Second order structure function code**: this code allows to solve the equations (2.67) (2.68) (2.74) which eventually leads to the construction of a matrix containing $\bar{u}(d)^2$ for each diameter class. The MATLAB functions employed are ***integral***, which numerically integrates the equation (2.74), and ***fsolve***, which allows to solve the nonlinear-system (2.68). In the following graph, the difference between the two approaches, Kolmogorov and Pope's energy spectra, are highlighted:

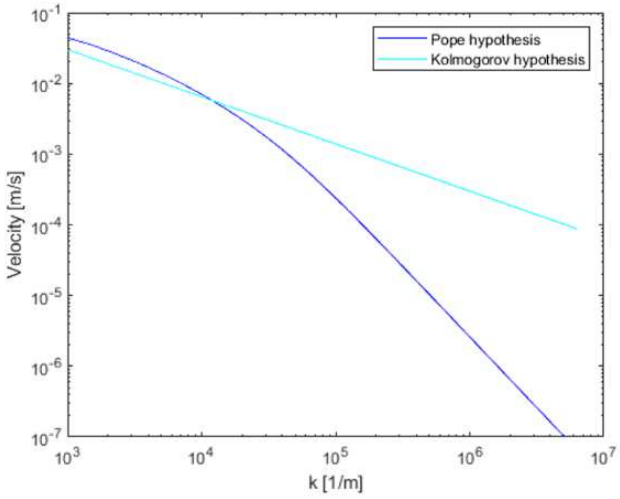

Figure 3.5 - Kolmogorov and Pope's hypothesis concerning energy spectrum have been compared. When κ increases, the two approaches show a spread of about three orders of magnitude. Hence, we find the largest gap between eddies velocity, for very small diameters, exactly in the Dissipation range.

III. **PBEs solving code:** this first code was employed for solving integro-differential equations of a balance population after that FPM was applied. PBEs have been solved by using the MATLAB function ***ode15s***: this function integrates the system of differential equations (e.g. $y' = f(y,t)$) over time, from an initial time t_0 to a final time t_f, by imposing the initial conditions y_0. In particular, this function allows to evaluate for each class of the FPM how particles number evolving over time. Once particles number have been computed, the code calculates the moments and then the Sauter diameters. Besides, the code computes a solution for PBEs by employing the two versions of the model, by eventually comparing the results with the experimental data in the form of graphs d_{32} *vs time*.

3.5 ANSYS FLUENT SIMULATIONS

In order to obtain the volumetric probability density function of ε for the homogenous model, for each experience a parallel CFD simulation was carried out, by using ANSYS Fluent. During the simulations several hypotheses were assumed:

- Since water phase fraction is less than 0,2 (**moderately concentrated system**), **single-phase simulations** were performed.
- Fluid properties were set according to table 2.1, testing the three rotational speeds 600 – 700 – 800 rpm.
- Turbulence was modeled by employing the **standard k-ε** method.
- The impeller motion was modeled by using the **multiple reference frame (MRF)** method. In this method a non-inertial frame reference is considered, according to which the impeller is considered still. The continuity and momentum equations are therefore modified including addictive speed and acceleration terms. This is the simplest approach to model stirred-reactors. More difficult approaches could be used to simulate impeller

motion, as the Sliding Mesh technique. This method considers the mesh deforming continuously due to impeller rotation. [25].

- Concerning solution methods, for pressure, momentum, turbulent kinetic energy k and turbulent dissipation rate ε evaluations the **Second Order Upwind** models were employed. Furthermore, **transient simulations** were used to reach the convergence criteria, by adopting a Second Order Implicit formulation.
- The time step was set to 0,0002 s, which corresponds to the time necessary to the impeller to complete an angle of 1 degree at 600 rpm. This hypothesis is validated in literature [39], [40]. Simulations have been run for almost 1800 time-steps, corresponding to 5 or 6 impeller revolutions.

Concerning the mesh, an unstructured one has been proposed and implemented by employing the software ANSYS meshing. The interior of the reactor has been discretized through tetrahedral cells, while boundary surfaces have been discretized as triangles. The total number of cells is about 712 000, while the triangular faces are about 1 445 000.

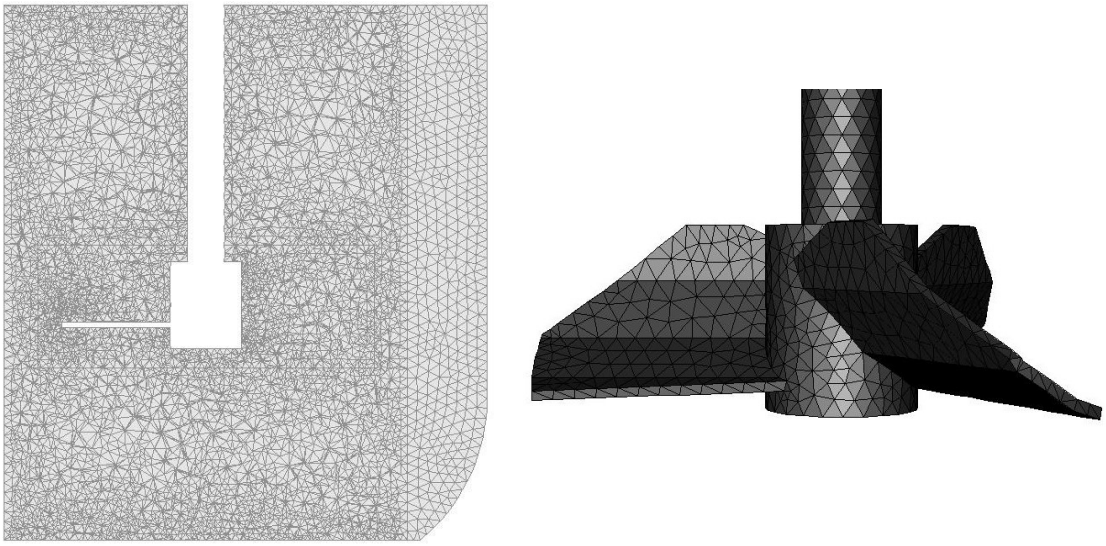

Figure 3.6 - An unstructured mesh has been employed during CFD simulations. On the right, the meshed impeller.

By using ANSYS Fluent some mesh quality parameters can be extracted, such as the minimum orthogonal quality (0,25) and the maximum orthogonal skewness (0,7158). According to the ***ANSYS Fluent Meshing User's Guide***, these two parameters are defined as follows [41]:

- *"**Orthogonal quality** is computed for cells using the vector from the cell centroid to each of its faces, the corresponding face area vector, and the vector from the cell centroid to the centroids of each of the adjacent cells. The worst cells will have an orthogonal quality closer to 0, with the best cells closer to 1. The minimum orthogonal quality for all types of cells should be more than 0.01, with an average value that is significantly higher."*
- *"**Skewness** is defined as the difference between the shape of the cell and the shape of an equilateral cell of equivalent volume. Highly skewed cells can decrease accuracy and destabilize the solution. A general rule is that the maximum skewness for a triangular/tetrahedral mesh in most flows should be kept below 0.95, with an average value that is significantly lower."*

Hence, according to ANSYS directives (Fig. 3.7), the mesh quality can be considered of a **good quality**.

Skewness mesh metrics spectrum:

Excellent	Very good	Good	Acceptable	Bad	Unacceptable
0-0.25	0.25-0.50	0.50-0.80	0.80-0.94	0.95-0.97	0.98-1.00

Orthogonal Quality mesh metrics spectrum:

Unacceptable	Bad	Acceptable	Good	Very good	Excellent
0-0.001	0.001-0.14	0.15-0.20	0.20-0.69	0.70-0.95	0.95-1.00

Figure 3.7 - Mesh quality parameters spectra

An example of PDF of ε is proposed hereunder. PDF is on the y-axis and ε is on the x-axis. It is interesting to note that PDF varies with the rotation speed. Higher values of rotational speed imply higher value of energy transmitted from the rotor to the system, which is eventually dissipated by the system. This energy contributes to increase ε. Furthermore, we note that even if the PDF values are very low, the system may assume very high values (40 – 50 m^2/s^3), by describing a decreasing tendency.

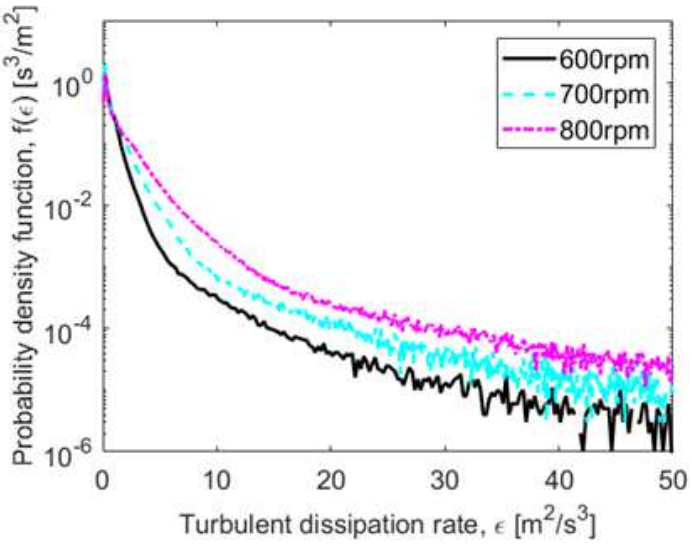

Figure 3.8 - A probability density function of the turbulent dissipation rate for the case of the Isane, obtained by using CFD simulations

4 RESULTS AND DISCUSSION

4.1 EXPERIMENTAL RESULTS

Kernels validation was carried out through several experiences, which provided the data necessary for the evaluation of the Sauter mean diameter. Tests started with the fulfilling of the reactor with the solvent; then, in the appropriate proportion the water was injected and the rotor was activated, by setting the right power in order to have the correct rotational speed. Thereafter, the endoscopic probe was immerged in the solution each 10-15 minutes, and the acquisition process was launched. Experiments were typically carried out for a duration of 5-6 hours. However, for low surface tension solvents, tests were conducted for 1-1,5 hours, since dimension droplets started to be too much small, misleading in the image processing. The post-treatment phase consisted in the analysis of the entire set of frames recorded and of the droplets size distribution. Finally, the experimental data were compared with the models.

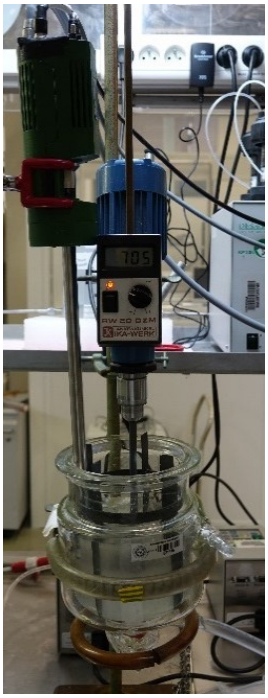

Figure 4.1 - The experimental device consists of the reactor, the rotor and the endoscopic probe.

4.1.1 Low viscous solvent – tests 1-3

In the first part of experimental phase, a low-viscous solvent was employed (μ = **1,2 cP**), allowing to complete Castellano et al.' results [22]. In particular, Isane was used as continuous phase and water as dispersed phase. The experimental conditions and some properties are indicated in the following table

Table 4.1 - Isane experimental conditions and properties.

Test number	Solvents				Conditions and properties			
	Marcol [%]	Isane [%]	TBP [%]	Water [%]	Duration [h]	μ [cP]	ρ [Kg/m^3]	Δσ [mPa.s]
1 - 3	0	100	0	2%	6	1,219	757,4	38,30

On the basis of these properties, Reynolds numbers have been estimated for each rotational speed set, in order to validate the fully turbulent conditions assumption:

Table 4.2 - Re number depends on rotational rate. The values for the Isane case have been estimated.

Rotational speed [rpm]	Re number μ=1,2 cP
600	22368
700	26096
800	29824

According to the *Handbook of Industrial Mixing*, the limit of the fully turbulent regime in a stirred tank reactor is estimated over Re=10000 [3], hence the assumption was respected for each case.

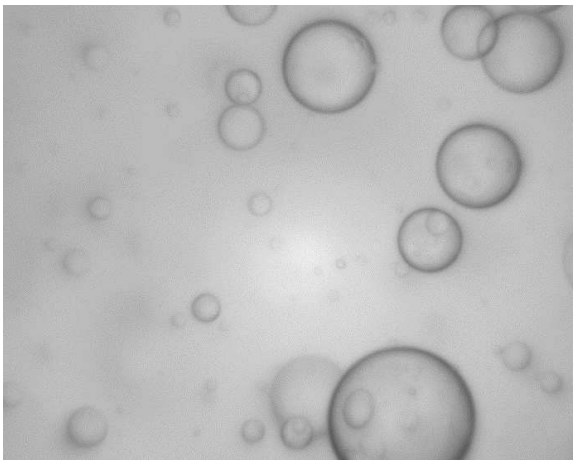

Figure 4.2 - Frame taken at 600 rpm.

The table 4.3 summarizes Sauter diameters evolution over time, for the three experiences. We can note that the gap between the first value and the last one is between 40 – 50 μm for the tests performed at 600 and 800 rpm. However, the 700 rpm experience shows a larger gap of about 70 μm. Besides, the initial size distributions appear decreasing, except for the 700 rpm test. These strange behaviors were due to a lower initial velocity, which affected the first measure.

Table 4.3 - Sauter diameter evolution over time at different rotational rates.

Conditions	2% 600 rpm	t [s]	2% 700 rpm	t [s]	2% 800 rpm	t [s]
Sauter diameters [μm]	302,91	0	345,33	0	290,20	0
	295,70	1740	310,17	4200	263,81	7200
	265,98	7620	300,82	10260	254,83	13020
	261,57	16680	277,93	16260	246,56	16200

4.1.1 Higher viscous solvents– tests 4-12

By adding the Marcol in different proportions, the viscosity was increased up to **2,4 cP** and **4,1 cP**. Hereunder, properties and experimental conditions are shown:

Table 4.4– Isane and Marcol were blended in different proportions. Here experimental conditions and properties are indicated.

Test number	Solvents			Conditions and properties				
	Marcol [%]	Isane [%]	TBP [%]	Water [%]	Duration [h]	μ [cP]	ρ [Kg/m^3]	Δσ [mPa.s]
4 - 6	30	70	0	1% - 2%	6	2,429	783,4	38,21
7 - 12	45	55	0	1%	6	4,102	799,9	39,81

The increased viscosity prevents the full developed turbulent regime, since it is necessary to apply higher forces in order to overcome fluid resistances. For this purpose, Reynolds numbers were calculated for each test:

Table 4.5 - Re number have been estimated when viscosity has been increased.

Rotational speed [rpm]	Re number	
	μ=2,4 cP	μ=4,1 cP
600	11611	7020
700	13546	8190
800	15481	9360

Even if Re are lower for the case of viscosity 2,4 cP than previous tests at 1,2 cP, the limit set to 10000 [3] is widely exceeded. This condition is not respected by 4,1 cP tests. However, Hockey and Nouri [26] shows that in a similar system, turbulence conditions can be already achieved for Re > 1500. Hence, on the basis of this new assumption, we can still consider the system turbulent.

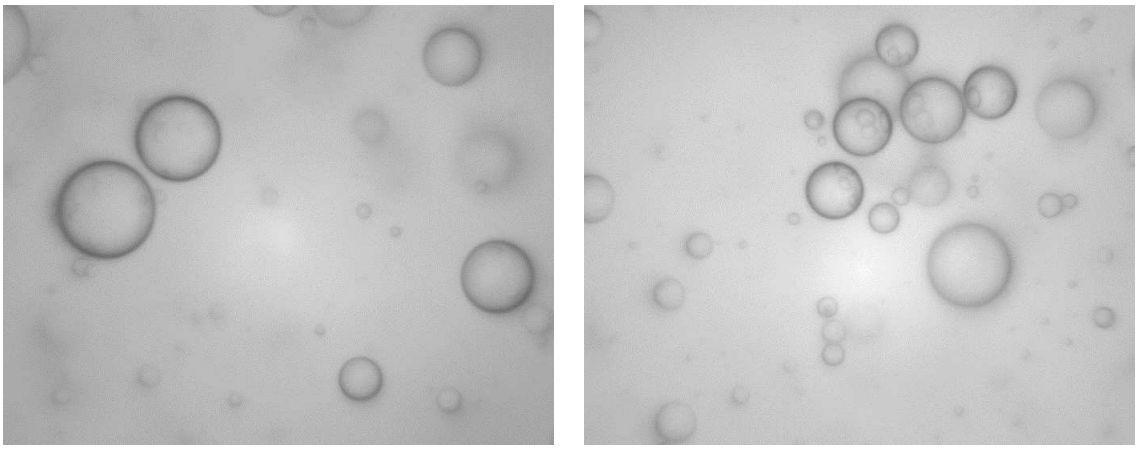

Figure 4.3 - On the left, 2,4 cP test at 600 rpm, on the right, 4,1 cP at 600 rpm. Drops sizes seem to appear smaller when viscosity is increased, at the same rotational speed.

Concerning drops sizes, since the interfacial tension remains quite similar to those of the other solvents, droplets approximately have the same Sauter diameter. However, dimensions it seems that the decrease over time is less than the 1,2 cP, shown in table 4.3. Indeed, droplets are generally affected by two factors: the quantity of water and the rotational speed. Indeed, a smaller water fraction generates, proportionally, smaller droplets. In particular, in the table 4.6, a difference of approximately 30 μm can be observed for tests at the same rotational speed when water fraction increases from 1% to 2% (μ = 2,4 cP). Regarding the second factor, higher values of velocity increase the Reynolds number and hence the turbulence in the dispersion. This causes increased shear stresses, promoting the droplets breakage. In terms of energy, the rotor rises the dissipated fraction. Furthermore, viscosity plays a key role in breakage and coalescence mechanisms. In particular, in the table 4.6 we note that when viscosity increases, droplets are smaller. Probably, viscous forces become more important than inertial forces, causing a more efficient breakage of the drops. Indeed, by looking at diameters variations for each test, we can note that in the case of μ = 2,4 cP Sauter diameters decreased of about 20 – 40 μm when water fraction is 1% and 30 – 50 μm when aqueous phase is set to 2%. On the contrary, in the 4,1 cP case, the gap between the first and last value is just about 10 μm. This confirms the assumption that viscous forces are predominant but *"slower"* than the inertial ones. Indeed, the lower turbulence, always caused by viscous forces, reduce breakage and coalescence efficacy over time since energy and momentum transfers become slower.

Table 4.6 - Sauter diameter evolution over time at different rotational rates

Marcol 30% + Isane 70% - μ = 2,4 cP						
Conditions	**1% 600 rpm**	**t [s]**	**1% 700 rpm**	**t [s]**	**1% 800 rpm**	**t [s]**
Sauter diameters [μm]	297,70	0	270,66	0	263,64	0
	284,34	1800	260,62	2400	256,63	1020
	273,15	8700	242,08	9180	245,78	1920
	256,33	16260	232,43	11880	240,28	3420
Marcol 30% + Isane 70% - μ = 2,4 cP						
Conditions	**2% 600 rpm**	**t [s]**	**2% 700 rpm**	**t [s]**	**2% 800 rpm**	**t [s]**
Sauter diameters [μm]	325,06	0	310,36	0	274,19	0
	311,45	3120	285,92	660	262,92	1500
	296,30	7680	267,68	2400	257,55	4920
	276,81	14640	253,52	4380	241,83	13320
Marcol 45% + Isane 55% - μ = 4,1 cP						
Conditions	**1% 600 rpm**	**t [s]**	**1% 700 rpm**	**t [s]**	**1% 800 rpm**	**t [s]**
Sauter diameters [μm]	288,90	0	277,95	0	252,69	0
	285,85	4800	272,63	3540	248,66	2940
	279,61	9000	265,19	7740	242,45	7140
	275,69	17340	251,12	16740	233,13	13920

4.1.1 Low interfacial tension solvents– tests 13-24

In order to approach experimental conditions to those of the PUREX process, the TBP was added to the Isane. Surface tension was reduced by approximately 70 – 80% of the previous values, leading to a significantly decrease of droplets size. Indeed, drops diameters have been proportionally reduced of about 70%. At a later stage, also Marcol was blended in order to increase solvent viscosity.

Table 4.7 - Isane and Marcol were blended in different proportions. Here experimental conditions and properties are indicated.

Test number	**Solvents**			**Conditions and properties**				
	Marcol [%]	**Isane [%]**	**TBP [%]**	**Water [%]**	**Duration [h]**	**μ [cP]**	**ρ [Kg/m³]**	**Δσ [mPa.s]**
13 - 18	0	70	30	1% - 2%	1,5	1,608	821,4	10,50
19 - 24	30	40	30	1% - 2%	1,5	3,384	848,2	15,90

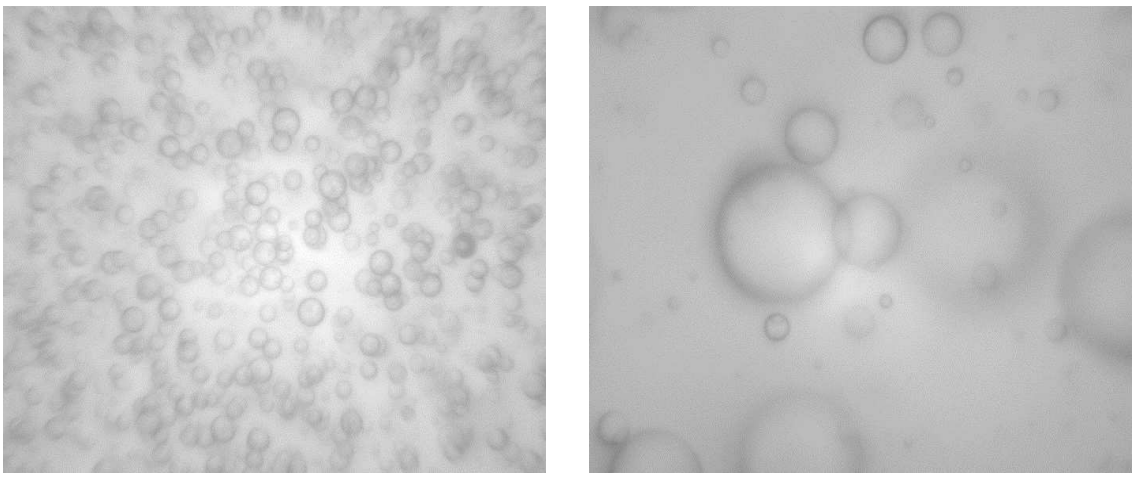

Figure 4.4 - Interfacial tension drop allowed to obtain smaller droplets in the TBP+Isane (on the left) system. Here droplets have been compared with the case of the Isane (on the right).

Since density was increased thanks to the TBP, Reynolds numbers significantly exceed Hockey and Nouri's limit [26], as we can see in the following table:

Table 4.8 – The limit of full turbulence, according to Handbook of Industrial Mixing's definition, is guaranteed in almost all the tests.

Rotational speed [rpm]	Re number	
	μ=1,6 cP	μ=3,4 cP
600	18390	9023
700	21454	10527
800	24519	12031

Sauter diameters increase with water fraction in both cases of about 10 μm, and decrease with higher rotational rates of about 15 – 20 μm. At this stage, since drops attaint the sensitivity threshold of the probe, values are affected by a significant error. Hereunder, we show how Sauter diameter evolve over time and in different conditions of water fraction and rotational speed:

Table 4.9 - Sauter diameter evolution over time at different rotational rates

TBP 30% + Isane 70% - μ = 1,6 cP						
Conditions	**1% 600 rpm**	**t [s]**	**1% 700 rpm**	**t [s]**	**1% 800 rpm**	**t [s]**
Sauter diameters [μm]	66,023	0	57,20	0	56,21	0
	65,624	600	54,67	2460	54,60	720
	64,106	1380	53,04	3540	54,80	1980
	61,524	3000	52,80	4200	50,48	3120
TBP 30% + Isane 70% - μ = 1,6 cP						
Conditions	**2% 600 rpm**	**t [s]**	**2% 700 rpm**	**t [s]**	**2% 800 rpm**	**t [s]**
Sauter diameters [μm]	82,34	0	71,81	0	67,27	0
	80,47	2040	70,72	840	66,92	1680
	79,19	4440	70,33	2700	66,57	2760
	78,51	5700	69,40	4440	65,85	4560
TBP 30% + Marcol 30% + Isane 40% - μ = 3,4 cP						
Conditions	**1% 600 rpm**	**t [s]**	**1% 700 rpm**	**t [s]**	**1% 800 rpm**	**t [s]**
Sauter diameters [μm]	72,21	0	64,67	0	77,91	0
	64,80	1500	59,67	1440	74,68	720
	61,76	2640	56,42	3960	67,45	1800
	56,34	3900	54,65	5040	66,39	2940
TBP 30% + Marcol 30% + Isane 40% - μ = 3,4 cP						
Conditions	**2% 600 rpm**	**t [s]**	**2% 700 rpm**	**t [s]**	**2% 800 rpm**	**t [s]**
Sauter diameters [μm]	86,20	0	74,84	0	69,01	0
	83,93	2040	72,70	1020	68,97	1440
	82,76	3300	72,32	2820	68,52	3360
	82,18	4980	72,19	5160	68,04	4860

4.2 MODELING RESULTS

In this section, the results are introduced with an exhaustive discussion. As a first step, we show results concerning the initial model, by highlighting the main differences with the use of ε and its PDF. A first validation of this approach has been provided by Castellano et al.[22] by employing water as continuous phase and Isane as organic dispersed phase. In his study, Castellano also inverted the phases by validating the method for the case of 1% of water in Isane organic continuous phase, as shown in the following graphs:

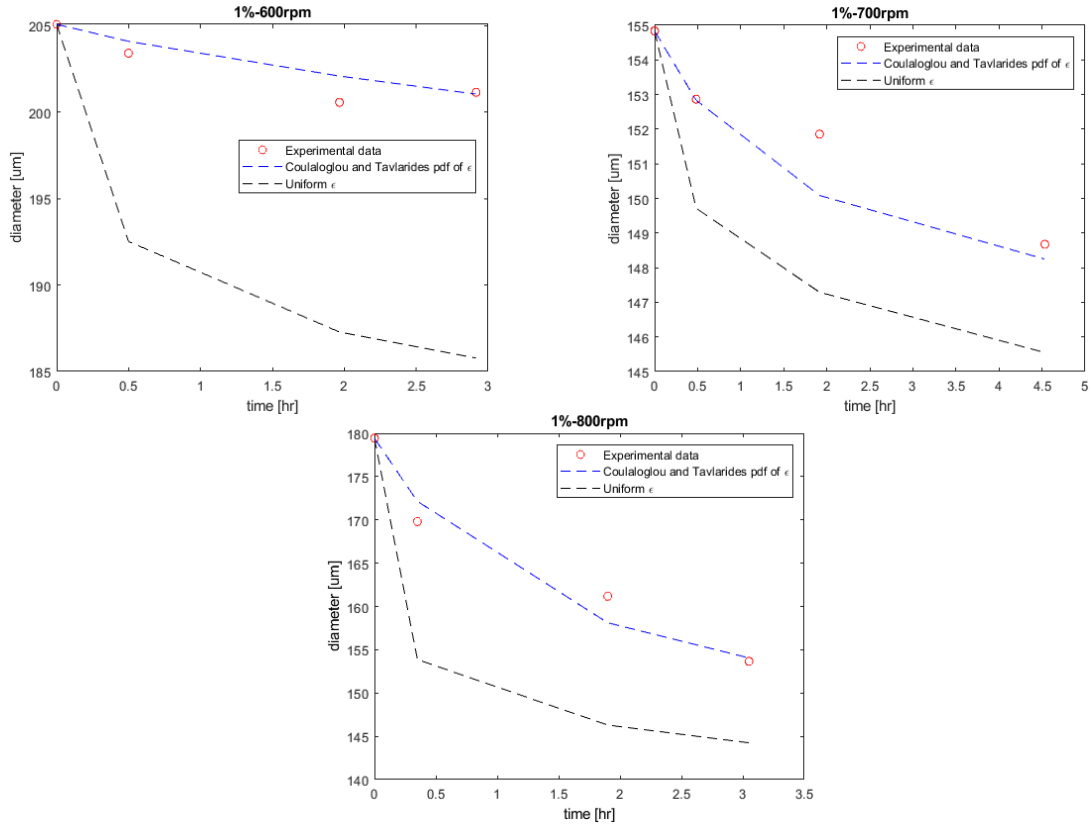

Figure 4.5 - Castellano et al. - 1% water in organic phase results

In this part, we explain why it was necessary to proceed towards a new definition of energy spectrum and thus through a new formulation of the kernels.

In the second part, we present the results for the improved model. We tested this new approach by employing several solvents presenting different properties, in order to extend its utilization to all the possible cases. It should be remembered that the main purpose of the experiments was to approach the PUREX process conditions, which is the reason why we move towards a more viscous set up.

Table 4.10 - Model parameters have been obtained by fitting the experimental data with the three different proposed approaches.

	Uniform ε	Initial model	Advanced model
k1	0,0784	0,0012	2,23E-04
k2	0,306	0,711	0,708
k3	0,000375	0,0195	1,0073
k4	8,23E+18	2,05E+14	1,68E+18

Here it is important to highlight that the model parameters, showed in table 4.10, have been obtained by fitting the *Initial model* with **1-2% Isane in water 600 rpm** tests and by fitting the

Advanced model with **1-2% water in Isane 600 rpm** tests. These parameters have been used to interpolate other experiences data, by showing very good results. Thus, the parameters allow a completely predictive behaviour for the model, independently of the operative conditions.

Finally, we show model limits of validity when droplets size crossed the *Dissipation range* boundary, represented by the Kolmogorov length scale.

4.2.1 Initial model – test on Isane experiences

As we saw in the chapter 2, in order to solve PBEs is necessary to formulate a kernel function for the coalescence and another one for the breakage of droplets. The Coulaloglou and Tavlarides' definition has been employed by computing the volume-average through the PDF of epsilon. The first part of this work consisted on testing Castellano et al. approach to a higher volume fraction (2%) of water in continuous organic phases. Therefore, experiments at this water volume fraction were performed and the model tested:

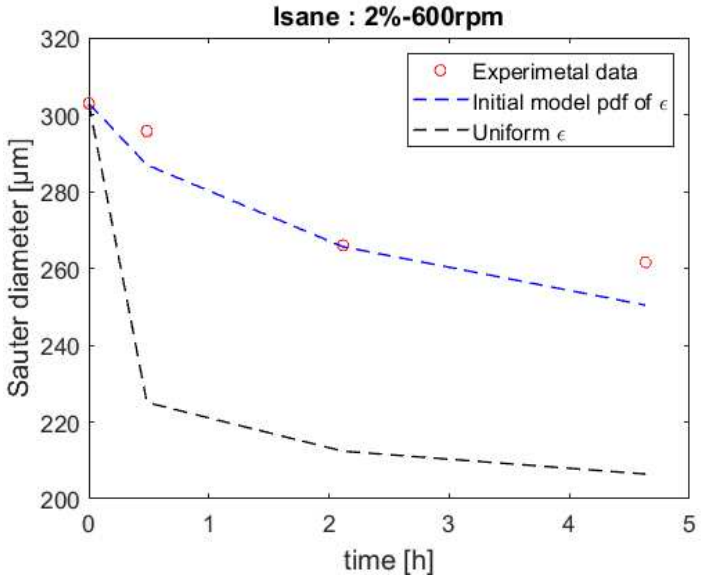

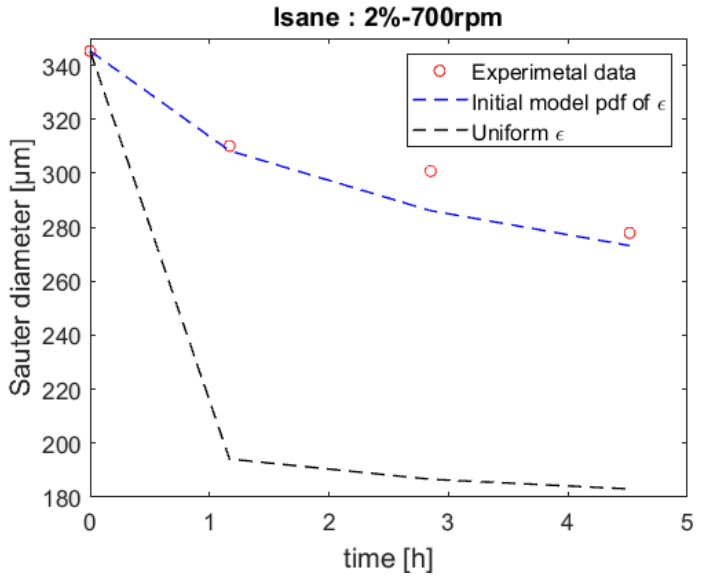

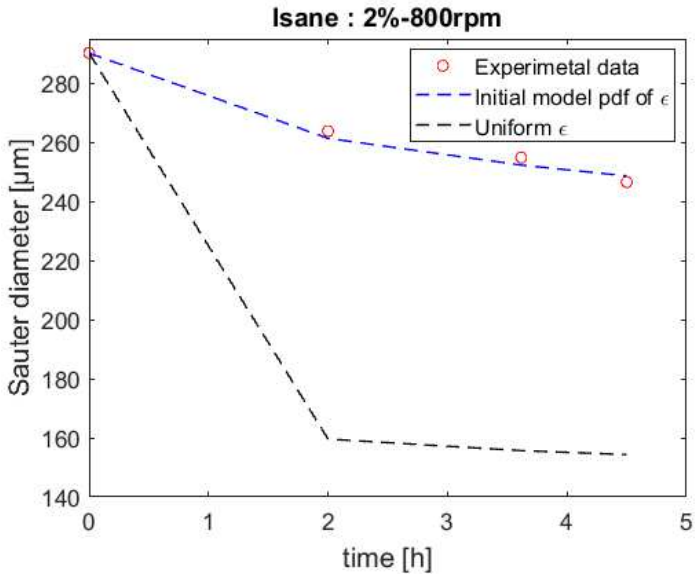

Figure 4.6 - 2% water in organic continuous phase confirm the validity of the model for 600, 700 and 800 rpm.

The model fit perfectly with experimental data collected. A wide spread can be observed between the Castellano et al. approach and the classic use of $\bar{\varepsilon}$ uniform. In fact, by considering the turbulent dissipation rate uniform, we are assuming that across the reactor turbulence is higher than its real value, leading to a breakage frequency overestimation.

We can finally affirm that the **Castellano et al. model can be employed indifferently with organic or water as continuous phase at low viscosity.**

4.2.1.1 More viscous systems

The second part of the work, we proceeded to extend the model to more viscous systems. First, we tested Castellano's model on experiments at higher viscosity, **2,4 cP** and **4,1 cP**. Here under we present the model fitting:

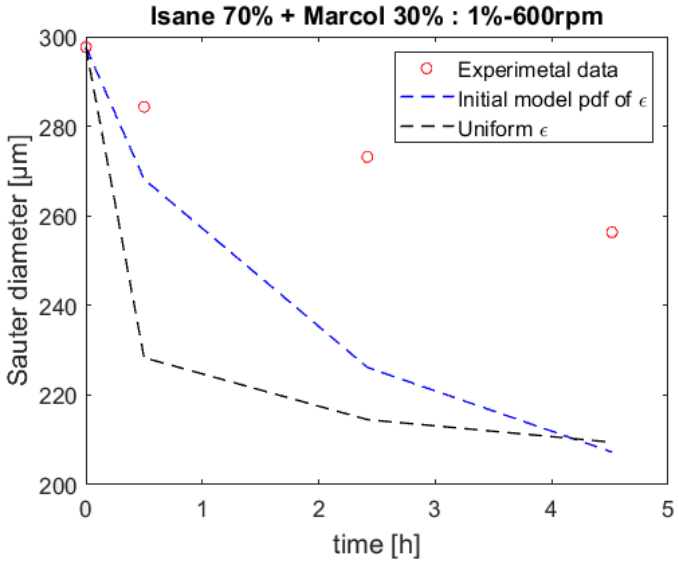

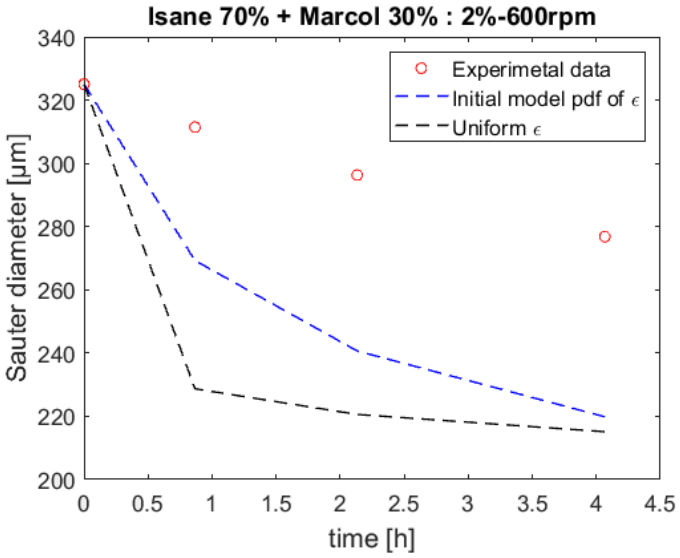

Figure 4.7 - When viscosity reaches a value of 4,2 cP the model is not able to fit data. Particles are prevalently in the Dissipation range and the model overestimates dissipated energy and thus breakage frequency.

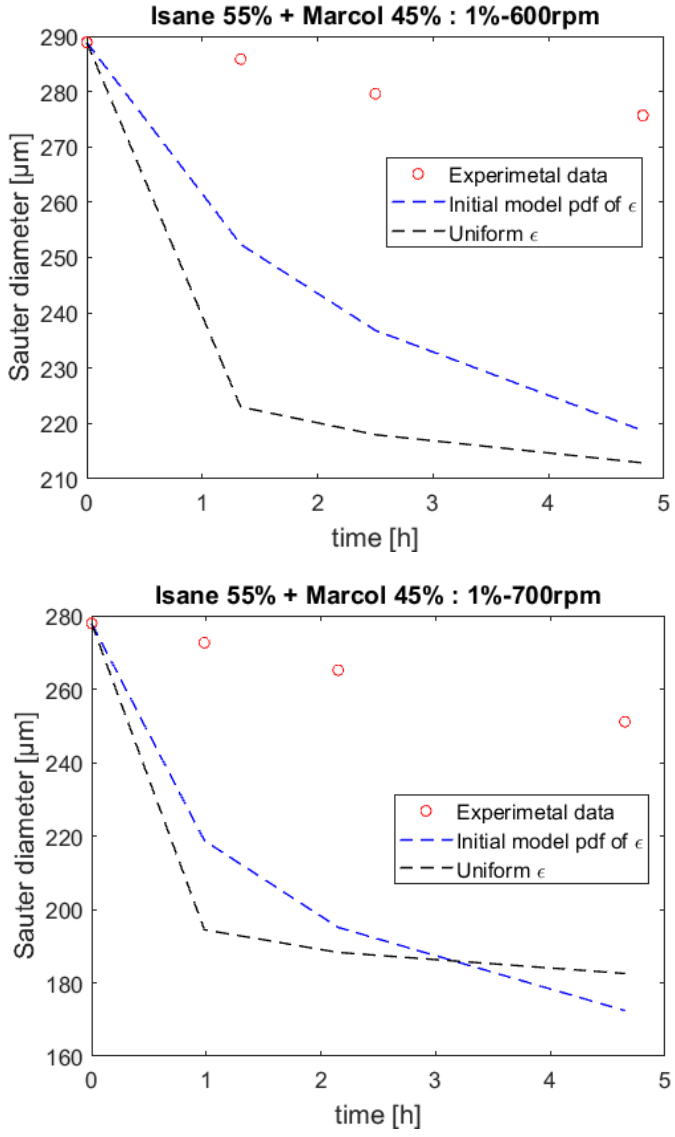

Figure 4.8 - The same result is achieved when the viscosity has a value of 4,1 cP.

The figures 4.7 and 4.8 show how the model cannot predict Sauter mean diameter evolution over time when more viscous solvents are employed. In fact, in a similar system, the droplet dimension resides in the Dissipation Range, which follows a different eddies energy distribution if compared to the Inertial one. Indeed, by applying the model based on CT kernels, which considers the *-5/3 Kolmogorov's law,* we are extending the *Inertial Subrange*'s pattern to the *Dissipation Range*, as we saw in the paragraph 2.1.4. It is important to remark that the increased viscosity affects the Kolmogorov scale value η and consecutively the limit between the Inertial and Dissipation subranges ($l_{DI} \approx 60\eta$) [13].

Table 4.11 - Dissipation range boundaries depend on rotational speed and viscosity. In particular, when μ is increased, the range becomes wider.

	μ = 2,4 cP		**μ = 4,1 cP**	
ε	**η [μm]**	**l_{DI} [mm]**	**η [μm]**	**l_{DI} [mm]**
0,63	82,94	4,98	120,96	7,26
1	73,89	4,43	107,76	6,47
1,47	67,1	4,03	97,87	5,87

Here we note that by increasing the viscosity, the size of the *Dissipation Range* becomes more and more important. For instance, in the following figure we can note that almost the entire distribution is contained in the *Dissipation Range*. This is why more viscous systems are more sensitive to the energy dissipation overestimation.

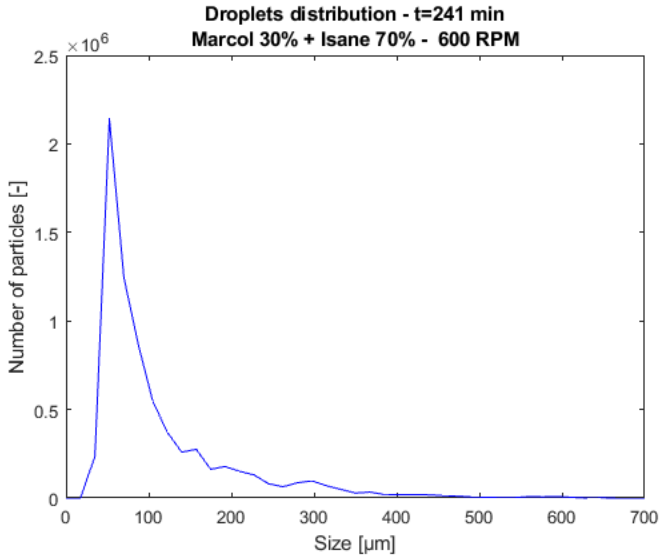

Figure 4.9 - Droplet size distribution for the case of μ=4,2 cP at t=241min

4.2.2 Advanced model

In order to account for the smaller energy dissipation, we modified Coulaloglou and Tavlarides' kernels by using the new energy spectrum provided by Pope [13] and the new square relative velocity definition provided by Davidson [24]. For this reason henceworth we refer to this model as the *Advanced model*. In this version of the model we are still considering turbulence inhomogeinities by employng the PDF of ε.

4.2.2.1 Isane tests

First of all, the new kernels definition was tested on the 1-2% water in Isane tests. In this way it has been possible to compare Castellano's results with the new formulation. Hereunder we present them:

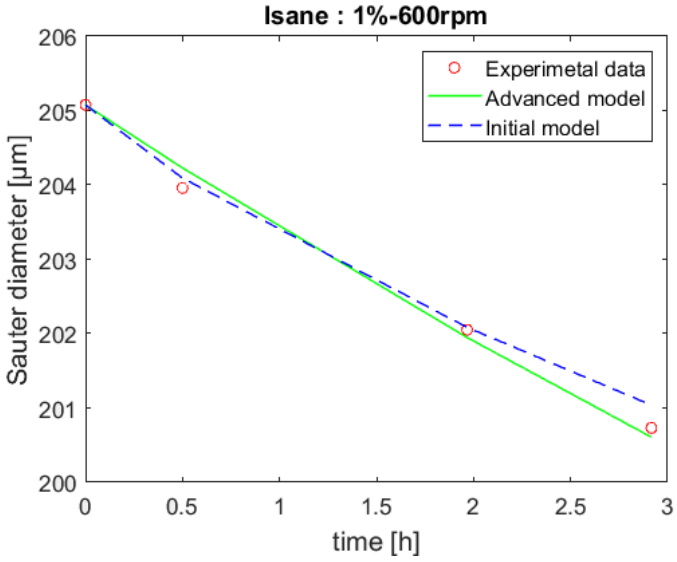
Isane : 1%-600rpm
Experimetal data
Advanced model
Initial model
Sauter diameter [µm]
time [h]
206
205
204
203
202
201
200
0
0.5
1
1.5
2
2.5
3

(a)

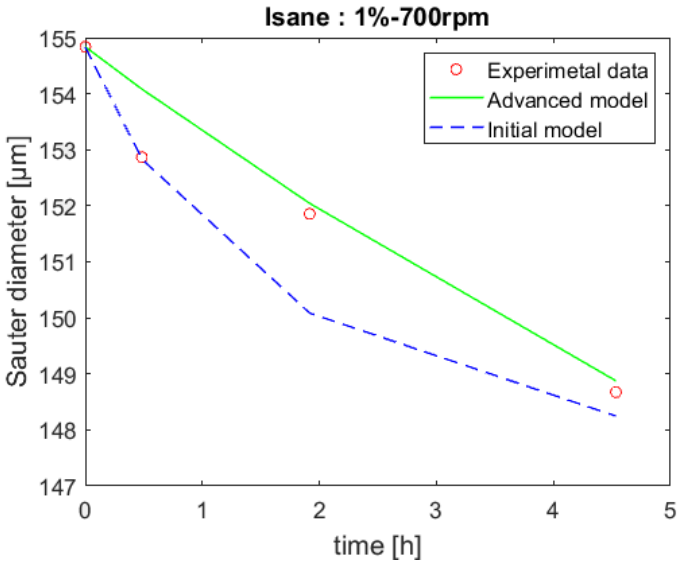
Isane : 1%-700rpm
Experimetal data
Advanced model
Initial model
Sauter diameter [µm]
time [h]
155
154
153
152
151
150
149
148
147
0
1
2
3
4
5

(b)

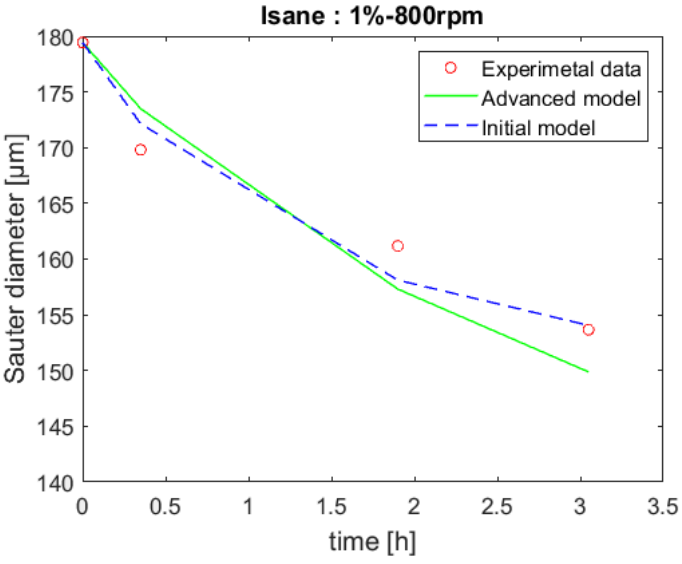
Isane : 1%-800rpm
Experimetal data
Advanced model
Initial model
Sauter diameter [µm]
time [h]
180
175
170
165
160
155
150
145
140
0
0.5
1
1.5
2
2.5
3
3.5

(c)

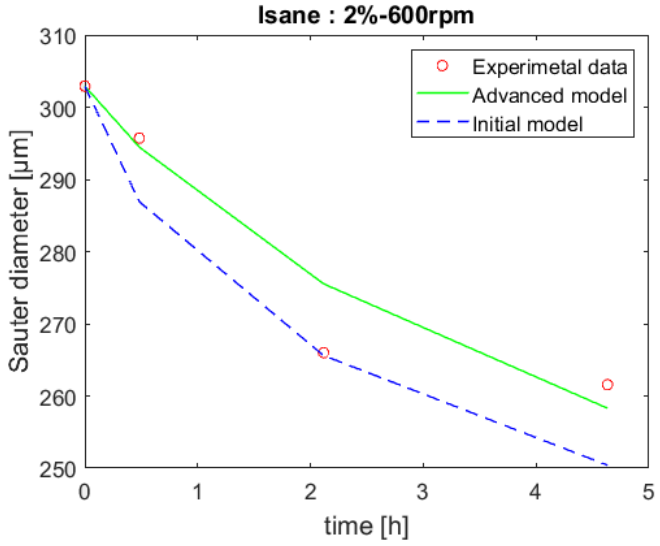

(d)

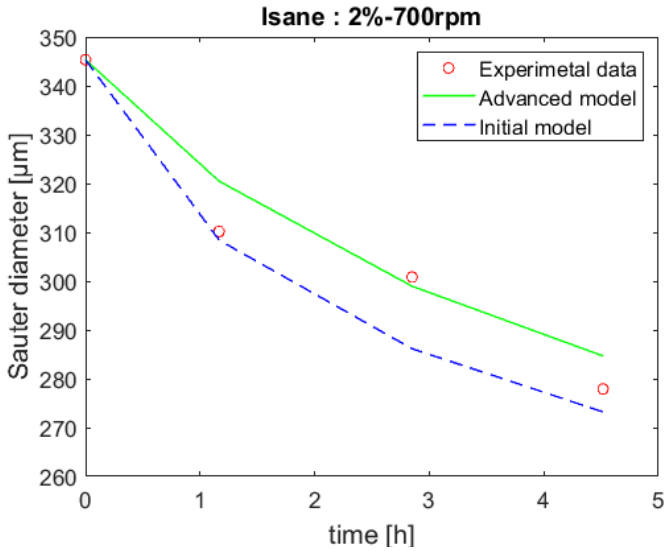

(e)

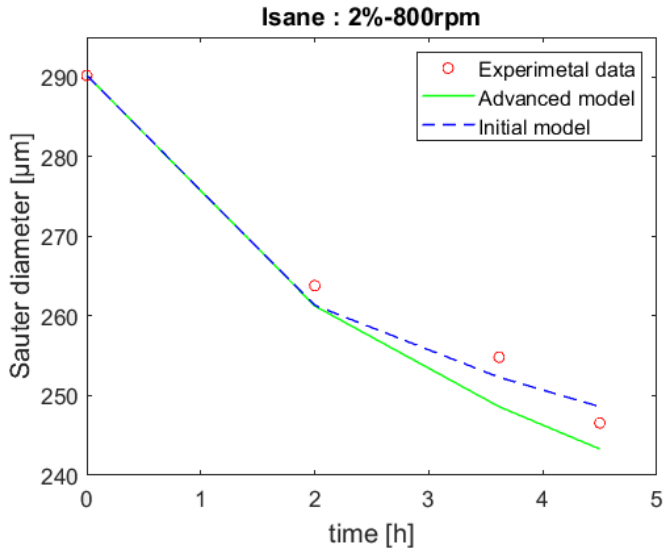

(f)

Figure 4.10 - Results show how in both cases 1% (a,b,c) and 2% (d,e,f) of water, the new model fit very well experimental data.

Figure 4.10 shows how the two versions of the model can interpolate the experimental data. In the graphs a, b, c both approaches seem to fit very well experimental data. This is due to fact that these data have been used to obtain model parameters, hence the model have been built on these experiences data. Nevertheless, in the graphs d, e, f the *Initial model* shows a small gap with the real pattern, while the *Advanced model* approximate quite well the experimental data. Once again, this gap is almost due to the overestimation of the dissipation energy.

4.2.2.2 Increased viscosity to μ=2,4 cP

Solvent viscosity was firstly increased up to **2,4 cP**.

In the following graphs we observe that the new version of the model is able to fit experimental data. On the contrary, the *Initial model* shows a significant deviation.

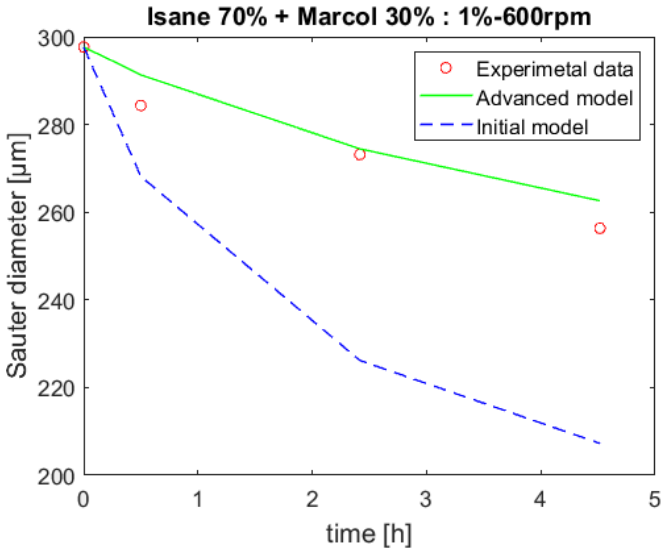

(a)

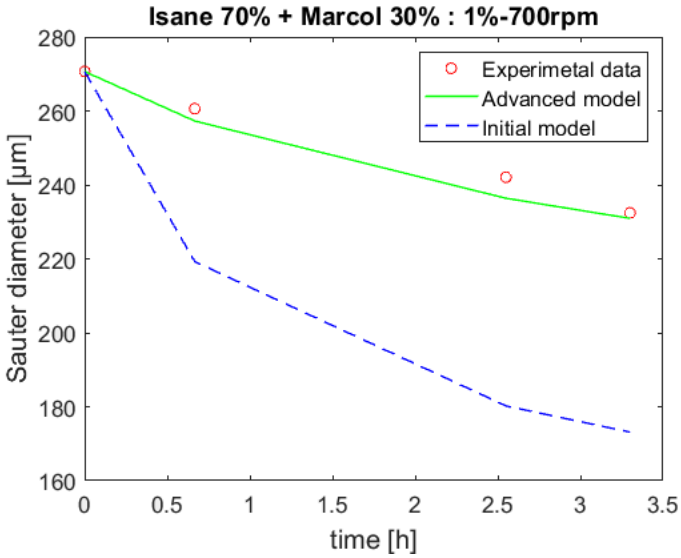

(b)

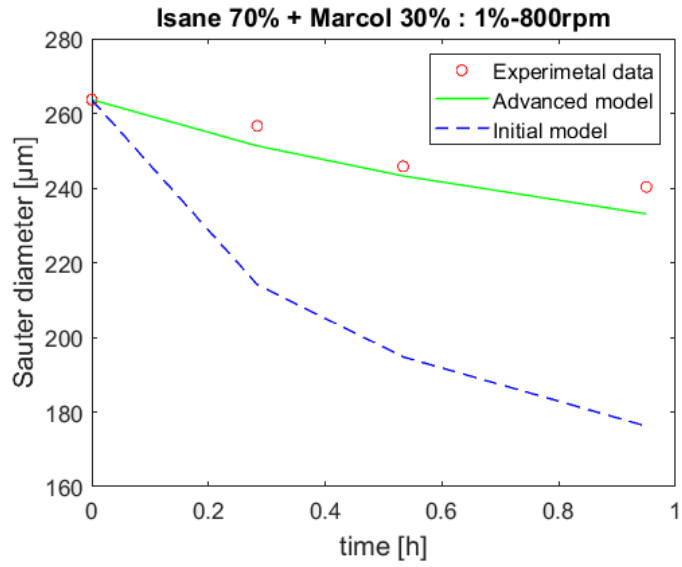
Isane 70% + Marcol 30% : 1%-800rpm
Experimetal data
Advanced model
Initial model
Sauter diameter [µm]
time [h]
280
260
240
220
200
180
160
0
0.2
0.4
0.6
0.8
1

(c)

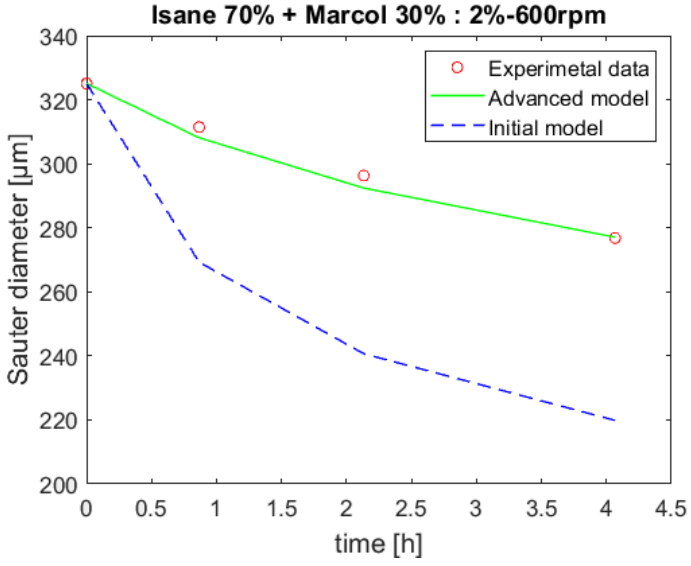
Isane 70% + Marcol 30% : 2%-600rpm
Experimetal data
Advanced model
Initial model
Sauter diameter [µm]
time [h]
340
320
300
280
260
240
220
200
0
0.5
1
1.5
2
2.5
3
3.5
4
4.5

(d)

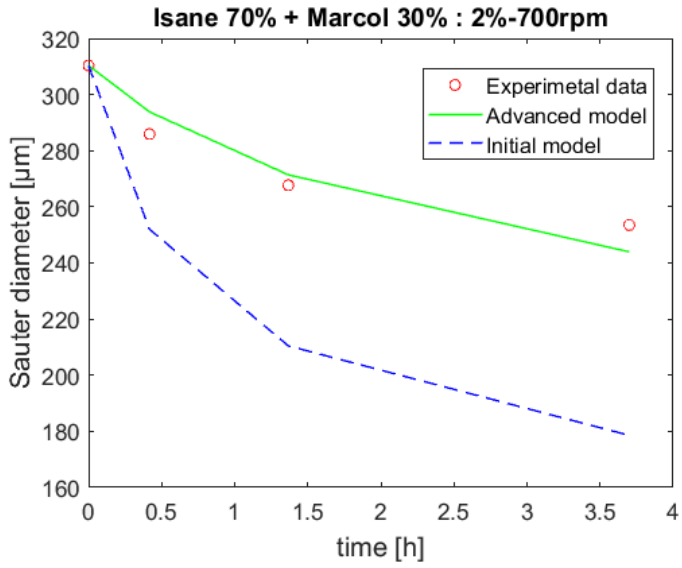
Isane 70% + Marcol 30% : 2%-700rpm
Experimetal data
Advanced model
Initial model
Sauter diameter [µm]
time [h]
320
300
280
260
240
220
200
180
160
0
0.5
1
1.5
2
2.5
3
3.5
4

(e)

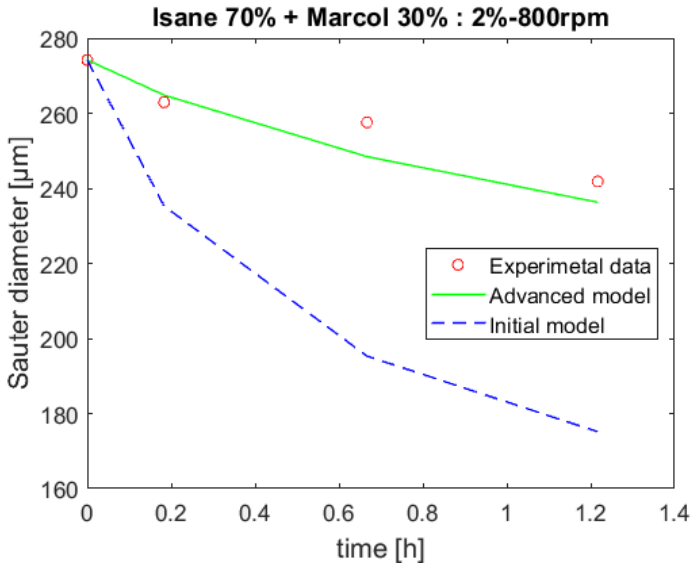

(f)

Figure 4.11 - The improved version of the model seems to fit very well the experimental points, even when µ=2,4 cP. These graphs show the gap with the old version.

As we can see in the graphs in figure 4.11, the new version of the model gives good results. These results have been achieved by employing the same model parameters. Thus, we can affirm that in this case the model can be considered completely predictive. On the basis of these results we can validate the hypothesis that in more viscous systems the *Dissipation Range* becomes larger and the Kolmogorov's energy spectrum is more "expensive" in terms of dissipated energy. Indeed, the difference between the initial and the advanced methods approaches concerns the dissipated energy in the *Dissipation* range. The gap shown in the graphs between the two curves is essentially due to a significant breakage frequency overestimation in the initial model, which assumes the *-5/3 law of Kolmogorov* also in the Dissipation subrange and therefore a higher turbulent kinetic energy dissipation. This is why the initial model tends to smaller diameters.

4.2.2.1 Increased viscosity to µ=4,1 cP

In tests 4 to 6, we provided a further augmentation for the solvent viscosity. Thus, we reached a value of **4,1 cP**.

Hereunder, we show the results for this series of tests.

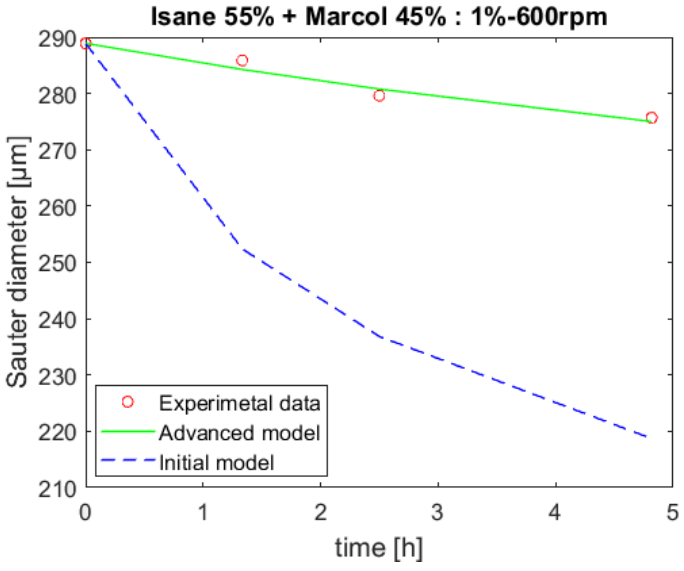

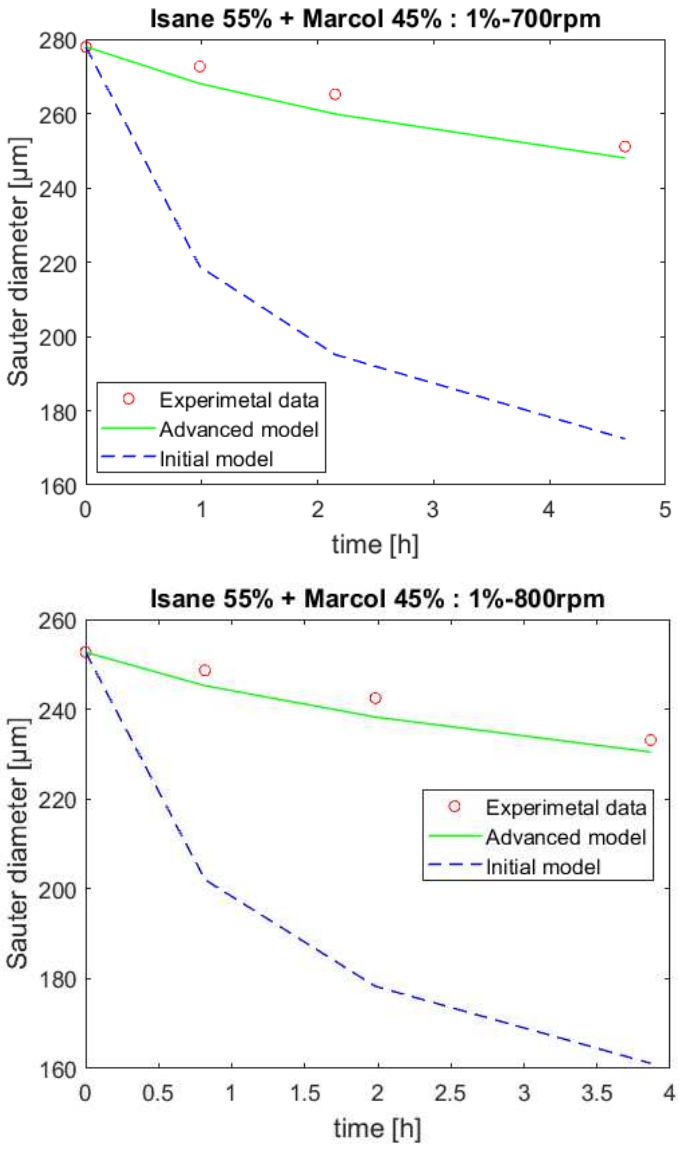

Figure 4.12 - The model produces good results even when a more viscous solvent is employed.

According to results, the improved model produces satisfactory outcomes even when viscosity is increased to 4,1 cP. Once again, these results have been achieved by using the same model parameters. That is why even in this case the model could be considered completely predictive. However, this time, we can observe that the gap between the two versions of the model becomes bigger. In fact, as we showed previously, the increased viscosity of the solvent widens the *Dissipation range*, and consequently expands the dissipated energy spread. Once again, the Initial model over-predicts the breakage frequency, leading to smaller diameters values.

4.2.2.2 Low interfacial tension systems

From test 13 to 24, we introduced in the system the TBP, which strongly reduced interfacial tension between the solvent and the water phase. Two different viscosities were tested, **1,6 cP** and **3,4 cP**.

In the following graphs we show some results for low interfacial tension experiences in which viscosity was changed. Further results have been attached to ANNEXES.

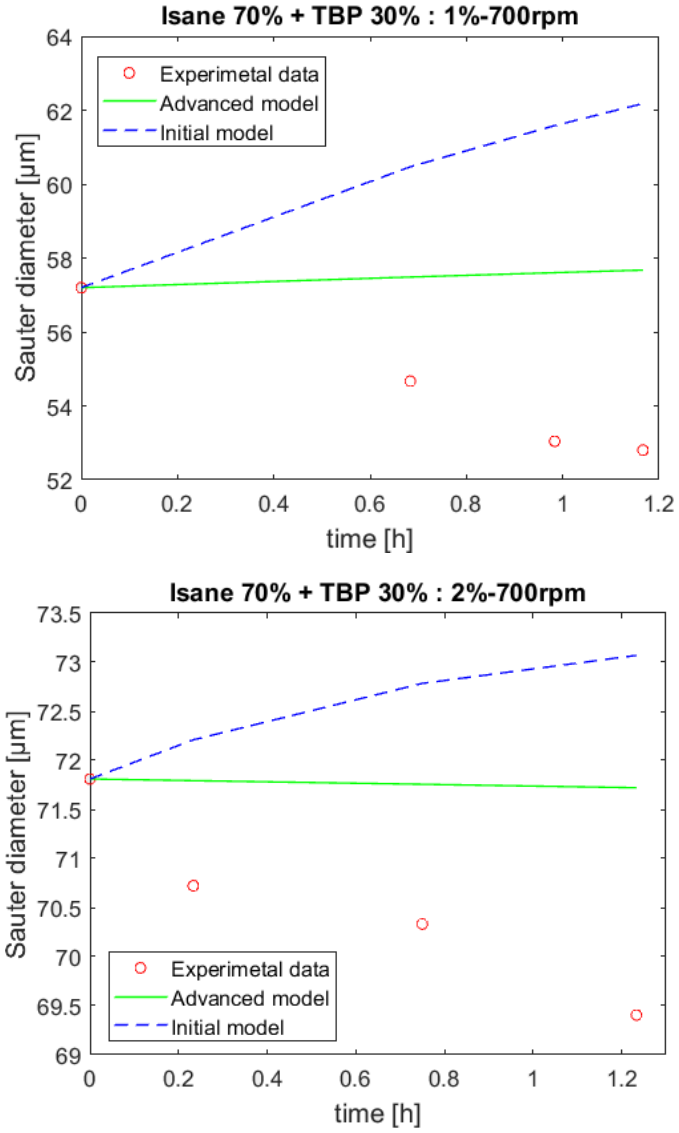

Figure 4.13 – At 700 rpm, both the versions of the model appear not capable to fit experimental data.

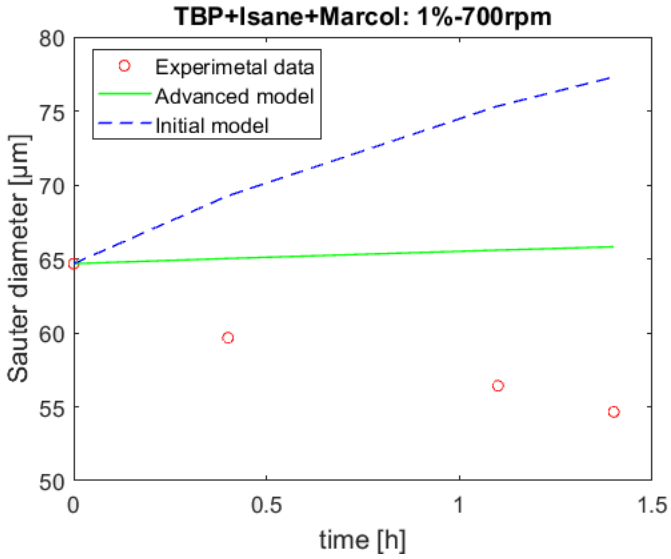

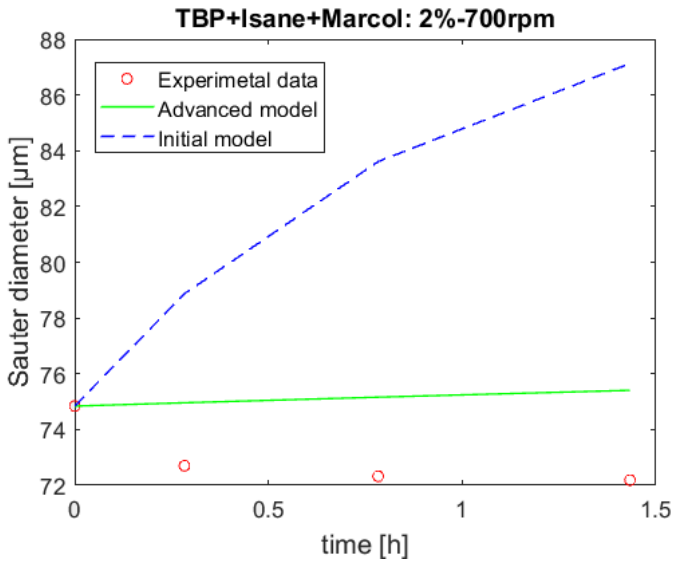

Figure 4.14 – By increasing viscosity in a low interfacial tension system, results are the same. The models do not produce good overcomes for this kind of systems.

In figures 4.13 and 4.14, graphs show that both model versions cannot predict the time size evolution for this kind of systems. In particular, for the *Initial model*, coalescence seems to overcome breakage, by predicting increased diameters. On the contrary, the *Advanced model* produces a constant pattern, which suggests a kind of equilibrium between coalescence and breakage events. We tried to give an explanation about these results.

As stated in the chapter 2, the Kolmogorov length scale is the lower *Dissipation range* boundary. This lower limit represents the smallest size an eddy can achieve in the cascade process before being dissipated by viscosity. If we consider the Kolmogorov length scales for each experience, we can easily see that in this system the droplets are smaller than this value, as shown in the following table:

Table 4.12 - Kolmogorov length-scale can be considered the Dissipation range boundary. In these experiences, η values were estimated bigger than almost the entire droplets size distribution.

	TBP + Isane	TBP + Isane + Marcol
Epsilon	**η [µm]**	**η [µm]**
0,63	58,74	100,20
1	52,34	89,27
1,47	47,53	81,07

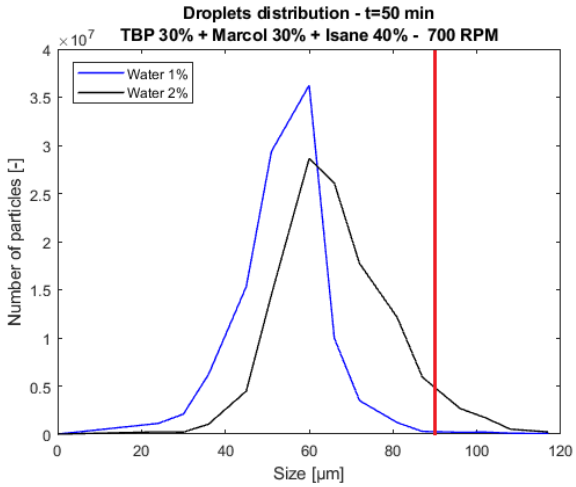

Figure 4.15 - Droplets size distributions for the case of µ=3,4 cP. The red line represents the Kolmogorov length scale.

For instance, by showing the distributions in figure 4.15 for the case of TBP + Marcol + Isane with the corresponding Kolmogorov length scales in the table (red line), we can observe that almost all of the particles have a size smaller than η. Hence, the dissipated energy tends to 0 when the eddy size approaches η. Furthermore, when droplets are out of the *Dissipation range* the system, at a microscopic scale, is no more turbulent and laminar forces cause droplet breakage. Thus, the models, based on turbulence theory, are not anymore able to produce satisfactory results.

5 CONCLUSIONS

In this work liquid-liquid dispersions behavior has been studied. In particular, the evolution of the droplets size distribution over time has been investigated through a population balance. This latter consists of an integro-differential equation which allows to follow particles size evolution over time and space through the *number density function*. The NDF derivative over time is equal to a source term which contains information about breakage and coalescence events. In particular, this information is expressed in mathematical terms called *kernels*. In literature several kernels are available, depending on phases involved in the system. In this work, the Coulaloglou and Tavlarides' expressions have been used, since they have been developed for liquid-liquid dispersions in turbulent conditions. In the kernels mathematical formulation, turbulence is taken in account through the turbulent dissipation rate ε. However, this value is considered uniform all over the space. When a dispersion is simulated in CFD, immediately we note that turbulence is not uniform in the space. In order to account for turbulent inhomogeneities, Buffo et al. [21] and Castellano et al. [22] have proposed to replace $\bar{\varepsilon}$ with its probability density function. The PDF represents the probability for ε to assume a value between ε and $\varepsilon + d\varepsilon$ in a certain zone of the space.

A first model, developed by Castellano et al. [22], has been tested in different conditions. In particular, solvent viscosity has been increased and interfacial tension reduced. Experimental data have been collected through several tests, allowing to compare model results with the real droplets Sauter diameter. Through a MATLAB routine, PBEs have been solved and the results have been compared with the *Initial model*. This latter has provided very good results whit low-viscosity solvents, showing that turbulent inhomogeneities lead to a significative improvement. However, when viscosity has been increased, the *Initial model* has been unable to predict size evolution over time.

At this stage, an improved model has been necessary. Starting from the Coulaloglou and Tavlarides' kernels, the second order correlation function has been redefined according to Davidson's definition. But, the most important evolution has concerned the eddies energy spectrum formulation. In particular, the Pope's definition has been employed in order to take in account droplets whose diameters were in the *Dissipation range*. Indeed, in the previous energy spectrum definition (*-5/3 law of Kolmogorov*), all the particles were considered in the *Inertial subrange*, leading to a dissipated energy overestimation.

The two versions of the model have been compared, by showing significant differences. In particular, the *Advanced model* has been produced satisfactory results, even with more viscous solvents. Nevertheless, when it has been employed to fit low interfacial-tension experimental data, it has been unable to predict the pattern. Indeed, the dramatic size decrease displace the droplets out of the *Dissipation range*, where turbulent conditions are no longer valid and breakage and coalescence mechanisms are provided by laminar forces.

Hence, a new model has been developed which can be employed in every domain where dispersions are used. In particular, by studying particles size evolution, it is possible to optimize equipment dimensions. Furthermore, process mass transfer can be better understood when droplets size distribution is known. These interesting applications find the interest of several engineering areas, such as oil and gas, pharmaceutical, food industries and also nuclear.

This work represents the cornerstone of a more important project. The *Advanced model* will be employed over other equipment, different from stirred tank reactors, by allowing to expand its field of application.

Further investigations are possible, especially concerning fluid particles out of the turbulent ranges. It would be interesting to build a model which can be applied in any condition. Besides, water fraction could be increased in order to validate the *moderate dilute system*, which has made possible to carry out single-phase CFD simulations. It would be possible account for a higher water fraction by performing multiphase CFD simulations. Finally, the dispersed phase could be replaced by a new compound providing a mass transfer between the two phases. It would be remarkable to modify the model in order to also account for mass transfer phenomena.

The interesting results presented in this manuscript, will be the object of a scientific paper.

ANNEXES

In this section, the results concerning low interfacial tension are presented:

TBP + Isane - μ = 1,6 cP

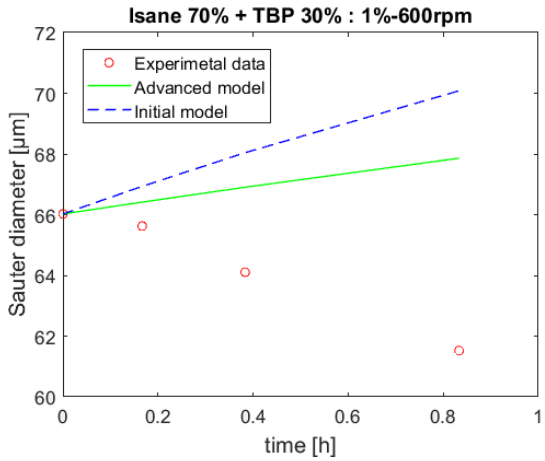

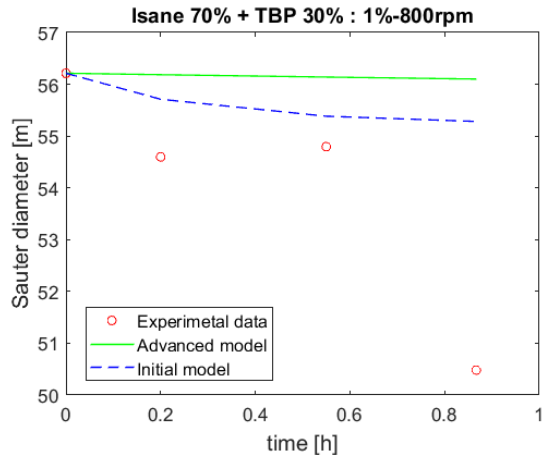

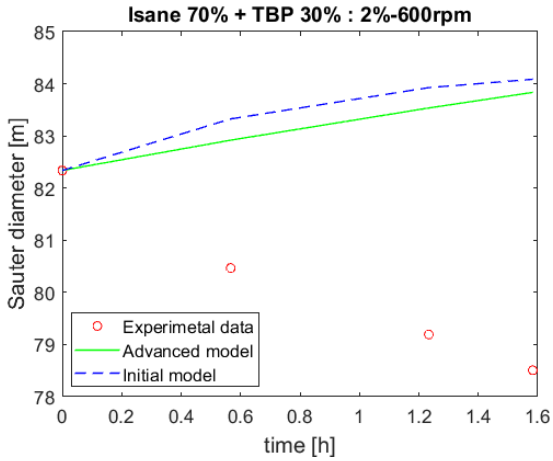

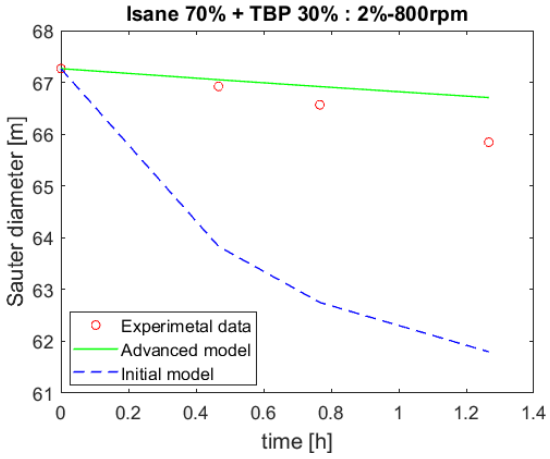

TBP + Marcol + Isane - μ = 1,6 cP

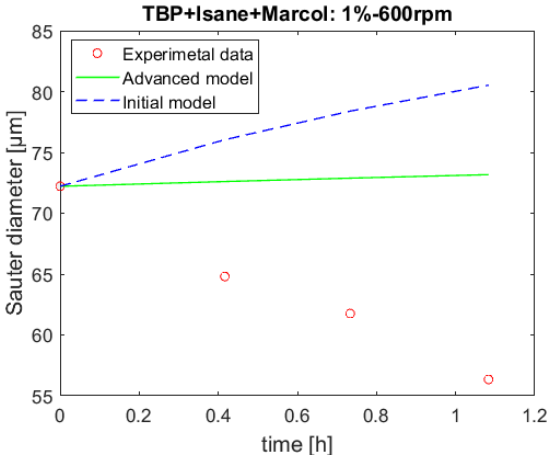

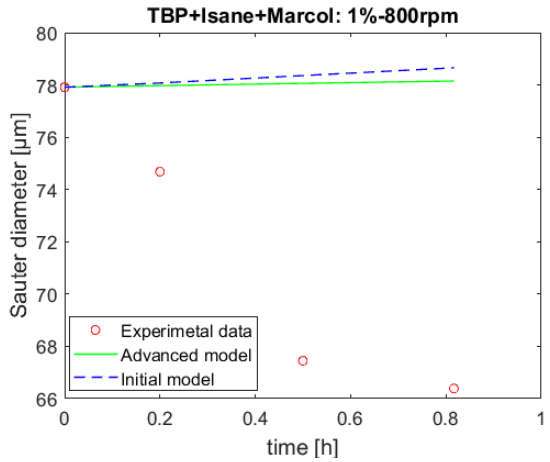

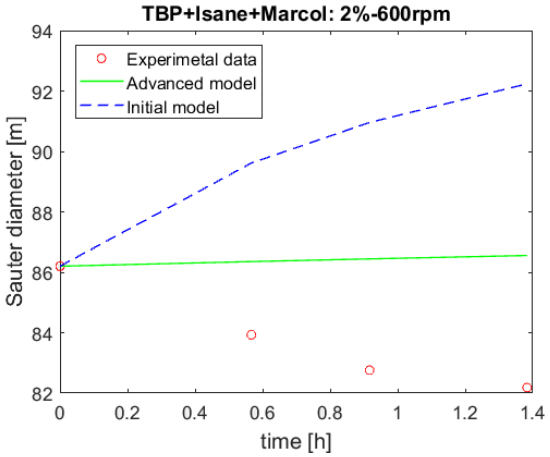
TBP+Isane+Marcol: 2%-600rpm
Experimetal data
Advanced model
Initial model
Sauter diameter [m]
time [h]
94
92
90
88
86
84
82
0
0.2
0.4
0.6
0.8
1
1.2
1.4

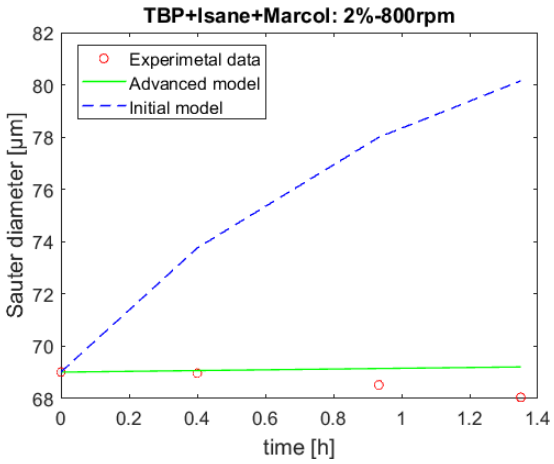
TBP+Isane+Marcol: 2%-800rpm
Experimetal data
Advanced model
Initial model
Sauter diameter [µm]
time [h]
82
80
78
76
74
72
70
68
0
0.2
0.4
0.6
0.8
1
1.2
1.4

LIST OF FIGURES

BIBLIOGRAPHY

[1] P. Paquin, "Technological properties of high pressure homogenizers: The effect of fat globules, milk proteins, and polysaccharides," *Int. Dairy J.*, vol. 9, no. 3–6, pp. 329–335, 1999.

[2] D. Guzey and D. J. McClements, "Formation, stability and properties of multilayer emulsions for application in the food industry," *Adv. Colloid Interface Sci.*, vol. 128–130, no. 2006, pp. 227–248, 2006.

[3] E. L. Paul, V. A. Atiemo-obeng, and S. M. Kresta, *Handbook of Industrial Mixing*. Hoboken, NJ, USA: John Wiley & Sons, Inc., 2003.

[4] S. Abid and A. K. Chesters, "The drainage and rupture of partially-mobile films between colliding drops at constant approach velocity," *Int. J. Multiph. Flow*, vol. 20, no. 3, pp. 613–629, 1994.

[5] C. A. Coulaloglou and L. L. Tavlarides, "Description of interaction processes in agitated liquid-liquid dispersions," *Chem. Eng. Sci.*, vol. 32, no. 11, pp. 1289–1297, 1977.

[6] A. W. Pacek, S. Chamsart, A. W. Nienow, and A. Bakker, "The influence of impeller type on mean drop size and drop size distribution in an agitated vessel," *Chem. Eng. Sci.*, vol. 54, no. 19, pp. 4211–4222, Oct. 1999.

[7] M. Stang, H. Schuchmann, and H. Schubert, "Emulsification in High-Pressure Homogenizers," *Eng. Life Sci.*, vol. 1, no. 4, p. 151, 2001.

[8] R. K. Thakur, C. Vial, K. D. P. Nigam, E. B. Nauman, and G. Djelveh, "Static Mixers in the Process Industriesða Review," *Trans IChemE*, vol. 81, no. August, 2003.

[9] D. Ramkrishna and A. W. Mahoney, "Population balance modeling. Promise for the future," *Chem. Eng. Sci.*, vol. 57, no. 4, pp. 595–606, 2002.

[10] D. Verkoeijen, G. A. Pouw, G. M. H. Meesters, and B. Scarlett, "Population balances for particulate processes - A volume approach," *Chem. Eng. Sci.*, vol. 57, no. 12, pp. 2287–2303, 2002.

[11] E. R. Irish and W. H. Reas, "The PUREX Process - A Solvent Extraction Reprocessing Method for Irradiated Uranium," p. 33, 1957.

[12] A. Vaudano and et al., "Le procédé PUREX," *Le Trait. du Combust. usé*, pp. 33–86, 2008.

[13] S. B. Pope, *Turbulent Flows*, vol. 12, no. 11. 2001.

[14] G. K. Batchelor, "Diffusion in a field of homogeneous turbulence. 2 The relative motion of particles," *Proc. Camb. Philol. Soc.*, vol. 48, no. September 1951, pp. 345–362, 1952.

[15] H. R. Hiester, M. D. Piggott, P. E. Farrell, and P. A. Allison, "Assessment of spurious mixing in adaptive mesh simulations of the two-dimensional lock-exchange," *Ocean Model.*, vol. 73, no. January, pp. 30–44, 2014.

[16] C. Hirsch, *Numerical Computation of Internal and External Flows*, Second edi. Elsevier, 2007.

[17] D. L. Marchisio, R. D. Vigil, and R. O. Fox, "Quadrature method of moments for aggregation-breakage processes," *J. Colloid Interface Sci.*, vol. 258, no. 2, pp. 322–334, 2003.

[18] T. Wang, J. Wang, and Y. Jin, “A novel theoretical breakup kernel function for bubbles/droplets in a turbulent flow,” *Chem. Eng. Sci.*, vol. 58, no. 20, pp. 4629–4637, 2003.

[19] Y. Liao and D. Lucas, “A literature review on mechanisms and models for the coalescence process of fluid particles,” *Chem. Eng. Sci.*, vol. 65, no. 10, pp. 2851–2864, 2010.

[20] S. Kumar and D. Ramkrishna, “On the solution of population balance equations by discretization—I. A fixed pivot technique,” *Chem. Eng. Sci.*, vol. 51, no. 8, pp. 1311–1332, 1996.

[21] A. Buffo, J. De Bona, M. Vanni, and D. L. Marchisio, “Simpli fi ed volume-averaged models for liquid – liquid dispersions : Correct derivation and comparison with other approaches,” vol. 153, pp. 382–393, 2016.

[22] S. Castellano, N. Sheibat-Othman, D. Marchisio, A. Buffo, and S. Charton, “Description of droplet coalescence and breakup in emulsions through a homogeneous Population Balance Model,” *Chem. Eng. J.*, 2018.

[23] S. G. Saddoughi and and S. V. Veeravalli, “Local isotropy in turbulent boundary layers at high Reynolds number,” *J. Fluid Mech.*, vol. 268, pp. 333–372, 1994.

[24] P. Davidson, *Turbulence: An Introduction for Scientist and Engineers*, vol. 540, no. 1. Oxford University Press, 2015.

[25] ANSYS Incorporation, “Modeling Flows in Moving Zones,” *FLUENT 6.0 User’s Guid.*, vol. 1, no. 1, pp. 1–68, 2001.

[26] R. M. Hockey and J. M. Nouri, “Turbulent flow in a baffled vessel stirred by a 601pitched blade impeller,” *Chem. Eng. Sci.*, vol. 51, no. 19, pp. 4405–4421, 1996.

[27] J. Véron, “S . H . Preston — Demography , Measuring and Modeling Population Processes,” pp. 591–592, 2018.

[28] R. W. Thompson and D. A. Cauley, “A population balance model for fish population dynamics,” *J. Theor. Biol.*, vol. 81, no. 2, pp. 289–307, 1979.

[29] World Nuclear Association, “World Nuclear Performance Report 2017,” p. 36, 2017.

[30] N. Sinha, A. E. Tejada-Martínez, C. Akan, and C. E. Grosch, “Toward a K-Profile Parameterization of Langmuir Turbulence in Shallow Coastal Shelves,” *J. Phys. Oceanogr.*, vol. 45, no. 12, pp. 2869–2895, 2015.

[31] L. H. B.Andersson, R.Andersson, L.Hakansson, M.Mortensen, R.Sudiyo , B.vanWachem, *Computational Fluid Dynamics for Engineers*. 2012.

[32] S. S. Kutateladze, “The mixing length hypothesis in the turbulence theory,” *Int. J. Heat Mass Transf.*, vol. 27, no. 11, pp. 1947–1951, 1984.

[33] R. Eymard, T. Gallouët, and R. Ele Herbin, “Finite Volume Methods,” *P.G. Ciarlet, J.L. Lions eds*, vol. 7, no. January, pp. 713–1020, 2003.

[34] D. L. Marchisio, J. T. Pikturna, R. O. Fox, and R. D. Vigil, “Quadrature method of moments for population balance equations,” *AIChE*, vol. 49, no. 5, pp. 1266–1276, 2003.

[35] D. L. Marchisio and R. O. Fox, “Solution of population balance equations using the direct quadrature method of moments,” *J. Aerosol Sci.*, vol. 36, no. 1, pp. 43–73, 2005.

[36] E. K. Nauha and V. Alopaeus, “Modeling method for combining fluid dynamics and algal growth in a bubble column photobioreactor,” vol. 229, pp. 559–568, 2013.

[37] A. H. Alexopoulos, D. Maggioris, and C. Kiparissides, “CFD analysis of turbulence non-

homogeneity in mixing vessels A two-compartment model," vol. 57, pp. 1735–1752, 2002.

[38] E. H. Wissler, "Physicochemical hydrodynamics (Levich, Veniamin G.)," *J. Chem. Educ.*, vol. 40, no. 10, p. A827, Oct. 1963.

[39] C. Reads, "PSE : a Fortran program for modeling well-stirred reactors," no. January, 2017.

[40] R. Sungkorn, J. J. Derksen, and J. G. Khinast, "Modeling of aerated stirred tanks with shear-thinning power law liquids," *Int. J. Heat Fluid Flow*, vol. 36, pp. 153–166, Aug. 2012.

[41] T. D. Canonsburg, "ANSYS Fluent Meshing User ' s Guide," vol. 15317, no. November, pp. 724–746, 2013.

ACKNOWLEDGMENTS

Remerciements

Une nouvelle langue, des nouvelles personnes, des nouvelles cultures et plein d'expériences. Je ne sais pas si c'est possible résumer mes deux derniers ans en quelques lignes. Je vais essayer.

Tout d'abord, merci à ma tutrice de stage, Mme Sophie CHARTON, pour m'avoir donné la possibilité d'être au CEA et de travailler sur cet important projet. Merci également pour m'avoir toujours soutenu et supporté pendant les 6 mois de stage. Merci aussi à mon tuteur « pratique », Simone CASTELLANO, pour m'avoir donné la possibilité d'apprendre des sujets compliqués et inconnus en très peu de temps. Simone, tu as été comme un frère. Je n'oublierai jamais les discours scientifiques, de travail et de vie que on a abordé ensemble. Bon courage pour la suite de ta thèse.

Merci à tous mes collègues, David Hermanito, David D., Mathieu, Azeddinne, Chloé, Léa, Youssri, Chris et Tojo, avec lesquels j'ai partagé mes journées de travail, mes préoccupations et toutes les belles soirées estivales en Avignon. En particulier, je voudrais remercier mes collègues stagiaires Fidèle et Miriana, pour avoir affronté cette expérience ensemble.

Merci à l'Ecole des Mines de Saint-Etienne, où j'ai passé 18 mois incroyables. Merci à tous les professeurs qui m'ont permis de découvrir des nouveaux sujets d'une façon différente de celle italienne. Une approche plus personnelle qui m'a permis d'établir des rapports solides que je garderai pour toute ma vie.

On vient à mes copains d'aventure. Vous avez été beaucoup ! Merci à ma famille italienne : Claudia, Corinne, Daniela, (b)Linda, Luca, Gigi, Max, Maria Elena, Martina, Giuditta, Erica, Andrea Borgognone, Giacomo et notre italo-allemand don Mimmo. Merci pour tous les diners ensemble, pour les soirées au Bul et pour toutes les bouteilles tombées.

Merci aux Juedas : Felipinho, Jaiminho, Joazinho, Seb, Marco, Andrea et les invités Lucas, Jacobo et Jimmy. Mes frères, copains des soirées et de maladies. C'est grâce à vous que cet Erasmus a pu être vraiment génial. Vous serez toujours dans mon cœur et je vous promets qu'on se reverra bientôt.

Merci à la coloc Stéphanoise : Marco, Andrea et Joao, ma famille. Merci pour m'avoir aidé dans toutes les difficultés et merci pour avoir partagé avec moi tous les bons et les mauvais moments de notre vie à Sainté. 9, Rue Brossard restera la maison des bêtises, des épisodes de GOT, des chansons jouées avec la guitare et des repas du dimanche. Je vous aime les gars.

Merci à tous les gens que j'ai rencontré pendant cette expérience incroyable. Vous faites tous partie de mes très bons souvenirs que je garderai de Saint-Etienne

Enfin, merci aux colocs Avignonnais : Simon, Richard, Eddy (aka chef Esposito), Margaux (à 7h08) et Marjo. Merci pour tous les matchs de foot qu'on a regardé ensemble (même si la France a gagné la coupe du monde), pour les soirées et merci pour m'avoir permis de découvrir les fromages et les vins français (notamment les Cotes du Rhône). Merci surtout pour avoir été ma famille française, mon refuge après les dures journées de travail. Attendez-moi pour le retour au Bocaos !!

Ringraziamenti

Un grazie particolare al mio relatore, prof. Antonio Buffo, per avermi seguito durante la stesura di questo lavoro di tesi e per i sui preziosi consigli.

Alla mia famiglia. A Papà per avermi insegnato che bisogna stringere i denti sempre e che non bisogna mollare mai, perché il lavoro ripaga sempre. A Mamma per essere la mia confidente, la donna che ha sempre sopportato le mie paturnie. Grazie per avermi fatto capire che è solo donando che si riceve. A Maria, la mia complice e colei che conosce veramente le mie debolezze. A Carlo, il mio gigante buono, che con la sua stravaganza riesce a conquistare il cuore di tutti. Grazie per tutti i commenti domenicali sulla formula 1, sei il mio guru. A Francesco, il più testardo della famiglia. La tua straordinaria e precoce maturità mi ha già insegnato tanto. Siete la roccia sulla quale costruirò il mio futuro. Mi avete supportato in tutti questi anni, siete stati il porto sicuro in cui rifugiarmi nei momenti bui e siete stati sempre i primi a gioire delle mie vittorie. Senza di voi non sarei la persona che sono ora e non sarei mai arrivato a questo traguardo. Continuate a essere tutto questo, ve ne prego. Vi voglio bene.

A tutta la banda dei Carrillo, zia Antonietta e Tommasino, zio Gerardo, zia Rosanna e Lorenzino. Grazie per essere stati sempre al mio fianco (e grazie anche per tutti i quintali di salsa che abbiamo fatto).

A tutta la family pazza-Piazzolla, zio Peppe, zia Nella, Ale e Claudia, zia Costa e zio Rosario. Un grazie particolare a zio Ferdi, per avermi fatto dono dell'essere interista (onestamente non se sia un bene o un male). Grazie a tutti voi per avermi regalato dei momenti davvero bellissimi insieme.

Grazie alle mie nonne, Carmela e Maria, e ai miei nonni, Lorenzo e Carlo. Grazie per avermi insegnato ad essere umile e per tutti i valori che avete trasmesso alla nostra famiglia. Grazie anche a zia Carmelina, per tutti i boccacci di pomodori, melanzane, ecc. di cui mi ha fatto dono durante questi anni in trasferta.

A Michela, grazie per essere la mia compagna di viaggio da un po' di tempo a questa parte. Grazie per avermi detto di si quel 28 ottobre 2011. Mi hai sopportato e supportato sempre. Hai visto le mie lacrime, i miei momenti di ira e mi hai sempre sostenuto e spinto ad andare avanti. Dietro un grande uomo c'è sempre una grande donna. In questo caso grandissima e fortissima. Questo traguardo è anche il tuo. E sarà sicuramente il punto di partenza di altre mille avventure insieme.

A Michele, il mio compagno di banco/coinquilino/migliore amico/fratello. Da quel 10 settembre 2007 non ci siamo mai più separati (anche se ci hanno provato in tanti). Grazie per avermi accolto nella tua famiglia (grazie anche a Maria Antonietta, Toni e Angela). Grazie per essere stato il mio più grande consigliere e per aver reso questi 11 anni fantastici. Grazie per aver gioito e per aver sofferto con me. Ti voglio bene.

A Jacopo, bandolero (con mucho trabajo y poco dinero) di questi anni universitari. Grazie per aver condiviso con me il tuo percorso. Non dimenticherò mai tutte le lunghissime giornate in sessione passate insieme a studiare e ristudiare i quintali di libri, slide e appunti per gli esami. Grazie per tutti i calcetti e grazie per avermi fatto capire che si può giocare a calcio anche senza mai segnare, neanche per sbaglio, e che è più importante un tunnel che un goal. Ti voglio bene Ja.

Grazie al Drinchimteam, Manis, Andrea, Peppuzzo, Mattia, Paride, Carrieri e Jacopo. Grazie per aver animato le lezioni, per aver affrontato insieme gli esami più difficili e per essere stati la mia piccola famiglia torinese.

Grazie ad Andrea Valentini, mio compagno di viaggio in terra francese. Grazie per tutte le strategie elaborate per passare gli esami e per avermi dato delle preziosissime lezioni di economia. Senza di te questi 2 anni non avrebbero potuto essere così perfetti.

Grazie a Miriana, che ha condiviso con me gli ultimi 12 mesi, e in particolare il periodo dello stage. Grazie per essere stata il mio riferimento avignonese e per aver affrontato insieme a me tutte le difficoltà di questi ultimi mesi.

Grazie a tutti i miei colleghi di corso, i quali ho avuto il piacere e l'onore di poter conoscere. In particolare a Astrid, sempre presente in questi ultimi 6 anni, nonostante la distanza. Grazie anche e soprattutto a Katia, Elena e Sasi, per tutte le riunioni improvvisate negli ultimi tempi.

Grazie a Peppe e Silvia, per essere stati sempre presenti pur non essendo in contatto spesso.

Ai miei amici candelesi, Trombacco, Solazzo, Cianfano, Onesto, Davide, Federico, Marf, Arianna, Ugo, Maria Luisa, Nigro e Gaetano. Siete stati il mio punto di riferimento sempre, nonostante il tempo e la distanza. Grazie per avermi sempre accolto come se non ci fossimo mai separati. Un grazie in particolare a Serena e Debora, per essere state sempre in contatto con me durante tutti questi anni e per aver mostrato sempre affetto nei miei confronti. Siete e sarete sempre il mio riferimento principale. Un grazie doveroso anche a Vigo, perché nonostante i rari contatti telefonici, al mio ritorno mi ha sempre accolto calorosamente. Grazie per avermi "preso" sotto Andrea fino alle 4 del mattino. Siete davvero speciali, tutti.

Grazie a Giovanna, Michele, Angelo e Roberto. Le parole non basterebbero per descrivere le mille emozioni provate insieme. Voi lo sapete. Nel mio cuore un posto importante è riservato a voi.

Grazie agli zii che mi hanno cresciuto, Maria Rosaria, Tiziana, Rosaria F., Savino, Anna, Cinzia e Luigi, Francesco Cicerone e il comparone Domenico. Solo quel corridoio sa quante passeggiate ci sono volute per farmi addormentare.

Spero di non aver dimenticato nessuno, in tutti i casi, grazie a tutti coloro che ho incontrato durante questi 25 anni. Tutti voi avete contribuito a rendere migliore la mia vita e tutti voi mi avete fatto dono della vostra presenza.